UNIVERSITÀ DEGLI STUDI DI MILANO

Dottorato di Ricerca in Scienze della Terra
Ciclo XXVII

# COH fluids at upper-mantle conditions: an experimental study on volatile speciation and mineral solubility in the MS + COH system

Ph.D. Thesis

**Carla Tiraboschi**
Matricola R09571

*Tutore*
**Dr. Simone Tumiati**

*Co- Tutore*
**Prof. Peter Ulmer**

**Anno Accademico**
**2013-2014**

*Coordinatore*
**Prof.ssa Elisabetta Erba**

# Table of Contents

# Abstract

COH fluids play a fundamental role in many geological processes, controlling the location of melting in subduction zones and promoting mass transfer from the subducting lithosphere to the overlying mantle wedge. The properties of COH fluids are strictly dependent on the composition of the fluid in subduction systems, i.e., the speciation of the volatile components of the fluid itself and the presence of solutes deriving from the dissolution of rock-forming minerals. In the scientific literature, the speciation of COH fluids has been generally determined through thermodynamic calculations using equations of state of simple $H_2O$–non-polar gas systems (e.g., $H_2O$–$CO_2$–$CH_4$), equations that do not consider the complexity related to dissolution processes, which are substantially unexplored in COH fluids and limited so far to aqueous fluids (Newton & Manning, 2002). The aim of this work is to experimentally investigate the speciation of COH volatile components of the fluid and the dissolution of mantle minerals in carbon-saturated COH fluids at buffered $fO_2$ conditions.

Our experimental approach relies on two different techniques: i) analysis by means of quadrupole mass spectrometer (QMS) of the COH fluid from pierced run capsules to retrieve speciation of volatile components and ii) analysis of frozen COH fluid with laser-ablation inductively coupled plasma-mass spectrometry (LA-ICP-MS) to measure the amount of solutes. Experiments were conducted at $P$ = 1–3 GPa and $T$ = 700–1200 °C using a rocking piston-cylinder apparatus. Mantle minerals in equilibrium with COH fluids are represented by synthetic forsterite, enstatite and natural magnesite. $fO_2$ conditions were controlled employing the double capsule technique and nickel–nickel oxide (NNO) buffer. We also performed a series of experimental runs in the COH-only system in single or double capsules, varying the packing material that surrounds the capsule and the oxygen buffer, to evaluate the differences in COH volatile speciation determined by the choice of the experimental setup.

Quantitative analyses of COH volatile speciation were retrieved by piercing the capsule in a gas-tight vessel at $T$ = 80 °C and convoying evolved gases to a QMS through a heated line to avoid the condensation of water.

Our experimental results on COH volatile speciation highlighted the importance of the experimental verification of volatile speciation, which can diverge considerably compared to the thermodynamic model (Perplex; Connolly, 1990) depending on the experimental strategies adopted. In particular, when single capsules are employed, the packing material that surrounds the capsule exerts a major control on the COH volatile speciation.

Double capsule experiments provided similar COH volatile speciation compared to thermodynamic modeling for what concerned the COH-only system. However, the addition of mantle minerals in the experimental charge at the same $P$–$T$–$f$H$_2$ conditions determines a shift in the COH fluid composition toward more $CO_2$-rich terms.

At $P$ = 1 GPa, data show an increase in $CO_2$ of + 11 mol% at $T$ = 800 °C and of + 26 mol% at $T$ = 900 °C in the COH fluid in equilibrium with forsterite + enstatite compared to a pure COH fluid. To evaluate if this shift could be determined by interactions of the COH fluid with solid phases, we retrieved the solubility of mantle minerals in COH fluids through the cryogenic LA-ICP-MS technique described by Kessel et al. (2004).

With this method the COH fluid is trapped into a diamond layer, the aqueous part of the COH fluid is frozen to avoid any precipitation of solutes and is analyzed through LA-ICP-MS.

Experimental results on mantle minerals solubility in COH fluids suggest that the amount of dissolved material in COH fluids is similar compared to mantle mineral solubility in $H_2O$-only fluid and ranges from the 2 wt.%, expressed as MgO + $SiO_2$, at $P$ = 1 GPa and $T$ = 800 °C, to 12 wt.% at $P$ = 2 GPa and $T$ = 1100 °C for the forsterite + enstatite assemblage.

The formation of dissolved species containing carbon, such as $CO_3^{2-}$ and $Mg(HCO_3)^+$ lead to an increase in the amount of carbon in the fluid, but not in $CO_2$ species. In order to get the increase of $CO_2$ that we observed in experiments analyzed through quadrupole mass spectrometry, we suggest a series of possible dissolution reactions involving Mg-solutes, which could lead to increase the amount of $CO_2$ in the fluid.

As a consequence, the quantity of $CO_2$ infiltrating into the mantle-wedge could be remarkably high, compared to the COH fluid composition predicted by thermodynamic modeling.

# Chapter 1

# General introduction and experimental

## 1.1. Setting the scene: COH fluids at mantle conditions

Fluids are involved in many geological processes from controlling the location and extent of melting at subduction zones to hydrothermal ore genesis, earthquake generation, and rock-forming processes in general.

Water is considered the most abundant volatile-bearing species at mantle conditions (e.g., Scambelluri & Philippots, 2001; Poli & Schmidt, 2002; Manning, 2004) and so far the most extensive experimental work on the effect of volatiles on mantle relations have been conducted on systems in presence of an aqueous fluid (see review by Ulmer, 2001). $H_2O$ may be present at high-pressure conditions under different forms: i) as a free fluid phase (e.g., Peacock, 2001); ii) stored in hydrous minerals like amphibole, lawsonite, zoisite and phlogopite (e.g., Poli & Schmidt, 1995; Ulmer & Trommsdorff, 1995; Poli & Schmidt, 1998; Ulmer & Trommsdorff, 1999); iii) incorporated in nominally anhydrous mineral (NAMS) such as olivine and pyroxene (e.g., Berry et al., 2005; Withers & Hirschmann, 2007; Bali et al., 2008; Litasov et al., 2009; Ardia et al., 2012).

Although subduction-related fluids appear to be dominated by an aqueous component, composition of arc-magmas gases and metasomatized mantle-wedge peridotites suggest that carbon, stored in the altered oceanic crust, ophicarbonates and metasediments, is also recycled back into the mantle wedge, at least partially (e.g., Bebout, 1995; Wallace, 2005; Gorman et al., 2006; Thomsen & Schmidt, 2008; Martin & Hammouda, 2011; Tsuno & Dasgupta, 2011). Carbon is retained in graphite/diamond and in carbonate phases, which are refractory and stable at very high pressure, as shown by experimental data (Molina e

Poli, 2000; Dasgupta & Hirschmann, 2006; Brey et al., 2008; Poli et al., 2009; Grassi & Schmidt, 2011). Thermodynamic models (Kerrick & Connolly, 1998; Kerrick & Connolly, 2001a, 2001b; Gorman et al., 2006) predict very small $CO_2$ fractions in COH fluid resulting from decarbonation processes, which only occur at low-*P* and high-*T* conditions. However, at top-of-the-slab conditions the effect of carbonate dissolution could have an important role in raising the concentration of carbon in high-pressure fluids (Caciagli & Manning, 2003; Perchuk & Korepanova, 2011).

Several experimental studies investigated the effect of $H_2O$ (e.g., Green, 1973; Green & Falloon, 1998; Konzett & Ulmer, 1999; Fumagalli & Poli, 2005) and $CO_2$ (e.g., Eggler, 1975; Wyllie, 1977; White & Wyllie, 1992; Dasgupta & Hirschmann, 2007) on subsolidus and melting relations in peridotitic systems at upper-mantle conditions. However, only few works consider the effect of the simultaneous occurrence of $H_2O$ and $CO_2$ or more in general, the influence of COH fluids (i.e., the fluids belonging to the system C–O–H) on peridotitic systems (e.g., Olafsson & Eggler, 1983; Taylor & Green, 1988; Wallace & Green, 1988; Thibault et al., 1992; Jakobsson & Holloway, 2008; Foley et al., 2009; Tumiati et al., 2013). In particular, the speciation of the fluid in equilibrium with mantle minerals has been mainly estimated through thermodynamic modeling (e.g., Poli et al., 2009; Tumiati et al., 2013), using equations of state of simple $H_2O$–non-polar gas systems (e.g., $H_2O$–$CO_2$–$CH_4$) (see Section 2.1.1), equations that do not consider the complexity related to dissolution processes (Liebscher, 2010, and refs. therein) (see Chapter 3). In this study, experimental data on COH fluid composition in the COH-only system and in the MS + COH system at $P$ = 1–3 GPa and $T$ = 700–1200 °C will be presented, considering the volatile species that compose the fluid (Chapter 2) and the solute content of COH fluids in equilibrium with mantle minerals (Chapter 3).

### 1.1.1. COH fluids in the upper mantle

The clearest clue that a fluid phase was present during the petrogenesis is the occurrence of fluid inclusions. Primary inclusions in peridotite- and eclogite-forming minerals, including diamonds, are very valuable as they provide information on the fluid regime in the mantle.

Fluid inclusions in shallow-mantle xenoliths are mainly dominated by $CO_2$ (Roedder, 1965, 1984; Pasteris, 1987; Frezzotti et al., 1994; Andersen & Neumann, 2001). $H_2O$ is a difficult component to detect in fluid inclusions as it may react with the host mineral at

high-pressure or during eruption (Andersen & Neumann, 2001) or could be solubilized in the ascending melt (Luth, 2003). Nonetheless, $CO_2$–$H_2O$ inclusions have been found in peridotite nodules from Ichinomegata, Japan (Roedder, 1965) and Schiano et al. (1995) reported pure $H_2O$ inclusions in harzburgites from Bataan (Philippines). Small amounts of $H_2O$ were measured by Berkesi et al. (2009) in $CO_2$-rich inclusions in a spinel peridotite from the Pannonian basin (Hungary). Raman microspectroscopy allowed detecting $H_2O$ in diamond-bearing $CO_2$-rich inclusions from garnet clinopyroxenites from Oahu, Hawaii (Frezzotti & Peccerillo, 2007). With the same technique $H_2O$–$CO_2$ fluid inclusions coexisting with silicate melt inclusions have been studies in spinel lherzolite xenoliths from the Carpathian-Pannonian region by Hidas et al. (2010).

Carbon dioxide and water are not the only COH species detected in fluid inclusions. Carbon monoxide (CO) has been found in amphibole vein inclusions in wherlite xenolites, together with $CO_2$ (Bergman & Dubessy, 1984). $H_2$- and $CH_4$-bearing inclusions have been found in serpentinized peridotites (Peretti et al., 1992) and $H_2O$–$CO_2$, $CO_2$- and $CH_4$-rich fluid inclusions have been observed in granulitized eclogites (Fu et al., 2003a, 2003b).

The presence of $CH_4$ and $H_2$ in fluid inclusions is linked to reducing conditions in the COH system where carbonate species become unstable (Holloway, 1987). The chemical potential of oxygen ($\mu O_2$) plays a fundamental role in controlling the volatile speciation of the COH fluid. At high values of $\mu O_2$ (and therefore oxygen fugacity), $CO_2$ and $H_2O$ are the dominant species, while at low $\mu O_2$, $CH_4$ and $H_2$ become significant species (Luth, 1999).

Fluid inclusions have also been found in diamonds from mantle-derived xenoliths (e.g., Izraeli et al., 2001; Van Roermund et al., 2002; Klein-BenDavid et al., 2004; Tomlinson et al., 2007; Logvinova et al., 2008). Navon et al. (1988) observed $H_2O$- and $CO_3^{2-}$-rich inclusions in diamonds, suggesting that diamonds grew from the same fluid that subsequently was trapped in the micro-inclusions. Recently, microdiamonds from Lago di Cignana in Western Alps were described as precipitated from a COH fluid (Frezzotti et al., 2011, 2013).

Elemental carbon has also been found as graphite in multiphase inclusions in high-*P* peridotites (Naemura et al., 2009) or as interlayered graphite in phlogopite structure (e.g., Finero peridotite, Ferraris et al., 2004). It is worth to note that the occurrence of graphite/diamond is particularly interesting because the volatile speciation of carbon

saturated fluids can be determined using fluid equations of state once pressure, temperature and redox conditions are fixed (e.g., Kerrick & Connolly, 1998; Gorman et al., 2006; Zhang & Duan, 2009).

The presence of COH fluids at mantle conditions is also suggested by the occurrence of carbon-bearing phases and hydrous minerals in mantle peridotites (e.g., Zhang et al., 2007; Scambelluri et al., 2008; Malaspina et al., 2010; Malaspina & Tumiati, 2012). Ultramafic rocks presenting carbonates and hydrous phases (amphibole and phlogopite) are in fact though to have witnessed a metasomatic processed driven by aqueous $CO_2$-bearing fluid.

### 1.1.2. Effects of volatiles on mantle phase relations

Since the pioneering works of Bowen (1928), Goranson (1931), Tuttle & Bowen (1958) and Yoder & Tilley (1962), aqueous fluids has been recognized as fundamental in many mantle processes. Water is a species that changes dramatically the melting behavior in a variety of systems, as it is highly soluble in melts especially at high-pressure conditions (Burham & Jahns, 1962; Hamilton et al., 1964). In particular, the presence of $H_2O$ in the peridotitic system causes an inversion in the slope of the solidus, accompanied by lower melting temperatures (e.g., Kushiro et al., 1968; Kushiro, 1974; Green, 1973; Mysen & Boettcher, 1975). Small to moderate amounts of water (0.1 to 0.5 wt.%) in the mantle source lead to a decrease in the melting temperatures of 100–150 °C while in $H_2O$-saturated magmas the melting temperature decrease is in the order of 300–400 °C (e.g., Green, 1973; Wallace & Green, 1991; Niida & Green, 1999; Ulmer, 2001; Fumagalli et al., 2009).

Eggler (1974, 1975), Mysen (1975) and Wyllie (1977) demonstrate that also the addition of $CO_2$ influences the melting temperature in peridotitic systems, mainly caused by the formation of carbonate phases through carbonation reactions:

$$\text{forsterite} + CO_2 = \text{enstatite} + \text{magnesite} \quad (1.1)$$

$$\text{diopside} + \text{forsterite} + CO_2 = \text{enstatite} + \text{dolomite} \quad (1.2)$$

In the model system $CaO–MgO–SiO_2–CO_2$ Eggler (1975) observe that reaction 1.2 lowered the solidus temperature, causing a bend in the solidus shape at 2.8 GPa and 1240 °C.

Compared to the $H_2O$-saturated system (Wallace & Green, 1991; Conceição & Green, 2004), carbonated peridotites (Falloon & Green, 1989; Dasgupta & Hirschmann, 2006) melt at higher temperatures. Dasgupta & Hirschmann (2006, 2007) observed that the solidus temperature of a carbonated peridotite at 6.6 GPa drops in temperature by ~ 600 °C once that the storage capacity of $CO_2$ is exceeded and magnesite is stabilized in the system by reaction 1.1. Once that a carbonate phase is present, the melting temperature seems to increase with increasing bulk $CO_2$ (Dasgupta & Hirschmann, 2007).

Few experimental works are available for what concerned carbonated peridotites in presence of a $H_2O$–$CO_2$ mixed fluid (e.g., Taylor & Green, 1988; Thibault et al., 1992; Jakobsson & Holloway, 2008; Foley et al., 2009). In particular, experimental data focusing on subsolidus relations are lacking, with the exception of the contributions of Olafsson & Eggler (1983), Wallace & Green (1988), Tumiati et al. (2013) and Green et al. (2014). These works show several discrepancies, probably related to the different experimental strategy adopted. In the experimental study of Tumiati et al. (2013) the authors located the solidus at higher temperature compared to Olaffson & Eggler (1983), although the melting temperature was lower compared to the only-$CO_2$ system of Dasgupta & Hirschmann (2006), suggesting a key role of the relative abundances of $H_2O$ and $CO_2$ in the fluid.

Different modal amount in $H_2O$ and $CO_2$ influence not only the melting behavior but also the subsolidus relations, which are deeply affect by the volatile-bearing species. Wyllie (1977) and Eggler (1978) suggested that the location of reaction 1.2 depends on the $XCO_2$ of the coexisting fluid phase, defined as $CO_2/(H_2O + CO_2)$. Reaction 1.2 in fact shift towards higher pressure as $XCO_2$ diminishes. Tumiati et al. (2013) highlighted how variable $H_2O/CO_2$ ratio can influence the appearance and the relative ratios of the major phases in peridotites (e.g., olivine).

Another fundamental property of $H_2O$-bearing phases at high-pressure conditions is the capacity to transport dissolved species (e.g., Anderson & Burnham, 1965; Nakamura & Kushiro, 1974; Manning, 1994). The amount of solutes from rock-forming minerals in aqueous fluids increase with increasing pressure (Zhang & Frantz, 2000; Zotov & Keppler, 2002; Caciagli & Manning, 2003) and, at certain conditions above the solidus, the fluid is no longer distinguishable from the silicate melt and a supercritical liquid is formed (e.g., Kennedy et al., 1962; Stalder et al., 2000; Mibe et al., 2002). At lower pressure and temperature, the solubility of mantle minerals, such as forsterite and

enstatite, has been measured in aqueous fluid (e.g., Nakamura & Kushiro, 1974; Newton & Manning, 2002) up to 1.5 GPa and at $T$ = 700–1300 °C. Experimental data on mineral dissolution in $H_2O$–$CO_2$ fluid are available for quartz (Walther & Orville, 1983; Newton & Manning, 2000, 2009; Shmulovic et al., 2006), albite and diopside (Shmulovic et al., 2001) and suggests that solubility decreases with increasing content of $CO_2$ in the fluid.

### 1.1.3. Objectives and approaches

We choose to investigate COH fluids at upper-mantle conditions, namely $P$ = 1–3 GPa and $T$ = 700–1200 °C. We performed rocking piston-cylinder experiments at the Laboratory of Experimental Petrology, Department of Earth Sciences, University of Milan (Italy). A rocking piston-cylinder apparatus was employed to avoid chemical segregation, typical of fluid saturated systems (Schmidt & Ulmer, 2004).

The problem of the composition of high-pressure COH fluids was approached from two different perspectives:

1) Volatiles: we developed with the collaboration of Sandro Recchia (University of Insubria, Italy) a capsule-piercing device for the extraction of quenched high-pressure COH fluids from piston-cylinder experiments. The capsule-piercing device is connected to a quadrupole mass spectrometer (QMS) to retrieve quantitative analyses of the volatiles constituting the COH fluid: we evaluated the COH volatile speciation in the COH-only and in the MS + COH systems by varying the experimental setups and the oxygen buffers. We considered two different types of material to embed the capsule during the experimental run: BN and MgO. We also employed different oxygen buffers such as nickel–nickel oxide (NNO), iron–wustite (IW) and hematite–magnetite (HM). Experiments were performed in single or double capsule starting from oxalic acid dihydrate and graphite.
2) Solutes: we determined the amount of solutes in high-pressure COH fluids at oxygen-buffered condition in the system MS + COH, through the cryogenic laser-ablation inductively coupled plasma mass-spectrometry (LA-ICP-MS) technique (Kessel et al., 2004; Aerts et al., 2010) carried out with the collaboration of Thomas Pettke at the Institute of Geological Sciences, University of Bern (Switzerland), employing a freezing stage developed at ETH Zurich (Switzerland). Experiments were performed starting from two powder mixtures:

forsterite + minor enstatite and enstatite + magnesite + minor forsterite. COH fluids were generated from oxalic acid anhydrous and $H_2O$. Fluid composition was buffered employing the double capsule technique and NNO buffer.

# 1.2. Experimental procedure

In this section an overview on the experimental procedures to synthesize COH fluid at high-pressure and high-temperature conditions will be presented, together with the procedure to obtain the mantle minerals mixtures employed in this experimental study. The description of the rocking piston-cylinder apparatus will also be provided.

## 1.2.1. Starting materials

Several solid organic compounds can be charged to obtain a COH fluid in the experimental runs. Usually the choice of the fluid source depends on the requested H/O ratio, assuming that this ratio is maintained at the experimental *P–T* conditions (Table 1.1).

For this experimental study, we choose as fluid sources oxalic acid dihydrate (OAD; $H_2C_2O_4 \cdot 2H_2O$) for experiments on COH volatile speciation (Chapter 2) and oxalic acid anhydrous (OAA; $H_2C_2O_4$) + Cs-doped $H_2O$ for experiments on mantle-minerals solubility in COH fluids (Chapter 3).

| Source of fluid | Chemical formula | H/O ratio | References |
|---|---|---|---|
| Fumaric acid | $C_4H_4O_4$ | 1:1 | Eggler et al. (1979), Truckenbrodt et al. (1997) |
| Stearic acid | $C_{18}H_{36}O_2$ | 18:1 | Holloway & Jakobsson (1986), Jakobsson & Holloway (1986), Taylor & Foley (1989), Jakobsson & Oskarsson (1990), Matveev et al. (1997) |
| Oxalic acid dihydrate | $H_2C_2O_4 \cdot 2H_2O$ | 1:1 | Holloway et al. (1968), Holloway & Reese (1974), Morgan et al. (1992), Rosenbaum & Slagel (1995) |
| Phtalic acid | $C_8H_6O_4$ | 3:2 | Matveev et al. (1997) |
| Benzoic acid | $C_7H_6O_2$ | 3:1 | Matveev et al. (1997) |

Table 1.1. Examples of organic compounds used to generate COH fluids.

Oxalic acid dihydrate is a solid compound commonly used in high-pressure experiments (e.g., Holloway et al., 1968; Holloway & Reese, 1974; Morgan et al., 1992; see also Fig. 1.1). At low temperature ($T$ = 230–350 °C) the thermal dissociation of OAD produces $H_2O$, $CO_2$ and CO via the reaction:

$$0.2\ H_2C_2O_4{\cdot}2H_2O = 0.6\ H_2O + 0.2\ CO_2 + 0.2\ CO \quad \text{(Pernert, 1952)} \qquad (1.3)$$

Morgan et al. (1992) observed that the $CO_2$ and $H_2$ contents increase with increasing temperature due to the reaction:

$$H_2O + CO = CO_2 + H_2 \qquad \text{(Holloway et al., 1968)} \qquad (1.4)$$

As data from Morgan et al. (1992) closely fit to a linear function of temperature (Fig. 1.1), it is possible to extrapolate the dissociation of oxalic acid at $T$ = 800 °C in this way:

$$H_2C_2O_4{\cdot}2H_2O = 2\ H_2O + 2\ CO_2 + H_2 \qquad (1.5)$$

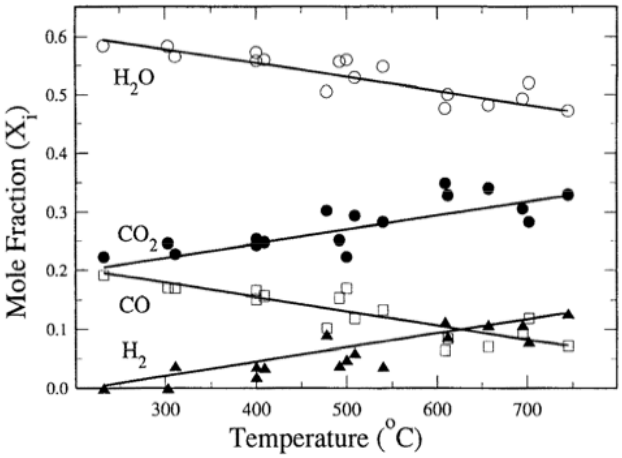


Fig. 1.1. Speciation of the fluid generated from thermal decomposition of oxalic acid dihydrate (after Morgan et al. 1992).

In the experimental runs performed to retrieve mantle minerals solubility in COH fluids we employed as fluid sources oxalic acid anhydrous. The thermal dissociation of OAA at high temperature conditions generates a $CO_2$–$H_2$ fluid according to the reaction:

$$H_2C_2O_4 = 2\ CO_2 + H_2 \qquad (1.6)$$

Therefore, to obtain a COH fluid in the experimental charge we weighted oxalic acid anhydrous and $H_2O$ (doped with Cs, see Chapter 3) in order to obtain a roughly equimolar $CO_2$–$H_2O$ 1:1 mixture.

Minerals forsterite (FoEn) and enstatite (EnFo) were synthesized starting from dried nanocrystalline $Mg(OH)_2$ (Sigma-Aldrich, 99.9%) and silicon dioxide (Balzers, 99.9%) mixed in stoichiometric proportions, pelletized and loaded in a vertical furnace at 1500 °C for 24 h. The temperature rate was 300 °C/h till 300 °C, then 50 °C/h till 400 °C to allow slow dehydration of $Mg(OH)_2$, and again 300 °C/h until 1500 °C. Synthesis products were ground in ethanol for 1 hour, dried and characterized by means of X-ray powder diffraction data (Bruker, AXS D8 Advance, ETH Zurich; Philips X'pert MPD, University of Milan) (Fig. 1.2). Natural magnesite from Pinerolo (Italy), checked for purity at scanning electron microscope and characterized chemically at the electron microprobe (Jeol 8200 Superprobe, University of Milan; Table 1.2) was ground under ethanol for 1 h, dried and added to the enstatite powder (EnFo) to obtain the starting material mix EnMag. Results of Rietveld structure refinements, performed using the software GSAS (http://www.ccp14.ac.uk/solution/gsas/) are reported in Table 1.3.

| MgO | $Na_2O$ | $TiO_2$ | MnO | $K_2O$ | $Al_2O_3$ | $SiO_2$ | $Cr_2O_3$ | FeO | CaO | Total |
|---|---|---|---|---|---|---|---|---|---|---|
| 47.76 | 0.018 | 0.016 | 0.000 | 0.009 | 0.002 | 0.089 | 0.021 | 0.640 | 0.082 | 48.64 |

Table 1.2. Representative WDS analysis of the magnesite used in the starting material mix EnMag.

| | FoEn (wt.%) | EnFo (wt.%) | EnMag (wt.%) |
|---|---|---|---|
| Forsterite | 83.2 | 70.9 | 15.3 |
| Enstatite | 16.7 | 26.5 | 39.0 |
| Magnesite | - | - | 44.2 |
| Cristobalite | 0.1 | 2.6 | 1.5 |

Table 1.3. Relative abundances of minerals (wt.%) in the starting materials FoEn, EnFo and EnMag, retrieved from Rietveld structure refinements.

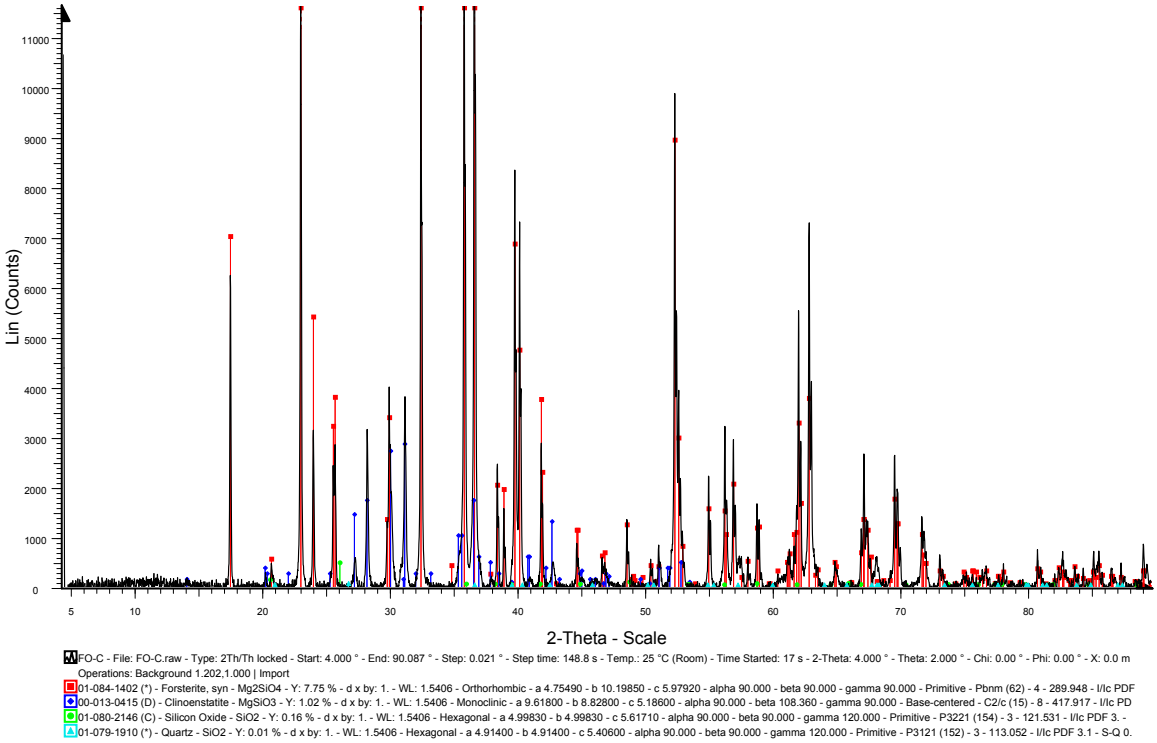


Fig. 1.2. X-ray powder diffraction pattern of the starting material FoEn.

## 1.2.2. Rocking piston-cylinder apparatus

In this experimental study a rocking piston-cylinder apparatus (Fig. 1.3) was employed to reach high-pressure and high-temperature conditions. The rocking piston-cylinder is a regular end-loaded piston-cylinder which completes a rotation of 180° during the experimental run, thus inverting its position in the gravity field (Schmidt & Ulmer, 2004). Unhomogeneity in mineral assemblage within the capsule is in fact common in fluid saturated experiments (e.g., Stalder & Ulmer, 2001; Melekhova et al., 2007). The rocking piston-cylinder was developed to overcome this problem (Schmidt & Ulmer, 2004). The rotation of the sample induces Raylegh-Taylor instabilities, forcing the fluid to migrate and causing chemical rehomogenisation. Authors show that rotating the piston-cylinder every 30 seconds (i.e., continuously) during the heating phase of the experiment leads to a homogeneous sample. Differentiations within the capsule in fact, occur at the beginning of the experimental run and, if not avoided in the heating phase, are very difficult to eliminate. Afterwards the recrystallization phase ends and starts the grain growth, which implies a lower mass transfer in the capsule charge (Schmidt & Ulmer, 2004; Melekhova et al., 2007).

Pressure calibration of the used rocking apparatus is based on the quartz to coesite transition (Bose & Ganguly, 1995) at $P$ = 3.72 GPa and $T$ = 1000 °C.

Fig. 1.3. Rocking piston-cylinder at the Laboratory of Experimental Petrology of the University of Milan (Italy). The orange part completes a rotation of 180° during the experimental run.

# Chapter 2

# COH volatile speciation in the COH and MS + COH systems

## 2.1. Introduction

It is widely accepted that COH fluids are crucial in modeling mantle processes. A significant effort has been made to unravel the effect of volatiles on mantle melting, especially in presence of $H_2O$-only and $CO_2$-only fluid (See Section 1.1.2). On the other hand, the system peridotite + COH fluid is substantially unexplored, with the exception of some pioneering works (Olafsson & Eggler, 1983; Wallace & Green, 1988; Tumiati et al., 2013; Green et al., 2014). In the scientific literature, the speciation of COH fluids has been generally determined through thermodynamic calculations using equations of state of simple $H_2O$–non-polar gas systems (e.g., $H_2O$–$CO_2$–$CH_4$), equations that do not consider the complexity related to dissolution processes (Liebscher, 2010). Experimental data are lacking especially for what concern the composition of the COH fluid in equilibrium with the peridotitic assemblage, even though the quantitative assessment of the COH species (i.e., the $H_2O/CO_2$ ratio) is crucial and deeply affect subsolidus and solidus relations.

In this chapter experimental data on volatile speciation of high-pressure COH fluids will be presented. Fluids were synthesized using a rocking piston-cylinder apparatus. The volatile speciation of COH fluids was retrieved with a capsule-piercing device connected to a quadrupole mass spectrometer.

### 2.1.1. Thermodynamic modeling of the COH system

Thermodynamic calculations have been largely employed to retrieve fluid speciation in a variety of geological subjects, also thanks to the availability of several user-friendly computer programs. Detailed reviews of different programs, equations of state and fugacity coefficients are given in Huizenga (2001). Thermodynamic modeling has been employed to estimate the fluid speciation in experiments where the analytical characterization at the microprobe was inevitably limited to the solid phases (e.g., Poli et al., 2009; Malaspina et al., 2010; Goncharov et al., 2012; Tumiati et al., 2013). However, the thermodynamic modeling relies on some concepts, which have to be kept in mind when it comes to calculate COH volatile speciation (French, 1966).

First, the calculation is valid only for a homogeneous fluid, which does not react with the mineral assemblage associated, except for graphite, and it does not apply if additional elements are present in the gas (e.g., N, S and Cl). Moreover, the gas phase is assumed to exhibit ideal behavior under all conditions. The presence of solutes will increase the solvus temperature of the system (e.g., Bowers & Helgeson, 1983) and affect the activity of $H_2O$ (e.g., Aranovich & Newton, 1983). However, dissolved species can be present in significant amounts in the fluid, especially at high $P$ and $T$ (e.g., Caciagli & Manning, 2003; Manning, 2004; Manning et al., 2010; Chapter 3). Second, the fluid is assumed to be in continuous equilibrium with graphite. Disequilibria with graphite, or the presence of disordered graphite, will change the thermodynamic properties of the fluid. Third, the use of different thermodynamic dataset to calculate the fugacity for phase assemblages that externally buffers the $fO_2$ of the fluid, such as fayalite–magnetite–quartz (FMQ) or nickel–nickel oxide (NNO), may give different results and can consequently lead to a different fluid compositions, as COH fluids are very sensitive even for small differences in oxygen fugacity (Huizenga, 2001).

The composition of fluids belonging to the pure COH system can be represented by means of ternary chemographic diagrams, where the volatile species $H_2O$, $CO_2$, $CH_4$, CO, $H_2$ and $O_2$ and the solid phases graphite/diamond are plotting (Fig. 2.1). The COH ternary diagram shows two phase fields separated by the graphite-saturation surface (Connolly, 1995; graphite boundary after Holloway & Reese, 1974), the locus of points representing the composition of the COH fluid phase coexisting with a solid carbon phase (GCOH fluids after Connolly, 1995). At high-pressure and low-temperature conditions, the graphite boundary approaches the tie-lines connecting $CH_4$–$H_2O$ and $H_2O$–$CO_2$. The

position and the shape of the graphite boundary are pressure- and temperature dependent (Fig. 2.1). By increasing temperature and decreasing pressure, the graphite boundary becomes smoother and is shifted towards the C vertex.

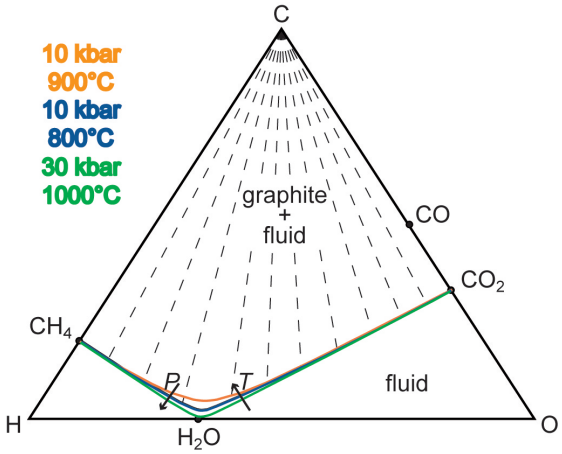


Fig. 2.1. COH ternary diagram. The graphite saturation surfaces are reported for the specified *P*–*T* conditions.

Considering the Gibbs phase rule, the field COH fluid + graphite is trivariant ($\nu = 3 + 2 - 2$), whereas the field of fluid without graphite is tetravariant ($\nu = 3 + 2 - 1$). The graphite + fluid field becomes univariant at constant *P* and *T*. This means that the fugacities of the volatile species present in the fluid cannot be varied independently. The composition of a fluid in equilibrium with graphite would lie on the tie-line that connects the carbon vertex to the graphite saturation surface. As carbon is a fixed composition phase the speciation of the fluid in terms of volatiles would be determined uniquely by the H/O molar ratio, ratio that can be expressed by the variable *X*(O) (Labotka, 1991; Connolly, 1995), i.e. the atomic fraction of oxygen relative to oxygen + hydrogen.

According to Connolly (1995), the significant species in COH fluids are $H_2O$, $CO_2$, $CH_4$, CO, $H_2$ and $O_2$. Therefore, the composition of a GCOH fluid is given by the equilibrium constants of the following reactions (French, 1966; Ohmoto & Kerrick, 1977):

$$2\ H_2 + O_2 = H_2O \qquad K_1 = fH_2O / fO_2 \cdot fH_2^2 \qquad (2.1)$$

$$C + O_2 = CO_2 \qquad K_2 = fCO_2 / a_c \cdot fO_2 \qquad (2.2)$$

$$2\ C + O_2 = 2\ CO \qquad K_3 = fCO^2 / a_c^2 \cdot fO_2 \qquad (2.3)$$

$$C + 2\ H_2 = CH_4 \qquad K_4 = fCH_4 / a_c \cdot fH_2^2 \qquad (2.4)$$

where $f_i$ is the fugacity of the species $i$, and $a_c$ is the activity of graphite ($a_c$ = 1 in GCOH fluids).

In this case there are four equations and six unknowns, i.e., the fugacities of $H_2$, $O_2$, $H_2O$, $CO_2$, CO and $CH_4$. Therefore, in order to be able to solve the system we need two compositional constraints. The first is given by the assumption that the total fluid pressure is equal to the solid pressure and that the sum of partial pressures of the fluid is constrained to equal the total pressure:

$$P_{fluid} = P_{H2O} + P_{O2} + P_{H2} + P_{CO2} + P_{CO} + P_{CH4} \quad (2.5)$$

Moreover, the sum of all the fluid species fractions must equals the unit:

$$1 = X_{H2O} + X_{CO2} + X_{CO} + X_{H2} + X_{O2} + X_{CH4} \quad (2.6)$$

Therefore, the total fluid pressure can be expressed as:

$$P_{fluid} = (fH_2O / X_{H2O}) + (fCO_2 / X_{CO2}) + (fCO / X_{CO}) + (fH_2 / X_{H2}) + (fO_2 / X_{O2}) + (fCH_4 / X_{CH4}) \quad (2.7)$$

The additional constrain needed to solve the system is given by the oxygen partial pressure or fugacity of oxygen ($fO_2$), which can be controlled in experiments using oxygen buffers (e.g., Eugster, 1957). For instance, at redox conditions buffered by the fayalite–magnetite–quartz buffer and low temperature and pressure, thermodynamics predicts that methane is the dominant species in COH fluids in equilibrium with graphite. At low temperature and high pressure, fluids are nearly aqueous as graphite saturation surface bend toward the $H_2O$ end-member on the COH diagram. Eventually, at higher temperature, COH fluids move to $CO_2$-rich compositions (Fig. 2.2).

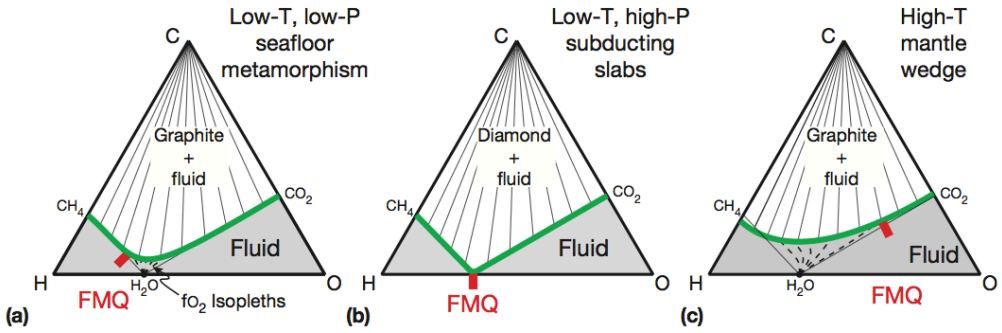


Fig. 2.2. Isobaric-isothermal COH diagrams, illustrating the shift of GCOH fluid composition at redox conditions buffered by fayalite–magnetite–quartz (FMQ) buffer (after Schmidt & Poli, 2014).

### 2.1.2. Experimental background on COH fluid speciation analysis

One of the first analysis of volatile species in COH fluids in piston-cylinder experiments was retrieved by Eggler et al. (1979) by means of a modified gas chromatograph. The authors investigated the solubility of $CO_2$–CO in different silicate melts. To experimentally verify thermodynamic calculations on COH fluid speciation the authors developed a system to extract the quenched fluid from the experimental run. The capsule was placed at the bottom of a vacuum valve connected to the gas chromatograph. By rapidly closing the valve the capsule was punctured and the gases were swept to the chromatographic column. This method provided quantitative analyses of quenched $CO_2$–CO fluids in equilibrium with phase assemblages including graphite at $P$ = 3 GPa and $T$ = 1700 °C. The volatile speciation of the fluid found by the authors was higher in $CO_2$ compared to the calculated equilibrium composition (Holloway, 1977), suggesting that fluid composition did not only depends from the starting material charged. The work of Eggler et al. (1979) highlighted for the first time the importance of an experimental verification of the fluid-phase composition estimated by means of thermodynamics.

Jakobsson & Holloway (1986) and Holloway & Jakobsson (1986) measured the solubility of a COH fluid in silicate melts at $P$ = 0.5–2.5 GPa and temperatures from 1000 to 1200 °C at iron–wustite (IW) oxygen fugacity conditions. They retrieved the composition of the dissolved fluid in albite, basanite and tholeiite melts through a quadrupole mass spectrometer (QMS) by heating the glass samples to 1200 °C for 5 minutes under vacuum conditions. The path from the samples to the QMS was short to minimize gas phase reactions, although the authors could not completely exclude post-quench reactions.

Taylor & Foley (1989) proposed a capsule-piercing device composed of a modified Withey regulating valve connected to a mass spectrometer. This method allowed analyzing the GCOH fluid in equilibrium with graphite, WC and WO (WC–WO buffer) from 0.9 to 3.5 GPa and temperatures from 1000 to 1260 °C. No evidences that quench significantly altered the fluid composition were observed. The authors pointed out that most fluid buffers used by experimentalists lack of experimental verification of oxygen fugacity and fluid composition, assuming perfect agreement between the calculation and the experimental value.

Morgan et al. (1992) measured the speciation of a COH fluid produced by the decomposition of oxalic acid dihydrate at $P$ = 0.1 GPa and temperatures from 230 to 750 °C, using Raman spectroscopy and silica glass capsules. The abundance of water was

derived from mass balance calculation due to analytical difficulties. The authors demonstrate the quenchability of fluids from run conditions through reversal experiments. Experimental data showed poor agreement between analyzed products and equilibrium model speciation using equation of state from Saxena & Fei (1988). The authors suggest a process of the form $CO + H_2O = CO_2 + H_2$ that enrich the composition of the fluid in $CO_2$ and $H_2$ with increasing temperatures. As hydrogen tends to escape from the capsule especially at high temperature, the composition of the COH fluid shifts eventually toward equimolar binary $H_2O$–$CO_2$ mixtures (see also Section 1.2.1).

Jakobsson & Oskarsson (1994) modified the vacuum valve proposed by Eggler et al. (1979) by connecting it to a QMS. The capsule-piercing device was modified to allow the analysis of $H_2O$ by heating the inlet system to 80 °C and turn $H_2O$ into vapor. The authors retrieved the speciation of a COH fluid at iron–wustite oxygen buffer conditions in equilibrium with graphite at pressures from 0.5 to 1 GPa and temperatures from 900 to 1200 °C. The calculations using the EoS of Saxena & Fei (1987) failed to reproduce exactly the experimental results. In particular, the calculation predicts with reasonable accuracy the trends of the major species, whereas calculated minor species poorly fitted the experimental data. Authors suggested that the discrepancy between calculated and experimental values could be ascribed to the lack of thermodynamic data at high *T* and *P*.

Rosenbaum & Slagel (1995) investigated the effect of different packing materials on the speciation of COH fluids in piston-cylinder experiments, considering single and double capsule assemblies. Condensable volatile ($CO_2$ and $H_2O$) were frozen in liquid $N_2$ and measured using a manometer (for $CO_2$) and a pressure gauge (for $H_2O$). The non-condensable gases were frozen into a sample tube using He and were analyzed through mass spectrometry. The authors considered different packing materials: NaCl, $BaCO_3$, Pyrex, soft glass, crushable alumina, pyrophyllite and different mixtures of hematite, NaCl, $BaCO_3$ and talc. The analyses revealed that the nature of the material that surrounds the capsule is critical to maintain a stable fluid composition. In particular, $H_2$ can infiltrates into the sample volume and reacts with $CO_2$ to produces both CO and $H_2O$. The authors suggested that double capsule assemblies, with sufficient $H_2$-absorbing capacity to maintain fluid composition, are the best option to generate constrained fluid compositions.

Matveev et al. (1997) analyzed oxygen buffered GCOH fluids over 7.5 orders of magnitude of $\log f O_2$ (from $\log f O_2 = -8.5$ to $\log f O_2 = -16$) through a piercing device and

gas chromatography. The authors focused their investigation at reducing oxygen fugacity conditions at $P$ = 2.4 GPa and $T$ = 1000 °C, employing boron nitride (BN) as packing material. All the retrieved volatile speciation fall along the graphite saturation surface, suggesting that the analyzed fluids represent equilibrium composition. Authors investigated post-quench modifications by varying the quenching rates of the experiments, observing that slow quench rates (< 120 °C/second) induce back reactions in the COH fluid.

Truckenbrodt et al. (1997) investigated the hydrogen permeability in two different packing materials: BN and unfired pyrophyllite. The authors analyzed the COH volatile speciation produced from different organic compounds at $P$ = 1 GPa and $T$ = 900 °C with a gas chromatograph connected to a heated capsule-puncturing system. The system was calibrated for quantitative analyses of $H_2$, CO, $C_2O_6$, $CO_2$, $CH_4$ and $H_2O$. Results showed that BN nitride was nearly impermeable to hydrogen. The authors suggested that by employing BN in piston-cylinder experiments the redox condition depends only on the composition of the starting material and not from the furnace assembly. In a following work, Truckenbrodt & Johannes (1999) analyzed COH fluids using different noble metal capsules with the same analytical technique used by Truckenbrodt et al. (1997). Gold capsules up to $T$ = 1000 °C and $P$ = 1 GPa showed no remarkable oxygen loss. The oxygen content of $Ag_{75}Pd_{25}$ capsules remains nearly constant during the experiment at $T$ = 1000 °C. Platinum capsules presented a distinct oxygen loss (up to 79 wt.% compared to the initial oxygen) starting from $T$ = 1100 °C.

Akaishi et al. (2000) synthesized diamonds from graphite and oxalic acid dihydrate at $P$ = 7.7 GPa and $T$ = 1600 °C. The COH volatile speciation of the fluid was analyzed through a quadrupole mass spectrometer by piercing the platinum capsule. The authors observed a significant amount of $CO_2$ produced by OAD, which slightly increases with holding time. After 8 hours, they obtained traces of diamonds. It must be noted that the ratio of $H_2O$ to $CO_2$ could not be determined quantitatively by the QMS analysis. The author reported that complete removal of the adsorbed water in the vacuum chamber was particularly difficult.

Chepurov et al. (2012) investigate serpentine decomposition at high-pressure conditions studying the released aqueous phase. Their chromatographic analysis also comprises COH species such as $CO_2$, CO, $H_2$, $H_2O$, $O_2$, $CH_4$ and other hydrocarbons. The authors

provided quantitative analysis of the COH fluid, including also $H_2O$, as the gas line was thermostated.

Dvir et al. (2013) recently proposed the quartz-tube system (QTS) technique to analyze $H_2O$ and $CO_2$ trapped in a diamond layer from rocking multi-anvil experiments. They employed Au capsules and BN as packing material. The capsules were frozen at $T$ = -90 °C in liquid nitrogen and opened to expose the diamond trap. The fluids were conducted to an infrared gas analyzer by heating the diamond trap at $T$ = 900 °C for at least 60 seconds.

In our experimental study, we choose to analyze the quenched COH fluids through a quadruple mass spectrometer, which ensures superior performances in terms of selectivity of molecules to be detected, high acquisition rates, and extended linear response range. We develop a system to ensure the analysis of water, by keeping the temperature of the reactor and of the connecting line to the QMS at 80 °C.

# 2.2. Experimental procedure

## 2.2.1. Starting material

We chose oxalic acid dihydrate (OAD; $H_2C_2O_4 \cdot 2H_2O$) as the fluid source to generate a 1:1 $H_2O$–$CO_2$ mixture (see Section 1.2.2). Volatile speciation experiments were conducted in the COH system considering four different types of capsule geometry: i) single Au capsule loaded with OAD; ii) single Au capsule loaded with OAD and graphite; iii) single Au capsule loaded with OAD, graphite and an oxygen buffer (iron–wustite, hematite–magnetite or nickel–nickel oxide); iv) double capsules (cf. Eugster & Skippen, 1967) loaded with OAD and graphite in an inner $Au_{50}Pd_{50}$ capsule, and nickel–nickel oxide (NNO) + $H_2O$ in the outer Au capsule. The double capsule technique was also employed for another set of experiments, performed in the MS + COH system, with GCOH fluids in equilibrium with mixture of forsterite with minor enstatite (FoEn, see details in Section 1.2.2). In these runs oxalic acid dihydrate, graphite and FoEn were loaded in the inner capsule. The amounts of loaded materials are given in Appendix (Tables A.1 and A.2).

If an oxygen buffer is loaded into a single capsule together with OAD, the volatile speciation can be calculated through thermodynamic model considering the chemical potential imposed by the oxygen buffer. In double capsule experiments, the oxygen buffer

is not in direct contact with the starting material, which is enclosed in the inner capsule. The $Au_{50}Pd_{50}$ alloy of the inner capsule is permeable to hydrogen, therefore the chemical potential of $H_2$, and not the chemical potential of $O_2$, is expected to be homogeneous in the inner and in the outer capsules. As the inner capsule will contain in general a fluid with species other that $H_2O$, the oxygen fugacity in the inner capsule would be lower compared to the outer capsule (Luth, 1989). We calculated the speciation of the GCOH fluid in the inner capsule through thermodynamic modeling using the software package Perplex (Connolly, 1990; http://www.perplex.ethz.ch/). The routines "vertex" and "fluids" were used first to calculate the fugacity of oxygen and hydrogen fixed in the outer capsule by NNO + $H_2O$ (Perplex equation of state no. 16). As the $fH_2$ imposed by the NNO buffer ($fH_2^{NNO}$) is the same in the inner and in the outer capsule, we were able to calculate the molar fractions of the volatile species and the oxygen fugacity of the GCOH fluid in the inner capsule at the investigated *P* and *T*. For the calculations we considered the thermodynamic dataset of Holland & Powell (1998) revised by the authors in 2004, and an MRK EoS for graphite-buffered COH fluids (Perplex equation of state no. 11; Connolly & Cesare, 1993).

### 2.2.2. Experimental conditions and apparatus

Experiments were carried out in a rocking piston-cylinder apparatus (Schmidt & Ulmer, 2004; Section 1.2.2), at pressures from 1 to 3 GPa and temperatures from 800 to 1000 °C. To investigate the effect of packing materials on the speciation of the COH fluid we choose two different materials to embed the experimental capsule: i) MgO rods drilled to accommodate the capsule and MgO powder to fill the voids (Fig. 2.3A); ii) BN rods and powder, both fired for 2 hours at 800 °C before the experimental run, with MgO spacers at the top and the bottom of the assembly (Fig. 2.3B). A corundum disk is placed at the top of the capsule to avoid the contact with the thermocouple, which could lead to the piercing of the capsule. The furnace consists in a graphite heater, surrounded by NaCl and Pyrex (Fig. 2.3). At the top of the assembly a pyrophyllite plug is placed to ensure electrical contact.

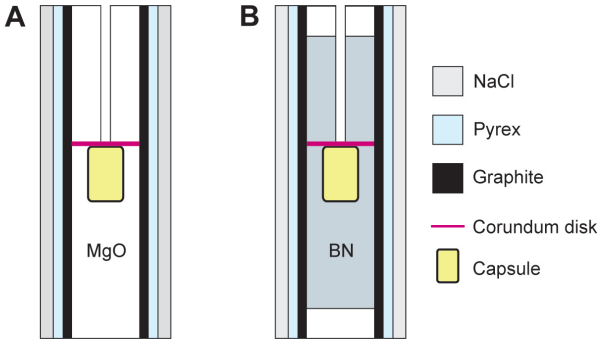


Fig. 2.3. Assembly configuration for speciation experiments. A) MgO; B) BN with MgO top- and bottom spacers.

Samples were first pressurized to $P$ = 0.25 GPa, heated to $T$ = 400 °C and then pressurized and heated simultaneously to the final experimental $P$–$T$ value. Temperature rate was 50 °C/minute until 400 °C and 100 °C/minute to the final value. Temperature was measured with K-type thermocouple sited within 0.6 mm of the capsule and is considered accurate to ± 5 °C. Experiments were performed for a variable run time from 24 to 72 hours (see Table 2.3). Experiments were quenched by turning off the power supply. Quench rate was approximately 40 °C/second.

A set of experiments was performed at ambient pressure. Capsules were heated in a lab oven at $T$ = 250 °C for variable run times from 1 to 2 hours.

After the quench capsules were recovered and cleaned. Experiments performed in MgO were cleaned in HCl and capsules embedded in BN were cleaned with diamond router bits. The outer capsule of double capsule experiments was open and left in oven at 110 °C for 2 hours to completely eliminate the residual $H_2O$ in the oxygen buffer.

### 2.2.3. Analytical technique

To retrieve COH fluids volatile speciation we design a capsule-piercing device connected to a quadrupole mass spectrometer (Fig. 2.4). The capsule-piercing device consists of two parts: i) an extraction vessel (reactor) and ii) an electric furnace where the vessel is allocated (Fig. 2.4B). The reactor, made with Teflon, is composed of a base part, where the capsule is placed (Fig. 2.4D), and a top part, where a steel pointer is mounted (Fig. 2.4C). The capsule, placed horizontally and partially embedded in epoxy, is mounted on cross steel support, designed to oppose the rotation given by the steel pointer during the

piercing (Fig. 2.4D). The furnace is designed with an opening in the base part that permits to close the reactor with a hex key, when the furnace is closed (Fig. 2.4B).

Openings on the top allow the gas carrier to flow inside the reactor and to extract air to generate vacuum conditions. The presence of O-rings ensures a tight seal. The reactor is connected to a QMS through a heated line to avoid condensation of water on the tubes (Fig. 2.5).

The pressure conditions of the line and the reactor are monitored through high-resolution sensor gauges (± 1 mbar error). The temperatures of the line, reactor and furnace are monitored with thermocouples. Line and reactor pressures are monitored through a Eurotherm nanodac$^{TM}$ data recorder with PID control, which also monitors the reactor and furnace temperatures.

The conditions of $P$ and temperature $T$ in the reactor are used to retrieve the total moles of the COH volatile species released from the capsule after piercing. Considering the ideal gas law:

$$n = \frac{PV}{RT} \tag{2.8}$$

at known $P$ and $T$ conditions it is possible to calculate the number of moles ($n$), by knowing the volume ($V$) of the reactor.

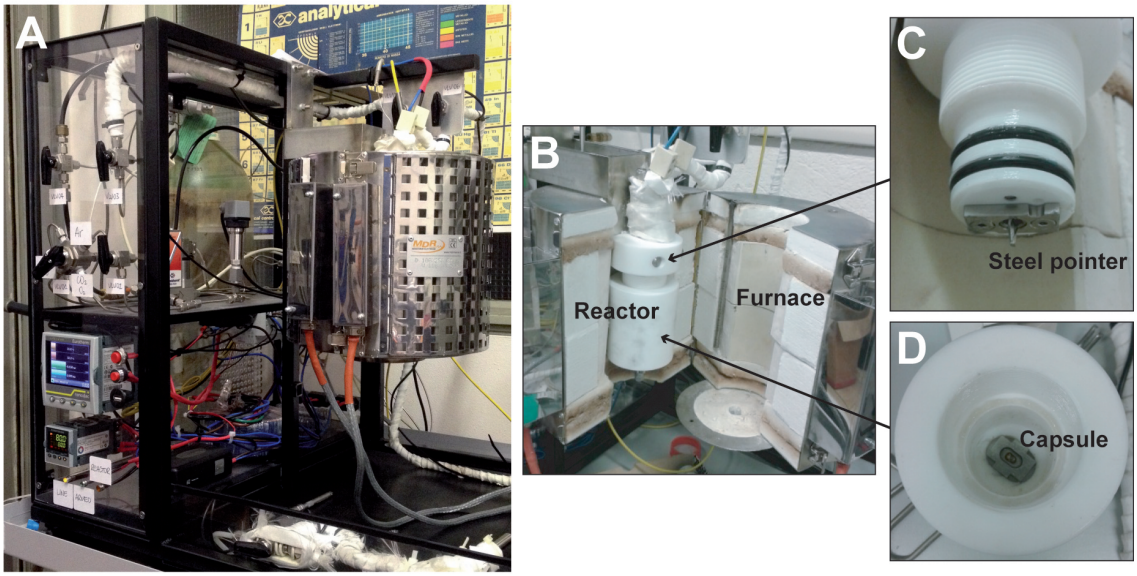


Fig. 2.4. A) The capsule-piercing device and the control panel; B) furnace and the reactor; C) steel pointer mounted on the top of the reactor, with O-rings; D) the base of the reactor with the capsule holder.

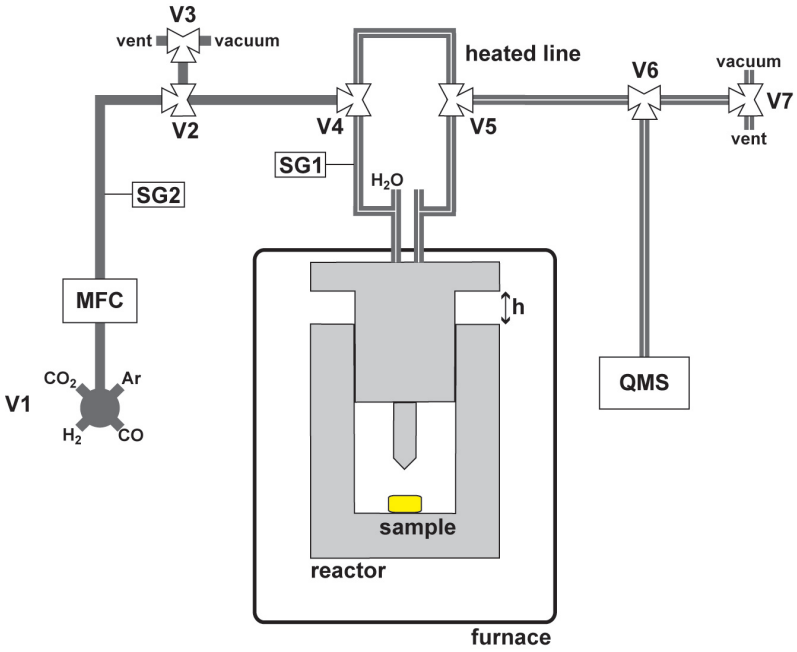


Fig. 2.5. Schematic drawing of the capsule-piercing QMS device; MFC, Mass Flow Controller; SG1, high resolution sensor gauge to measure the reactor pressure; SG2, high resolution sensor gauge to measure the line pressure; V1, four-way valve used to select standard gas-mixtures or the gas carrier; V2, three-way valve to convoyed the gas carrier to the reactor or to V3; V3 and V7, three-way valves to deviate the gas to a vent valve or to a vacuum line; V4 and V5, valves to insulate the reactor during the piercing; V6, three-way valve to convoyed the gas to the QMS or to a vent valve; $H_2O$, silicon septum for injection of $H_2O$ for the calibration; h, know distance between the top and the base of the reactor; QMS, quadrupole mass spectrometer. All the lines are kept heated at 80 °C.

The system is calibrated for quantitative analyses of $H_2O$, $CO_2$, $CH_4$, CO, $H_2$ and $O_2$. The monitored mass/charge (*m/z*) values of interest are reported in Table 2.1.

| *m/z* | species |
|---|---|
| 2 | $H_2$ and fragmentation of $CH_4$ and $H_2O$; |
| 12 | C fragmentation deriving from CO, $CH_4$, $CO_2$; |
| 14 | $CH_4$ and $N_2$ fragmentation. Once the contribution of $CH_4$ is subtracted it is a very useful channel to monitor the quantity of air in the reactor; |
| 15 | exclusively from $CH_4$ (*m/z* = 16 is not monitored because is a very interfered channel); |
| 18 | exclusively from $H_2O$; |
| 20 | exclusively from Ar (in the form of $Ar^{++}$). The channel 40 is not used, as it is a very strong signal. This channel is not used for analytical purpose but it is important to evaluate the stability of the mass spectrometer; |
| 28 | CO, $N_2$ from air and $CO_2$ fragmentation; |
| 32 | exclusively from $O_2$; |
| 44 | exclusively from $CO_2$. |

Table 2.1. Monitored *m/z* channels for the quantitative analyses of COH fluids by means of QMS.

For the calibration of the QMS, we used as standards 3 gas mixtures with know compositions: i) 80 vol% Ar, 10 vol% $CO_2$, 10 vol% $O_2$; ii) 80 vol% Ar, 10 vol% $CH_4$, 10 vol% CO; iii) 90 vol% Ar, 10 vol% $H_2$. Water calibration is performed by loading into the reactor a known amount of water (typically 1 μL), injected with a micro-syringe inserted through a silicon septum present at the top of the reactor (Fig. 2.5).

To extract the COH fluid from the capsule the reactor is placed at a known distance *h* (Fig. 2.5), to be able to retrieve the internal volume of the reactor. Then, the furnace is closed and heated to $T$ = 80 °C. Once that the temperature of the reactor is stable it is possible to clean line and reactor from all the residual gases (e.g., air, residue from the oil of the pump) by performing cycles of pressurization and vent with the gas carrier, argon, using a rotary pump. This procedure must be performed five times with the reactor insulated and five times with the reactor open, to clean all the segments of the device (Fig. 2.5). When the procedure is complete, the reactor is insulated from the line, to be able to monitor the pressure variation inside the reactor once that the capsule is pierced. By rotating the hex key, the base part of the reactor starts to move upward and at some point the steel pointer pierce the capsule. The expansion of the gases release in the reactor causes an increase in pressure, detected by a sensor gauge.

Before connecting the reactor to the line and to the QMS, the reactor has to be rotated counter-clockwise to reach a value of internal pressure close to zero. It is in fact preferable to have a similar pressure in the reactor and in the line when the two are connected. In this way, the gases are convoyed to the QMS only by the carrier gas argon and do not reach the QMS because of their expansion. For every *m/z* channel 310 points are registered, one point every 5 seconds, for a total time of 1550 seconds.

To determine the moles of the COH species we performed an areal balance (Fig. 2.6) considering the total moles of fluid evolved and a matrix that describes the species in terms of *m/z* channels (Table 2.2). We used a weighted least-squares method, where weights take into account that the system has a heteroskedastic distribution of errors, owing to the different analytical uncertainties expected for different components. Monte Carlo simulations provide the propagation of errors for each species, corresponding to the analytical uncertainty.

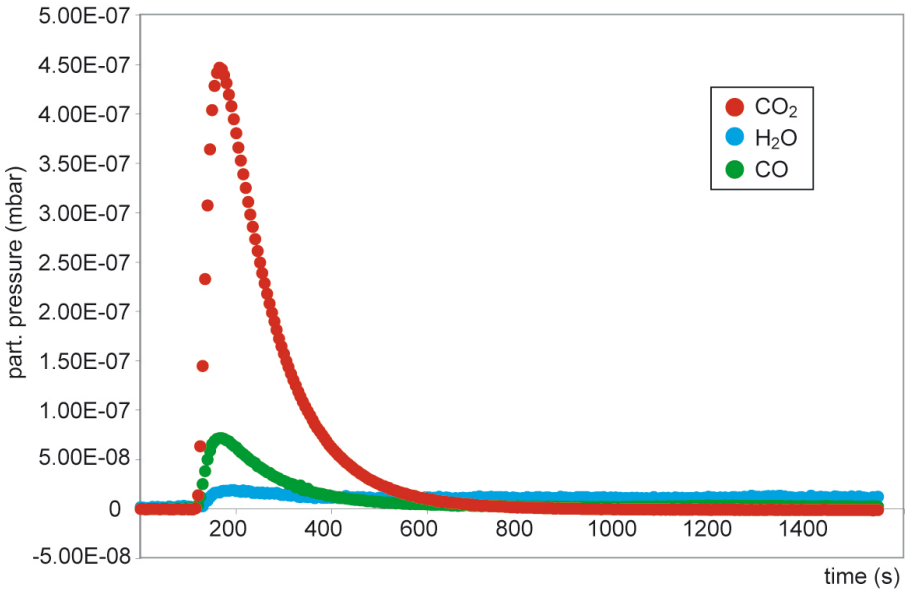


Fig. 2.6. Example of a COH fluid spectrum (experiment CM3) measured through the capsule-piercing QMS technique. The peakes correspond to the piercing, when the fluid is released from the capsule and increases the reactor pressure.

| *m/z* | $O_2$ | $H_2O$ | $H_2$ | CO | $CO_2$ | $CH_4$ | air |
|---|---|---|---|---|---|---|---|
| 2 | 0 | $1.091 \cdot 10^{-7}$ | $3.940 \cdot 10^{-6}$ | 0 | 0 | $5.463 \cdot 10^{-8}$ | 0 |
| 12 | 0 | 0 | 0 | $3.935 \cdot 10^{-8}$ | $6.157 \cdot 10^{-8}$ | $1.441 \cdot 10^{-8}$ | 0 |
| 14 | 0 | 0 | 0 | 0 | 0 | $3.922 \cdot 10^{-7}$ | $1.496 \cdot 10^{-7}$ |
| 15 | 0 | 0 | 0 | 0 | 0 | $8.630 \cdot 10^{-7}$ | 0 |
| 18 | 0 | $7.902 \cdot 10^{-7}$ | 0 | 0 | 0 | 0 | 0 |
| 28 | 0 | 0 | 0 | $1.092 \cdot 10^{-6}$ | $1.513 \cdot 10^{-7}$ | 0 | $8.363 \cdot 10^{-7}$ |
| 32 | $1.016 \cdot 10^{-6}$ | 0 | 0 | 0 | 0 | 0 | $1.534 \cdot 10^{-7}$ |
| 44 | 0 | 0 | 0 | 0 | $1.423 \cdot 10^{-6}$ | 0 | 0 |

Table 2.2. Example of calibration matrix to retrieve the micromoles of the COH species. Numbers represents areas obtained by integrating the signal of each *m/z* channel, analyzing standard gas mixtures.

## 2.3. Results

The experimental conditions investigated are reported in Table 2.3. Quantitative analyses of quenched COH fluids will be provided in the following sections as mol% of the 6 volatile species monitored: $H_2O$, $CO_2$, $CH_4$, CO, $H_2$, $O_2$ and air. Errors are given as $1\sigma$ relative to the mole percentage.

| Run | *P* (GPa) | *T* (°C) | Starting material | Buffer | Assembly | Run time | Run products |
|---|---|---|---|---|---|---|---|
| COH11 | $1 \cdot 10^{-9}$ | 250 | OAD | - | - | 1 | $H_2O + CO_2 + CO$ |
| FM1 | $1 \cdot 10^{-9}$ | 250 | OAD | - | - | 2 | $H_2O + CO_2 + CO$ |
| COH12 | $1 \cdot 10^{-9}$ | 250 | OAD + G | IW | - | 1 | $H_2O + H_2 + CO_2$ |
| COH26 | 1 | 800 | OAD + G | - | MgO | 72 | - |
| COH27 | 1 | 800 | OAD + G | - | BN | 72 | - |
| COH14 | 1 | 800 | OAD + G | IW | MgO | 24 | $H_2O + CH_4 + CO_2$ |
| COH15 | 1 | 800 | OAD + G | HM | MgO | 22 | $CO_2 + H_2O + CO$ |
| COH19 | 1 | 800 | OAD + G | NNO | MgO | 72 | $CO_2 + CO$ |
| COH20 | 1 | 800 | OAD + G | NNO | BN | 72 | $H_2O + H_2$ |
| COH18* | 1 | 800 | OAD + G | NNO | MgO | 21 | $CO_2 + H_2O$ |
| CM3* | 1 | 800 | OAD + G + FoEn | NNO | MgO | 48 | $CO_2 + H_2O + CO$ |
| COH25 | 1 | 900 | OAD + G | - | MgO | 24 | - |
| COH28 | 1 | 900 | OAD + G | - | BN | 24 | - |
| COH32 | 1 | 800 | OAD + G | NNO | MgO | 24 | $CO_2$ |
| COH29 | 1 | 900 | OAD + G | NNO | BN | 24 | - |
| COH30* | 1 | 900 | OAD + G | NNO | MgO | 24 | $CO_2 + H_2O + CO$ |
| CM7* | 1 | 900 | OAD + G + FoEn | NNO | MgO | 21 | $CO_2 + CO + H_2O$ |
| COH16 | 3 | 1000 | OAD + G | NNO | MgO | 24 | $CO_2 + CO + H_2O$ |

Table 2.3. Run table. OAD, oxalic acid dihydrate; G, graphite; IW, iron–wustite; HM, hematite–magnetite; NNO, nickel–nickel oxide. *double capsule experiments. Run times are given in hours.

### 2.3.1. Fluid analyses of unbuffered, single capsule experiments

Two experiments were performed at ambient pressure conditions and at $T = 250$ °C, to analyze the species generated by thermal decomposition of oxalic acid dihydrate without any buffer. Experiment COH11 was left in the oven for 1 hour while experiment FM1 was removed after 2 hours. The calculated air content in the two experiments is similar: 12 mol% in COH11 and 13 mol% in FM1. The composition of the COH fluid consists mainly in $H_2O$, $CO_2$ and CO in both capsules (Table 2.4). In run COH11 the $H_2O$ content is higher (72 mol%), while $CO_2$ and CO are lower compared to experiment FM1.

| | COH11 | FM1 |
|---|---|---|
| μmol tot | 26.34 | 53.76 |
| air (mol%) | 12.01 | 13.22 |
| *mol%** | | |
| $O_2$ | -1.09 (4.28) | 1.90 (0.51) |
| $H_2O$ | 72.19 (3.84) | 56.20 (0.23) |
| $H_2$ | -1.16 (0.78) | 0.68 (0.05) |
| CO | 13.48 (15.81) | 19.24 (2.45) |
| $CO_2$ | 16.46 (2.13) | 21.89 (0.13) |
| $CH_4$ | 0.12 (1.75) | 0.09 (0.21) |

Table 2.4. Thermal decomposition of oxalic acid dihydrate at 250 °C as derived by least-squares modeling. Negative values should be considered zero values. Uncertainties ($1\sigma$) are reported in parenthesis. *on a air-free basis.

### 2.3.2. Fluid analyses of graphite-buffered, single capsule experiments

Experiments performed at $P$ = 1 GPa and $T$ = 800–900 °C, starting from oxalic acid dihydrate and graphite, did not allow reliable COH fluid volatile speciation analyses. The quantity of gases evolved from the capsules is extremely low, and the capsules are only filled with air.

### 2.3.3. Fluid analyses of graphite + oxygen buffered, single capsule experiments

Compositions of the quenched COH fluids generated from oxalic acid dihydrate, graphite and different oxygen buffers are given in Tables 2.5 and 2.6, together with the calculated amount of air present in the charge. Experimental result will be presented according to the oxygen buffer present in the experimental charge.

#### a) Iron–wustite (IW) buffer

Experimental run COH12, performed at $P$ = 1 bar and $T$ = 250 °C, presents a similar amount of air contamination (11 mol%) compared to runs COH11 and FM1, performed at the same $P$–$T$ conditions. The composition of the quenched COH fluid, generated from oxalic acid dihydrate, graphite and IW buffer, is $H_2O$ and $H_2$-rich, with low amounts of $CO_2$ and CO (Table 2.5). Experimental run performed with the same oxygen buffer at high $P$–$T$ conditions (COH14: $P$ = 1 GPa, $T$ = 800 °C) provided a more $CH_4$-rich fluid, with lower $H_2O$ and $H_2$ content compared to experiment COH12 (Table 2.5).

## b) Hematite–magnetite (HM) buffer

The hematite-magnetite buffer, loaded with oxalic acid dihydrate and graphite, generates at $P$ = 1 GPa and $T$ = 800 °C a COH fluid mainly composed of $CO_2$ (65 mol%) and $H_2O$ (26 mol%), with minor CO and $CH_4$ (Table 2.6).

| | COH12 | COH14 | COH15 |
|---|---|---|---|
| buffer | IW | IW | HM |
| μmol tot | 19.58 | 51.11 | 94.63 |
| air (mol%) | 11.17 | 2.18 | 2.99 |
| *mol%** | | | |
| $O_2$ | -0.83 (3.18) | -0.23 (9.93) | 0.10 (6.35) |
| $H_2O$ | 45.60 (2.89) | 35.78 (4.50) | 26.19 (6.49) |
| $H_2$ | 33.18 (0.58) | 1.55 (0.91) | -0.09 (1.32) |
| CO | 9.85 (11.63) | 5.79 (47.17) | 6.69 (20.05) |
| $CO_2$ | 12.21 (1.60) | 24.01 (2.50) | 64.97 (3.60) |
| $CH_4$ | 0.00 (0.26) | 33.10 (4.10) | 2.14 (5.91) |
| MRK model | | | |
| $O_2$ | 0.00 | 0.00 | 0.00 |
| $H_2O$ | 0.40 | 11.5 | 0.00 |
| $H_2$ | 0.00 | 2.40 | 0.00 |
| CO | 0.00 | 0.00 | 0.00 |
| $CO_2$ | 0.00 | 0.00 | 100 |
| $CH_4$ | 99.6 | 86.1 | 0.00 |

Table 2.5. COH volatile speciation in single capsule experiments buffered through the addition of graphite + iron–wustite and graphite + hematite–magnetite as derived by least-squares modeling. Negative values should be considered zero values. Uncertainties (1$\sigma$) are reported in parenthesis. The thermodynamic model of the COH fluid is reported for comparison. *on a air-free basis.

## c) Nickel–nickel oxide (NNO) buffer

Experimental runs performed at $P$ = 1 GPa and temperatures from 800 to 900 °C starting from oxalic acid dihydrate, graphite and nickel–nickel oxide buffer presents different COH fluid compositions on the basis of the packing material used (Table 2.6).

Experimental run performed using MgO as packing material at $P$ = 1 GPa and $T$ = 800 °C (COH19) presents a COH fluid mainly composed by $CO_2$ (96 mol%) with minor CO.

Experimental run COH32 performed with MgO as packing material at $P$ = 1 GPa and $T$ = 900 °C presents also a fluid mainly composed by carbon dioxide. However, in this run the total moles of fluid in the capsule are extremely low, which leads to large uncertainties and fictitious negative values in the least-square model (Table 2.6).

Also experimental run COH16 ($P$ = 3 GPa and $T$ = 900 °C) performed with MgO assembly, presents a $CO_2$-rich fluid (Table 2.6) and large uncertainties.

Experimental runs performed using BN as packing material provided only one reliable analysis of the quenched fluid, i.e. COH20. In fact, in experimental run COH29 ($P$ = 1 GPa, $T$ = 900 °C) the amount of air exceeds the total moles evolved from the capsule.

COH20 performed at 1 GPa and 800 °C generates an aqueous fluid, composed by the 98 mol% of $H_2O$ and minor $H_2$ (Table 2.6).

| | COH19 | COH20 | COH32 | COH29 | COH16 |
|---|---|---|---|---|---|
| assembly | MgO | BN | MgO | BN | MgO |
| μmol tot | 54.95 | 14.01 | 2.03 | 4.06 | 13.44 |
| air (mol%) | 0.78 | 12.61 | 58.3 | 100 | 31.26 |
| *mol%** | | | | | |
| $O_2$ | -0.11 (6.28) | -1.49 (1.14) | -13.64 (37.78) | 12.89 (-3.87) | -0.49 (53.76) |
| $H_2O$ | 0.08 (7.69) | 97.60 (0.52) | -2.26 (32.70) | 35.52 (-1.75) | 3.25 (49.98) |
| $H_2$ | 0.00 (1.56) | 5.25 (0.10) | -0.02 (6.63) | -1.00 (-0.36) | -0.07 (10.12) |
| CO | 4.29 (11.22) | -0.97 (5.40) | -44.16 (143.5) | 56.87 (-18.38) | 16.37 (190.9) |
| $CO_2$ | 95.78 (4.27) | -0.14 (0.29) | 158.72 (18.14) | -4.13 (-0.97) | 80.84 (27.68) |
| $CH_4$ | -0.04 (1.41) | -0.25 (0.47) | 1.36 (29.78) | -0.15 (-1.60) | 0.09 (9.15) |
| MRK model | | | | | |
| $O_2$ | 0.00 | 0.00 | 0.00 | 0.00 | 0.00 |
| $H_2O$ | 0.00 | 0.00 | 0.00 | 0.00 | 64.8 |
| $H_2$ | 0.00 | 0.00 | 0.00 | 0.00 | 0.04 |
| CO | 0.00 | 0.00 | 0.00 | 0.00 | 0.13 |
| $CO_2$ | 100 | 100 | 100 | 100 | 35.0 |
| $CH_4$ | 0.00 | 0.00 | 0.00 | 0.00 | 0.03 |

Table 2.6. COH volatile speciation in single capsule experiments, buffered through the addition of graphite and nickel-nickel oxide as derived by least-squares modeling. Negative values should be considered zero values. Uncertainties ($1\sigma$) are reported in parenthesis. The thermodynamic model of the COH fluid is reported for comparison. *on a air-free basis.

### 2.3.4. Fluid analyses of double capsule experiments

Double capsule experiments were performed using MgO as packing material and NNO as oxygen buffer. COH fluid analyses are reported in Table 2.7.

Experimental runs performed with oxalic acid dihydrate and graphite as starting material (COH18 and COH30) present a COH fluid mainly constituted by $CO_2$ and $H_2O$. In run COH18, the COH fluid is a binary $CO_2$–$H_2O$ mixture (Table 2.7). In this experimental

run the amount of evolved gases from the capsule is low, which lead to a significant uncertainty.

At $T$ = 900 °C (COH30), the COH fluid presents the same $CO_2/H_2O$ ratio measured at $T$ = 800 °C in experimental run COH18 ($CO_2/H_2O$ = 1.4). However, carbon monoxide was detected in higher amounts (~12 mol%; Table 2.7). The analytical error is similar compared to run COH18, even though the evolved fluid from the capsule is higher.

Experiments performed by adding forsterite + enstatite (CM3 and CM7) present different COH fluid compositions compared to the COH-only system.

At $P$ = 1 GPa and $T$ = 800 °C (CM3) the carbon dioxide content is up to 81 mol%, higher compared to the $CO_2$ content in the COH-only system experiment at the same temperature (Table 2.7). In run CM3 the moles evolved from the capsule are significantly higher compared to other experimental runs.

At $T$ = 900 °C (CM7) the COH fluid present a slightly lower amount of $CO_2$ (78 mol%) and $H_2O$ (11 mol%) compared to experimental run CM3. Carbon monoxide is also present, in the same amount of the experiment carried out at the same $P$–$T$ conditions but performed in the COH-only system (COH30).

| | COH18 | CM3 | COH30 | CM7 |
|---|---|---|---|---|
| μmol tot | 2.01 | 26.34 | 83.11 | 16.97 |
| air (mol%) | 59.29 | 3.19 | 8.43 | 7.47 |
| *mol%** | | | | |
| $O_2$ | -8.14 (22.49) | 0.75 (5.31) | -0.34 (24.09) | 0.06 (18.26) |
| $H_2O$ | 48.67 (17.39) | 13.21 (4.60) | 36.92 (21.58) | 10.62 (19.97) |
| $H_2$ | -1.33 (3.52) | -0.39 (0.93) | -1.04 (4.37) | -0.23 (4.04) |
| CO | -8.02 (91.57) | 4.92 (20.17) | 11.82 (88.90) | 11.78 (50.72) |
| $CO_2$ | 69.93 (9.64) | 80.93 (2.55) | 51.95 (11.97) | 77.66 (11.08) |
| $CH_4$ | -1.11 (7.93) | 0.59 (4.19) | 0.69 (9.86) | 0.10 (3.66) |
| MRK model | | | | |
| $O_2$ | 0.00 | 0.00 | 0.00 | 0.00 |
| $H_2O$ | 37.8 | 37.8 | 28.1 | 28.1 |
| $H_2$ | 0.02 | 0.02 | 0.12 | 0.12 |
| CO | 0.49 | 0.49 | 1.4 | 1.4 |
| $CO_2$ | 61.6 | 61.6 | 70.3 | 70.3 |
| $CH_4$ | 0.09 | 0.09 | 0.8 | 0.8 |

Table 2.7. COH fluid volatile speciation in double capsule experiments as derived by least-squares modeling. Negative values should be considered zero values. COH18 and COH30 experiments performed in the COH system. CM3 and CM7 experiments performed in the MS + COH system. Uncertainties (1$\sigma$) are reported in parenthesis. *on a air-free basis.

# 2.4. Discussion

In this section COH volatile speciations are plotted in the COH ternary diagram, together with the analytical error and the composition of the starting material, oxalic acid dihydrate (OAD). Graphite saturation surface and the estimated fluid composition calculated through thermodynamic modeling (Perplex; Connolly, 1990) are also reported.

## 2.4.1. Dissociation of OAD at unbuffered conditions

To investigate the thermal dissociation of oxalic acid dihydrate at low $T$ and ambient conditions we performed two experiments at $T$ = 250 °C starting from OAD: runs COH11 and FM1 (Section 2.3.1). We compared our experimental results retrieved through capsule-piercing QMS technique with data from Morgan et al. (1992), who used different experimental strategy and analytical technique (see Section 2.1.2). For the comparison we considered experiment FM1 (Fig. 2.7B), because it presents a lower uncertainty compared to run COH11 (Fig. 2.7A).

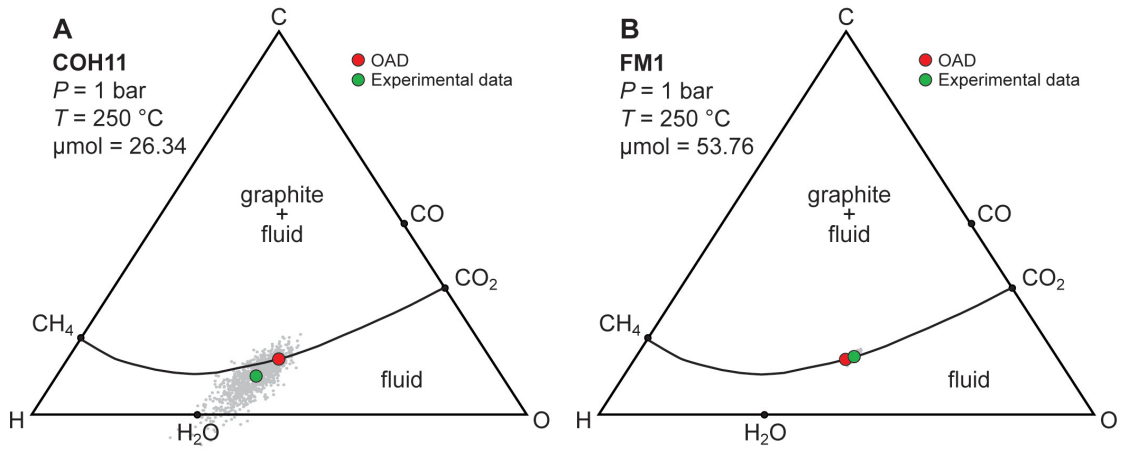


Fig. 2.7. Composition of the COH fluid generated from oxalic acid dihydrate thermal decomposition at 250 °C, plotted on the COH ternary diagram. A) experimental run COH11; B) experimental run FM1. Red dot: theoretical OAD composition; green dot: COH fluid data retrieved by QMS; grey dots: uncertainty cloud. Graphite saturation surface (black solid line) calculated by thermodynamic modeling.

By substituting the coefficients retrieved from COH-fluid analysis of run FM1 in reaction 1.3, which expresses the thermal dissociation of OAD (see Table 2.4), we obtain:

$$0.2\ H_2C_2O_4{\cdot}2H_2O = 0.56\ (\pm 0.002)\ H_2O + 0.22\ (\pm 0.001)\ CO_2 + 0.19\ (\pm 0.024)\ CO + 0.02\ (\pm 0.005)\ O_2 + 0.01\ (\pm 0.001)\ H_2. \quad (2.9)$$

Reaction 2.9 represent the thermal decomposition of OAD retrieved from our experimental data. Compared to reaction 1.3 coefficients are similar, although we also detected some $O_2$ and $H_2$, present in very low amount in the capsule. Morgan et al. (1992) also measured low contents of $H_2$ in their experiments, suggesting that $H_2$ could derives from reaction 1.4.

Combining reaction 1.3 and 1.4, Morgan et al. (1992) proposed the following reaction to account for the formation of $H_2$ in the experimental charge:

$$0.2\ H_2C_2O_4{\cdot}2H_2O = (0.6 - n)\ H_2O + (0.2 + n)\ CO_2 + (0.2 - n)\ CO + n\ H_2 \quad (2.10)$$

where $n$ is a stoichiometric coefficient sensitive to the progress of reaction 1.4 and calculated from experimental data. By substituting in reaction 2.10, the amount of $H_2$ experimental determined from run FM1 ($n = 0.01$) we obtained the following reaction for thermal dissociation of oxalic acid dihydrate:

$$0.2\ H_2C_2O_4{\cdot}2H_2O = 0.59\ H_2O + 0.21\ CO_2 + 0.19\ CO + 0.01\ H_2. \quad (2.11)$$

Reaction 2.11 closely mimics the experimentally determined reaction 2.9.

In Figure 2.8 we compared the COH fluid of experiment FM1, with the data from Morgan et al. (1992). Our experimental results show a good agreement, with the only exception of a slightly lower $H_2O$ content retrieved in our experiment. It is worth to note that Morgan et al. (1992) did not directly measured $H_2O$, which was estimated through mass balance calculation.

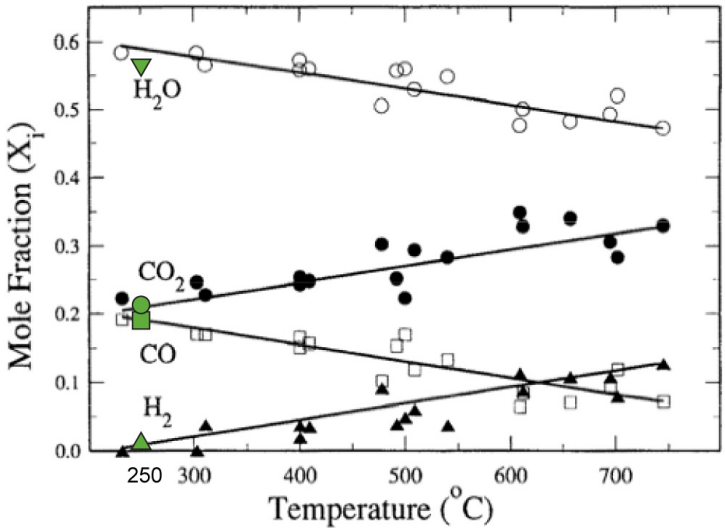


Fig. 2.8. Speciation of the COH fluid generated from the thermal decomposition of oxalic acid dihydrate at 250°C after Morgan et al. (1992). Green symbols represent the COH fluid volatile speciation of run FM1 retrieved through the capsule-piercing QMS device. Analytical error is smaller than symbol size.

## 2.4.2. Dissociation of OAD at buffered conditions

In this section we will discuss COH volatile speciation obtained from graphite + oxygen-buffered experiments in single capsule and from double capsules experiments, starting from oxalic acid dihydrate. We will compare our experimental data with the COH fluid speciation calculated through thermodynamic modeling (Perplex; Connolly, 1990). Experiments performed in single capsules with no oxygen buffer will not be discussed, as the capsules were only filled by air (Section 2.3.2).

### a) Graphite + oxygen buffered, single capsule experiments

#### Iron–wustite (IW) buffered experiments

From a thermodynamic point of view, the addition of IW buffer to the starting material is supposed to shift the composition of the GCOH fluid along the graphite saturation surface towards reduced compositions at ambient pressure and $T$ = 250 °C. Thermodynamic modeling performed at the investigated $P$–$T$ conditions indicates that at $P$ = 1 bar, $T$ = 250 °C (experiment COH12) the GCOH fluid is supposed to be entirely methane, while at $P$ = 1 GPa and $T$ = 800 °C (experiment COH14) minor quantities of water should also be present.

Analysis of experiment COH12 does not reveal methane. The plotted composition of the quenched GCOH fluid is shifted toward more reducing terms compared to oxalic acid dihydrate composition (Fig. 2.9A) and is very close to the calculated graphite saturation surface. The lack of $CH_4$ in the experimental run is probably due to the slow kinetics of methane formation, as experimentally observed by Bernt et al. (1996) during olivine serpentinization at 300 °C and $P$ = 0.05 GPa. The authors estimate that the conversion of $CO_2$ to $CH_4$ through Fischer–Tropsch synthesis (i.e., $CO_2 + 4H_2 = CH_4 + 2H_2O$) may take thousands of years at 200 °C and hundreds of thousands of years at 100 °C. Therefore, at the experimental conditions of the experiment ($T$ = 250 °C) the run time of 1 hour was probably not sufficient to produce methane, not even in trace amount.

In experimental run COH14, performed at $P$ = 1 GPa and $T$ = 800 °C, with a run time of 24 hours, methane is a relevant species in the fluid (33 mol%). However, the plotted composition in the ternary COH diagram does not lie on the graphite saturation surface, suggesting disequilibrium conditions (Fig. 2.9B).

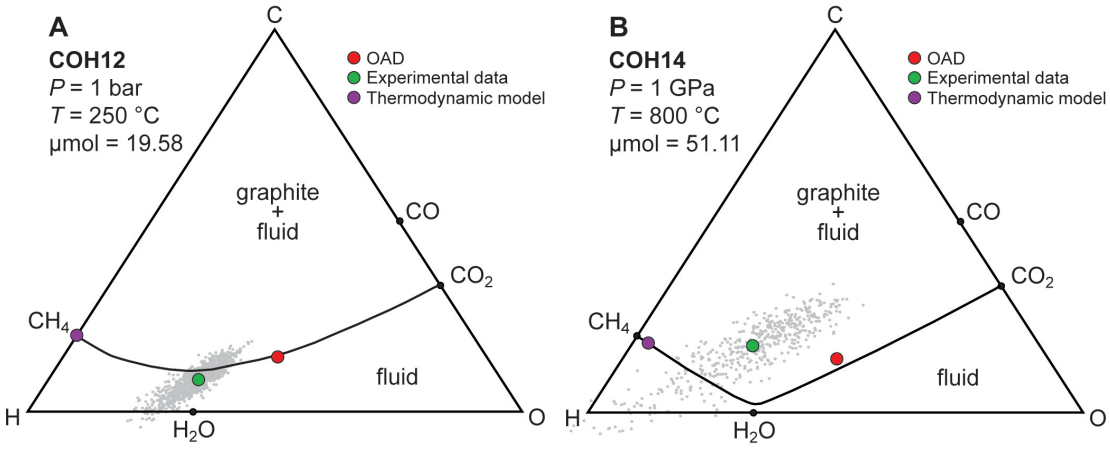


Fig. 2.9. Compositions of the COH fluid generated from graphite + IW buffer plotted on the COH ternary diagram. A) experimental run COH12; B) experimental run COH14. Red dot: theoretical OAD composition; green dot: COH fluid data retrieved by QMS; grey dots: uncertainty cloud. Graphite saturation surface (black solid line) calculated by thermodynamic modeling.

### Hematite–magnetite (HM) buffered experiments

COH volatile speciation starting from OAD, graphite and hematite-magnetite buffer, plot close to the calculated graphite saturation surface in the COH ternary diagram (Fig. 2.10). Although at the investigated conditions ($P$ = 1 GPa and $T$ = 800 °C) thermodynamic modeling predicts a fluid composed entirely of $CO_2$, the analyzed GCOH is mainly composed by $CO_2$ and $H_2O$ in a 5:2 ratio. Carbon monoxide is also present, together with

a small amount of methane (2.15 mol%). The presence of methane in the capsule could be due to interaction between the buffer and the fluid. The employed buffer imposed oxidizing conditions of oxygen fugacity in the charge, however, magnetite could favors the formation of $CH_4$. $H_2$-reduced magnetite is in fact an important catalyzing agent in the production of $CH_4$ from $CO_2$–$H_2$ mixtures (Yoshida et al., 1993), suggested also by the lack of $H_2$ in the COH fluid analysis. However, as the magnetite employed as oxygen buffer is not $H_2$-reduced, the process that intervenes in this case could be more complex than the simple methanation of $CO_2$.

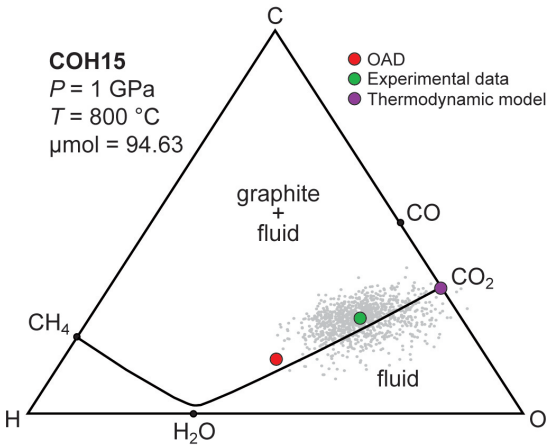


Fig. 2.10. Composition of the COH fluid generated from graphite + HM buffer plotted on the COH ternary diagram. Red dot: theoretical OAD composition; green dot: COH fluid data retrieved by QMS; grey dots: uncertainty cloud. Graphite saturation surface (black solid line) calculated by thermodynamic modeling.

## Nickel–nickel oxide (NNO) buffered experiments

Experimental runs with nickel–nickel oxide buffer, OAD and graphite were performed using both MgO and BN to embed the experimental capsule.

Run COH19, performed using MgO as packing material, shows a COH volatile speciation mainly composed by $CO_2$ (96 mol%) with low amounts of CO (4 mol%). In this case the retrieved experimental speciation agrees with the one predicted by thermodynamic modeling (Fig. 2.11A).

Run COH20, performed at the same *P*–*T* conditions of experimental run COH19 but employing BN as packing material, presents a different COH volatile speciation mainly constituted by $H_2O$ (98 mol%) and $H_2$ (5 mol%), which is very different compared to the model (Fig. 2.11B).

We observed that packing materials have a profound influence on COH volatile speciation. As observed also by Kaegi et al. (2005) MgO impose to the capsule more oxidizing conditions compared to BN. In experiment COH19 the assembly and the buffer impose oxidizing condition, moving the volatile speciation toward $CO_2$-rich fluids. When BN is employed, the oxygen fugacity imposed externally are so reducing that the buffer is not sufficient to move the speciation of the COH fluid toward oxidized terms.

Matveev et al. (1997) also employed BN as packing material in graphite-buffered and graphite + oxygen buffered experiments. The authors considered starting materials with high H/O ratio and employed different oxygen buffers (SiC, IW, WC, CoO), obtaining $H_2O$- and $CH_4$-rich fluids. In this case, the reducing effect of both the oxygen buffers and the packing material allow the composition of the COH fluid to be shifted towards compositions compatible with the thermodynamic model. It is also worth to note that the authors never detect $CO_2$ even where, according to the thermodynamic modeling, fluids were supposed to be a $H_2O$–$CO_2$ mixtures (e.g., CoO buffer at $T$ = 1000°C and $P$ = 2.4 GPa).

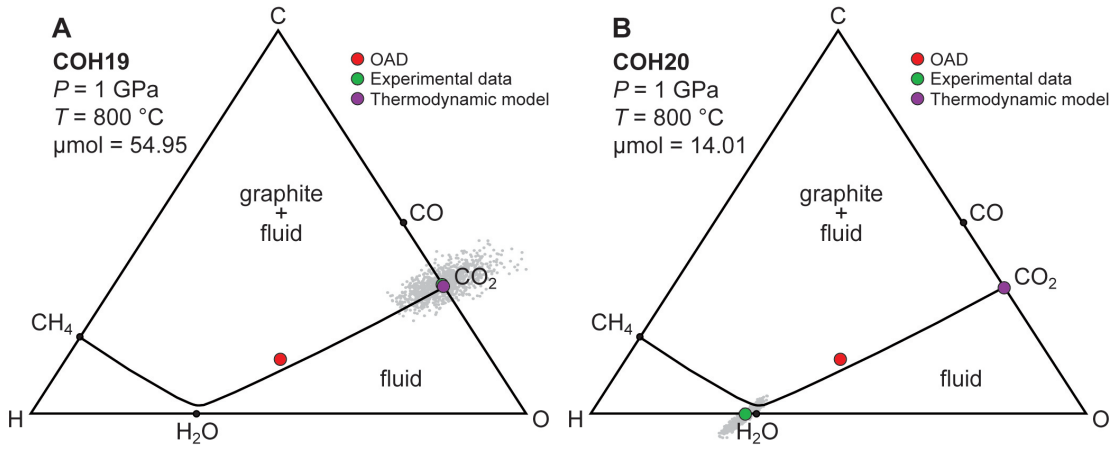


Fig. 2.11. Compositions of the COH fluid generated from graphite + NNO buffer plotted on the COH ternary diagram. A) experimental run COH19, performed with MgO assembly; B) experimental run COH20, performed with BN assembly. Red dot: theoretical OAD composition; green dot: COH fluid data retrieved by QMS; grey dots: uncertainty cloud. Graphite saturation surface (black solid line) calculated by thermodynamic modeling.

Three experiments didn't provide trustworthy COH volatile speciation analyses: COH32, COH16 and COH29.

Runs COH32 and COH16 were performed using MgO as packing material for the same run time (24 hours) at different pressure and temperature conditions. Both the experimental runs present extremely high uncertainty. However, it is not clear if this

calculated high analytical errors are connected to the amount of fluid present in the capsule or not.

The analyzed volatile speciation from experiment COH29 performed using BN as packing material also didn't provide trustworthy COH volatile speciation analyses as the capsule was only filled by air, characteristic also observed in graphite-buffered experiments (Section 2.3.2).

## b) Double capsules experiments

The COH volatile speciation generated by OAD and graphite, buffered at NNO hydrogen fugacity conditions (experiments COH18 and COH30) are very similar to the calculated fluid compositions through thermodynamic modeling (Fig. 2.12A, B). Uncertainties are significantly high, however GCOH fluids plot on the graphite saturation surface, suggesting the achievement of equilibrium in both cases. According to the thermodynamic model the volatile speciation of the GCOH fluid is supposed to move toward $CO_2$ with increasing temperature. In our experiments, this shift does not corresponds to an increase in $CO_2$, but to an increase in CO, not predicted by the model, which suggest the possibility of a riequilibration of the COH fluid during quench. In any case, the volatile speciation plots close to the predicted compositions, so we can consider the double-capsule technique the best method to achieve reliable compositions close to the thermodynamic models.

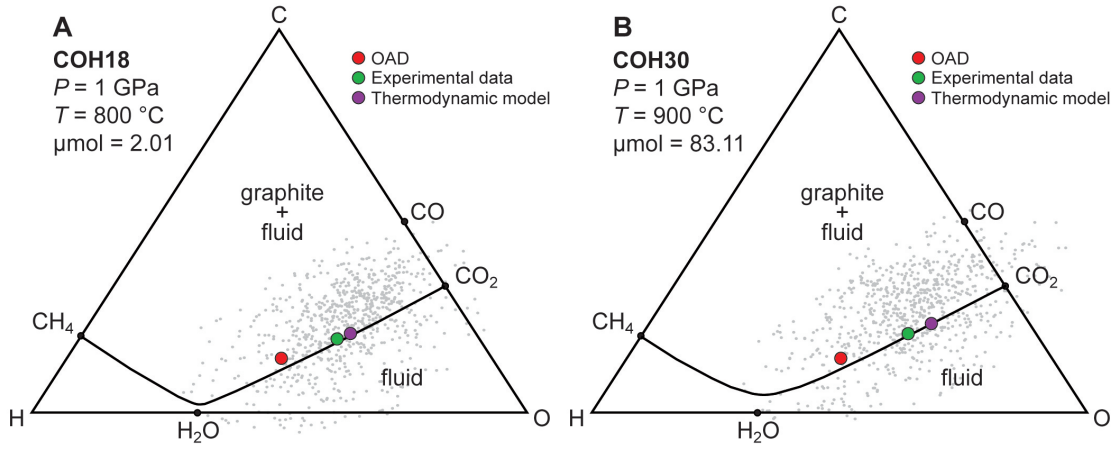


Fig. 2.12. Compositions of the COH fluid generated in double capsules from OAD + graphite at $fH_2^{NNO}$ condition, plotted on the COH ternary diagram. A) experimental run COH18; B) experimental run COH30. Red dot: theoretical OAD composition; green dot: COH fluid data retrieved by QMS; grey dots: uncertainty cloud. Graphite saturation surface (black solid line) calculated by thermodynamic modeling.

Experiments performed by adding in the inner capsule forsterite and enstatite together with OAD and graphite (experiments CM3 and CM7) present a COH volatile speciation shifted toward $CO_2$ compared to the model (Fig. 2.13A, B).

Quenched COH fluids are more $CO_2$-rich also compared to the experimental mineral-free GCOH fluids, maintaining the plotted compositions on the graphite saturation surface. With increasing temperature the experimental GCOH composition is more $CO_2$-rich, as predicted by the thermodynamic model and also observed in experiments in the COH-only system. Moreover, similarly to experiment COH30, the shift in the plotted composition is caused by CO formation.

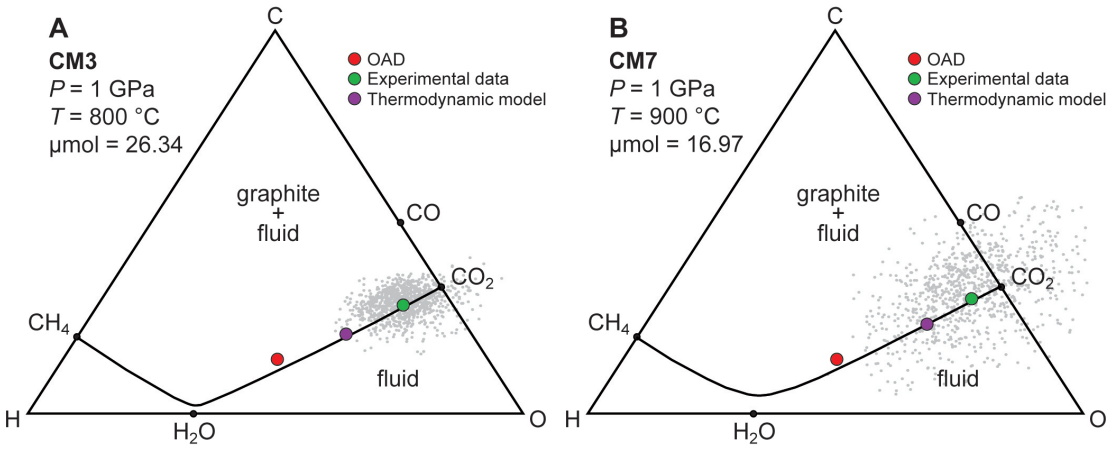


Fig. 2.13. Compositions of the COH fluid generated in double capsules from OAD + graphite + FoEn at $fH_2^{NNO}$ condition, plotted on the COH ternary diagram. A) experimental run CM3; B) experimental run CM7. Red dot: theoretical OAD composition; green dot: COH fluid data retrieved by QMS; grey dots: uncertainty cloud. Graphite saturation surface (black solid line) calculated by thermodynamic modeling.

The composition of the fluid seems to be affected by the addition of forsterite and enstatite to the experimental charge. As displayed in Figure 2.14 experiments performed in the MS + COH system present a consistent shift in the bulk COH compositions toward $CO_2$ compared to the COH-only system.

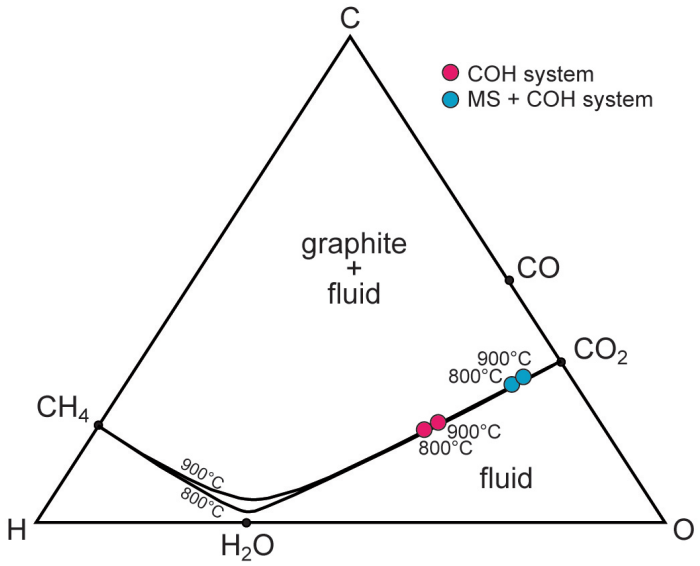


Fig. 2.14. Composition of the COH fluid in the COH-only system and in the MS + COH from double capsules experiments at $fH_2^{NNO}$ condition at $P$ = 1 GPa and $T$ = 800–900 °C, plotted on the COH ternary diagram. Graphite saturation surfaces (black solid line) calculated by thermodynamic modeling.

# Chapter 3

# Solubility of mantle minerals in COH fluids

## 3.1. Introduction

Subduction zones are one of the most dynamic geological settings, as they represent the onset of chemical recycling processes of crustal and volatile elements on Earth. In this setting, COH fluid released from the subducting slab interact with the surrounding rocks and transfer material to the overlying mantle wedge (Poli & Schmidt, 2002). The quantification of the mass transferred by fluids represent a key issue to resolve global geochemical cycles of elements and volatile components. In particular, experimental data on dissolution of mantle minerals represent fundamental information to develop accurate models of the upper-mantle phase relations.

A significant effort has been made to experimentally determine mineral solubility in aqueous fluids at $P$ up to 2 GPa and $T$ up to 1000°C for minerals such as quartz (Manning, 1994), corundum (Becker et al., 1983; Walther, 1997; Tropper & Manning, 2007), calcite (Fein & Walther, 1989; Caciagli & Manning, 2003), apatite (Antignano & Manning, 2008a), rutile (Antignano & Manning, 2008b, Tropper & Manning, 2005; Audétat & Keppler, 2005) and zircon (Newton et al., 2010). Mantle-minerals dissolution in aqueous fluids has been also investigated at $P$ up to 2 GPa and $T$ up to 1300°C by Nakamura & Kushiro (1974), Ryabchikov et al. (1982), Manning & Boettcher (1994) Zhang & Frantz (2000) and Newton & Manning (2002) (see Section 3.1.1).

These data allowed developing thermodynamic models of complex fluid bearing non-volatile species (Dolejs & Manning, 2010; Sverjensky et al., 2014) also based on experimental data on solutes speciation retrieved through Raman spectroscopy (e.g.,

Frantz et al., 1994; Zotov & Keppler, 2000, 2002; Mysen et al., 2013a; Mysen et al., 2013b; Facq et al., 2014).

For mixed $H_2O$–$CO_2$ fluids, the available experimental data only refers to quartz solubility (Walther & Orville, 1983; Newton & Manning, 2000, 2009; Shmulovic et al., 2006) and suggest that $CO_2$ act as diluting phase, lowering the solute content in the fluid without interacting with the solid phase.

In this chapter experimental data in $H_2O$–$CO_2$ mixed fluids on solubility of mantle minerals, namely forsterite, enstatite, magnesite and talc, will be presented to evaluate the effect of $CO_2$ on mineral solubility at different pressure and temperature conditions. We performed high-pressure experiments using a rocking piston-cylinder apparatus at $P$ = 1–2.1 GPa and $T$ = 700–1200 °C in the MS + COH system at buffered hydrogen fugacity conditions. Fluid and solutes, trapped in a porous diamond layer, were analyzed using the cryogenic laser-ablation inductively plasma mass spectrometry (LA-ICP-MS) technique (Kessel et al., 2004, 2005a; 2005b; Melekhova et al., 2007; Aerts et al., 2010).

### 3.1.1. Experimental background on mineral solubility

#### a) Mineral solubility in aqueous fluid

The first contributions to mineral solubility at high-pressures came from the experimental studies of Kennedy et al. (1962) and Anderson & Burnham (1965), who studied the system $SiO_2$–$H_2O$. Experiments were conducted in internally heated pressure vessels (IHPV) at $P$ from 0.2 to 1 GPa and $T$ from 500 to 1000 °C. Crushed crystals of quartz were enclosed in a perforated Au capsule, weighted and then sealed inside another Au capsule containing distilled water. After the experimental run the inner capsule was retrieved and weighted, dried and then reweighted. The measured weight difference provided the amount of $SiO_2$ dissolved into water. This procedure, know as the weight-loss technique, became one of the standard method to measure mineral solubilities (e.g., Manning, 1994; Caciagli & Manning, 2003, Newton & Manning, 2002).

Manning (1994) extended the pressures range of solubility experiments to 2 GPa using a piston-cylinder apparatus. Runs were performed in pure $H_2O$ at $T$ = 500–900 °C using rapid-quench rates, to avoid the precipitation of solutes from the fluid. The quench-rate has been reported to be a key issue in solubility experiments. Anderson & Burham (1965), who imposed long quench times (8–10 min) to their experiments, probably underestimated the solubility of quartz below 1 GPa (Manning, 1994). Nevertheless, the

two experimental works of Anderson & Burnham (1965) and Manning (1994) provide a comprehensive dataset of quartz solubility in aqueous fluid, at *P* and *T* condition corresponding to the deep crust and upper mantle.

The MS + $H_2O$ system was studied first by Nakamura & Kushiro (1974), who deduced the composition of the fluid phase at 1.5 GPa and 1280–1340 °C from the location of phase boundaries in the system MgO–$SiO_2$–$H_2O$ and projected to the $H_2O$–$SiO_2$ subsystem axis. The authors observed that the fluid in equilibrium with forsterite and enstatite is able to dissolve up to 20 wt.% of $SiO_2$ at the investigated conditions. Ryabchikov et al. (1982) extended the pressure range of the study of Nakamura & Kushiro (1974) to *P* = 3 GPa, using the same technique to estimate the fluid composition. The authors observed that in the MS + $H_2O$ system, the Mg/Si ratio slightly increases with pressure. At 3 GPa and 1000 °C the Mg/Si ratio equals 1, dissolving more than 30 wt.% of silicates.

Manning & Boettcher (1994) measured the solubility of a forsterite + enstatite assemblage in $H_2O$, from piston-cylinder experiments at *P* from 1 to 3 GPa and *T* from 700 to 1310 °C. To retrieve the solubility of these minerals the authors developed a device to extract both fluids and precipitates from the capsule, analyzed by means of inductively coupled plasma (ICP) mass spectrometry. Experimental data showed that at the investigate conditions the concentration of MgO in the solution is negligible (< 200 ppm), compared to $SiO_2$ solubility ($m$$SiO_2$ = 0.071 mol/kg at *P* = 1 GPa and *T* = 700 °C).

Zhang & Frantz (2000) retrieved the fluid composition in the MS + $H_2O$ system from the compositional boundaries of the assemblages projected to the $H_2O$–$SiO_2$ subsystem axis, as done by Nakamura & Kushiro (1974), assuming that MgO concentrations in the fluid is negligible at the investigated condition (*P* = 1–2 GPa, *T* = 900–1200 °C). The authors highlighted that the thermodynamic properties of aqueous silica derived from silica-saturated systems may not be applicable to calculation in silica-deficient systems at high-pressure conditions.

Newton & Manning (2002) applied the weight loss technique (see Manning, 1994) to retrieved the solubility of forsterite + enstatite from 0.4 to 1.5 GPa and *T* from 700 to 900 °C. The obtained aqueous silica exhibits negative, composition-dependent, departures from ideality. Solubility data reported by Newton & Manning (2002) and Zhang & Frantz (2000) present some discrepancies that Newton & Manning (2002) attributed to the quenching method employed by Zhang & Frantz (2000). In fact, decreasing temperature

at nearly constant pressure could lead to the formation of hydrothermal enstatite, as the quench *P, T* path will pass through the equilibrium field of enstatite. The presence of post-quench enstatite could have caused a misinterpretation of phase equilibrium boundaries by Zhang & Frantz (2000).

Although in the presented study we focus on experiments carried out at pressure conditions which do not exceed ~ 2 GPa, it is worth noting that another experimental techniques has been used to investigate the system MS + $H_2O$ at significantly higher-pressures, up to 10 GPa, where the dissolution of solids in supercritical fluids become so elevated that a distinction between aqueous fluid and silicatic melt becomes meaningless. Stalder et al. (2001) employed diamond-trap experiments to investigate the MS + $H_2O$ system at $P$ = 6–10.5 GPa and temperatures from 900 to 1200 °C. Diamond-trap experiments contain a diamond-powder layer in the capsule (Baker & Stolper, 1994), where precipitates and melt are trapped and subsequently analyzed through LA-ICP-MS. The system MS + $H_2O$ was also investigated by Melekhova et al. (2007) from 11–13.5 GPa, applying the "freezing technique" proposed by Kessel et al. (2004). The technique consists in freezing the capsule before open it, and analyzing the solute content in frozen fluids, trapped into the diamond layer, by LA-ICP-MS (other details in Section 3.2.3).

## b) Mineral solubility in COH fluids

Compared to experimental data in the $H_2O$-only system, mineral dissolution in COH fluid has been investigated by few authors. In this section an overview on mineral solubility in presence of a COH fluid will be provided.

Walther & Orville (1983) developed an extraction quench-hydrothermal apparatus to analyze the solubility of quartz in $CO_2$–$H_2O$ mixed fluids by extracting the fluid. In these experiments, performed in cold seal vessel, the pressure was limited to 0.2 GPa at $T$ < 600 °C. The authors observed a decrease in quartz solubility by increasing the amount of $CO_2$ in the COH fluid. Authors did not report any interaction between dissolved silica and the diluting volatile ($CO_2$).

Concerning *P–T* conditions similar to our experimental study, Schneider & Eggler (1986) investigated the solubility of different types of peridotites (amphibole, phlogopite and jadeite peridotites) and single minerals in mixed $H_2O$–$CO_2$ fluids at $P$ = 1.5–2 GPa and $T$ = 600–1100 °C. The collected solutes extracted from the capsule were mixed with $LiBO_2$ and fused in graphite capsule at $T$ = 1000 °C for 10 minutes. WDS analyses were

performed through electron microprobe. The authors observed that the addition of $CO_2$ to the aqueous fluid strongly depressed the solubility of silicates by approximately one order of magnitude.

Aranovich & Newton (1999) determined activity-compositions relations in $CO_2$–$H_2O$ solutions by modifying the weigh loss technique. The capsule was frozen in liquid nitrogen and punctured with a needle while still frozen. The immediate weight loss is ascribed to $CO_2$ escape. The capsules were then dried and reweighed to retrieve the $H_2O$ content.

Newton & Manning (2000, 2009) investigate quartz dissolution in $H_2O$–$CO_2$ using the above puncture-weight loss technique applied on double capsules at $P$ = 0.2–1.5 GPa and $T$ = 500–900 °C. The amount of $SiO_2$ in the fluid decreases strongly with increasing $CO_2$, in agreement with previous experimental data.

For what concerned other mineral solubility in mixed fluids it is worth to report the work of Caciagli & Manning (2003), who studied calcite dissolution in pure $H_2O$ up to $P$ = 1.6 GPa and $T$ = 500–900 °C. Authors reported that the dissolution of calcite formed $CO_{2(aq)}$ thus leading to the formation of a $H_2O$–$CO_2$ mixed fluid (see Section 3.4.4). Solubility obtained by weigh loss technique (Manning, 1994) is up to 0.6 wt.% of calcite dissolved in water at $P$ = 1 GPa.

# 3.2. Experimental procedure

## 3.2.1. Starting material

For this experimental study, two starting materials were used: i) a mixture of forsterite and minor enstatite (FoEn) and ii) a mixture of enstatite, magnesite and minor forsterite (EnMag) (see Section 1.2.1).

Carbon-saturated GCOH fluids were generated from oxalic acid anhydrous (OAA, $H_2C_2O_4$), $H_2O$ and graphite (glassy carbon spherical powder, grain size 80–200 μm). A layer of diamond crystals with grain size of 20 μm was placed between two layers of the starting material to collect the fluid in equilibrium with solid phases. The thermal dissociation of OAA at high temperature generates a $CO_2$–$H_2$ 2:1 fluid according to reaction 1.6.

$H_2O$ was added to obtain a roughly equimolar $CO_2$–$H_2O$ 1:1 mixture in the capsule. Since the cryogenic LA-ICP-MS technique (Kessel et al., 2004, 2005a; 2005b; Melekhova et

al., 2007; Aerts et al., 2010) requires the use of an internal standard, to determine the amount of solutes trapped into the diamond layer, water was doped with 585 ppm of cesium (from CsOH) and its concentration was checked by means of ICP-MS. By knowing the initial Cs/$H_2O$ ratio it is possible to retrieve the amount of solutes in the laser spot, because cesium is a highly incompatible element that will exclusively partition into the fluid phase (Kessel et al., 2004; more details in Section 3.2.3).

All experimental runs were performed at fluid-saturated conditions, with fluid/solids ratio ~ 20 wt.%. Redox conditions were controlled employing the double capsule technique and nickel-nickel oxide (NNO) buffer. The inner $Au_{50}Pd_{50}$ capsule was loaded with FoEn/EnMag, OAA, $H_2O$, graphite and diamonds. Weighted quantities of the loaded materials are given in Appendix, Table A.3. The outer capsule (Au at $T$ < 1000 °C, Pt at $T$ > 1000 °C) contains the inner capsule, the hydrogen buffer NNO and $H_2O$ (Fig. 3.1).

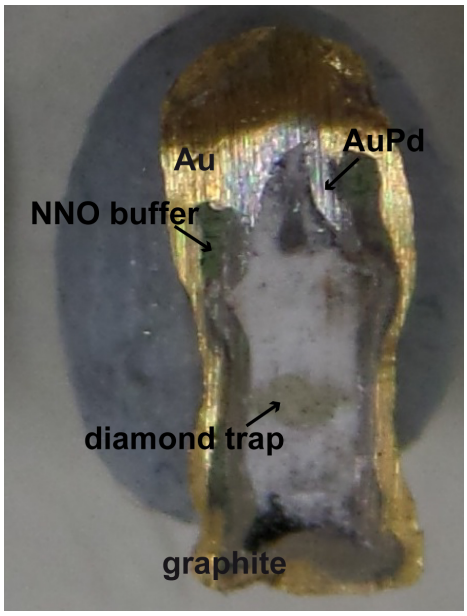


Fig. 3.1. Longitudinal section of a double capsule (experiment CZ11). At the bottom of the capsule, graphite spheres. The diamond layer is placed approximately at the center of the capsule, between two layers of starting material FoEn or EnMag. NNO buffer is placed at the top of the outer capsule.

NNO fixes the chemical potential of $H_2$ ($fH_2^{NNO}$) in the $H_2O$-only fluid of the outer capsule. The AuPd alloy of the inner capsule is permeable to hydrogen, therefore the chemical potential of $H_2$ is expected to be homogeneous in the inner and in the outer capsules. Therefore, since the inner capsule will contain in general a fluid with COH species in addition to $H_2O$, the oxygen chemical potential in the inner capsule will be lower (cf. also Luth, 1989) and can be calculated by thermodynamic modeling along with

the volatile speciation of the GCOH fluid. We used the software package Perplex (Connolly, 1990; http://www.perplex.ethz.ch/) and the routines "vertex" and "fluids" to calculate GCOH fluid speciation. Predicted fluids are mainly composed of $H_2O$ and $CO_2$, with different $XCO_2$ [= $CO_2$/ ($CO_2$ +$H_2O$)] ratios in function of $P$ and $T$ (Tables A.4 and A.5). In Figure 3.2, we show a calculated $P$–$T$ phase diagram of the MS + COH system saturated with a GCOH fluid, the thermodynamic dataset of Holland & Powell (1998) revised by the authors in 2004 and an MRK EoS for graphite-buffered COH fluids (Perplex equation of state no. 11). Since the composition of the GCOH fluid is a function of the oxidation state of the system, we imposed in the calculation the $fO_2$ retrieved by thermodynamic modeling, fitted in the following equation:

$$\ln fO_2 = 14.3 + (-60600 + 0.324808P) / T \quad (3.1)$$

($P$ in bar and $T$ in K).

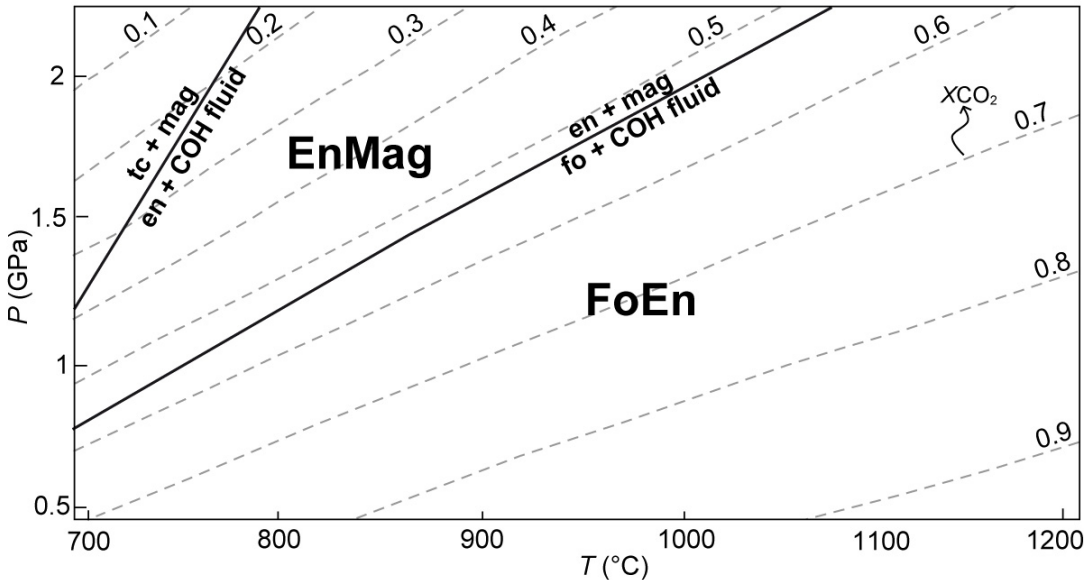


Fig. 3.2. Calculated $P$–$T$ diagram of the MS + COH system saturated with GCOH fluid, simulating the conditions in the inner capsule, controlled externally by the NNO buffer. Solid line: calculated reactions in the COH system. Dashed gray lines represent $XCO_2$, estimated by thermodynamic modeling of a pure GCOH fluid externally buffered by nickel-nickel oxide.

In the calculated diagram we found two univariants:

forsterite + COH fluid = enstatite + magnesite (3.2)

enstatite + COH fluid = talc + magnesite (3.3)

where the COH fluid is a $H_2O$–$CO_2$ mixture with variable $XCO_2$ as represented in Figure 3.2.

The two univariants were used as a guideline to select the starting material, either FoEn or EnMag. At *P*–*T* conditions above and below reaction 3.3, EnMag and FoEn were used respectively.

### 3.2.2. Experimental conditions and apparatus

Experiments were carried out in a rocking piston-cylinder apparatus at pressures from 1 to 2.1 GPa and temperatures from 700 to 1200 °C. Rocking piston-cylinder apparatus was employed to allow a better homogeneisation of the fluid in the experimental charge through a rotation of 180° of the entire structure of the piston-cylinder (see Section 1.2.2). During the heating phase the piston-cylinder rotated continuously (one turn of 180° every 30 s), then the rotation rate was switched to 99 seconds. Experiments were performed for an average run time of 48 h. Quench rates are variable from 25 °C/second to 40 °C/second at higher temperature conditions ($T$ > 1000 °C). The assembly consists in NaCl, Pyrex, a graphite heater and graphite disks at the bottom. Capsule was embedded in MgO rods filled with MgO powder.

After the experimental run the recovered capsule was rinsed in HCl solution for 5 hours and cleaned with diamond router bits to eliminate the residual MgO from the assembly.

### 3.2.3. Analytical technique

The solute content in the fluid was measured through the cryogenic laser-ablation ICP-MS technique also known as “freezing technique” (Kessel et al., 2004). The recovered experimental capsule is mounted on a freezing stage (Fig. 3.3), which consists of a stack of two Peltier elements, surrounded by plastic to thermally insulate the elements from the atmosphere. The sample holder is placed on a copper block, in direct contact with Peltier elements and cooled to $T$ = -35 °C. A longitudinal cross-section of the capsule is exposed using a cutter blade mounted on a steel support (Fig. 3.3A). This device, called the “guillotine”, permits to cut easily double capsule, by fasten a screw that push a steel block and the cutter blade through the capsule. During this operation the capsule is enclosed in a copper support (Fig. 3.3B). Once that the capsule is opened, the device is removed from the freezing stage together with the upper part of the capsule holder. The upper half of the

capsule is checked at the optical microscope, while the lower part remains on the freezing stage for laser ablation analyses (Fig. 3.3C) and will remain frozen during the entire analytical session. Element concentration ratios were obtained by external standardization (NIST SRM610).

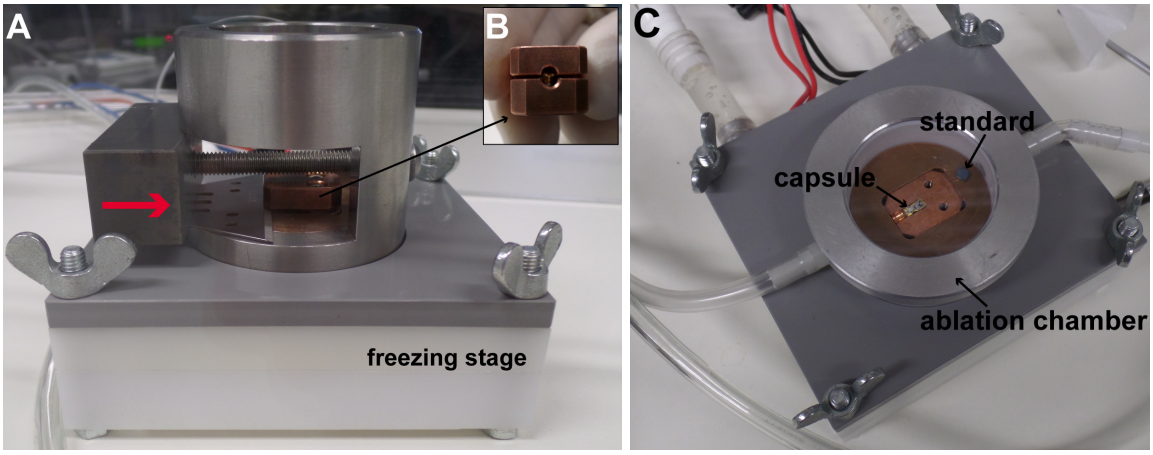


Fig. 3.3. A) the "guillotine" device mounted on the freezing stage, the red arrow indicates the direction of the cut; B) Capsule holder; C) The freezing stage ready for the laser-ablation analysis.

Analyses were performed at the Institute of Geological Sciences, University of Bern (Switzerland) using a 193 nm ArF GeoLas Pro excimer laser system coupled to an ELAN DRCD-e quadrupole mass spectrometer. Details on the instrument setup and operating conditions are given in Pettke et al. (2012). We analyzed the diamond trap for $^{24}$Mg, $^{25}$Mg, $^{26}$Mg, $^{29}$Si, $^{62}$Ni, $^{133}$Cs, $^{195}$Pt and $^{197}$Au, using a 60 µm beam diameter and 5 Hz repetition rate. Data were acquired in blocks of up to ~10 individual sample analyses bracketed by three analysis of the standard NIST SRM610, placed in the ablation chamber with the sample (Fig. 3.3C). Background was taken for roughly 50 seconds and the sample signal, on the diamond trap (Fig. 3.4A) or on the solid residue (Fig. 3.4B), was collected for 20 seconds. Data reduction was performed using the software Sills (Guillong et al., 2008; http://www.geopetro.ethz.ch/research/orefluids/software). Background and signal time interval were selected manually to calculate the concentration of each element (Fig. 3.4). The background count rates were subtracted from the signal count rates to obtain background-corrected counts for each element analyzed.

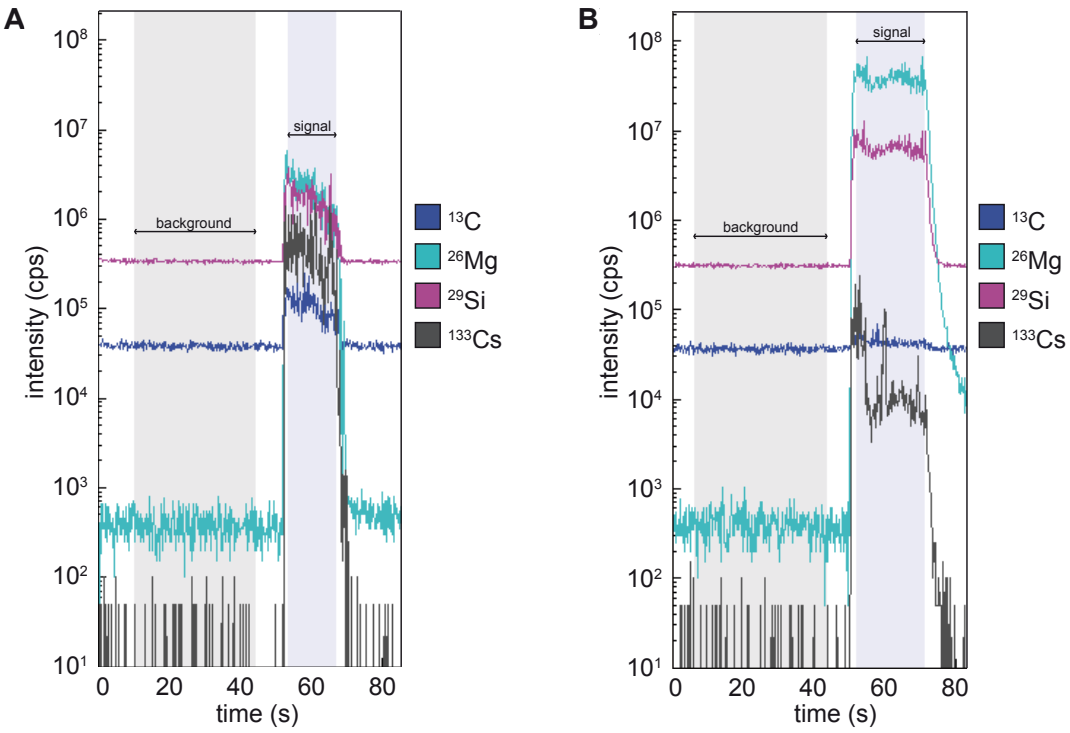


Fig. 3.4. Example of LA-ICP-MS intensity (counts) *vs.* time (seconds) spectra for the diamond trap (A) and for the solid residue (B) using 60 µm diameter laser beam.

To determine the concentrations in the fluid an internal standard, cesium, was considered. The measured Cs concentration in the frozen fluid allows determining the amount of $H_2O$ presents in the laser spot, i.e., the $H_2O$/diamond ratio. To retrieve the amount of fluid in the trap, a known concentration of Cs is added to the capsule using an aqueous solution of CsOH. Cs is a highly incompatible element in the systems investigated so far through the freezing approach (eclogitic system + $H_2O$, Kessel et al., 2004, 2005a, 2005b; MS + $H_2O$ system, Melekhova et al., 2007, $SiO_2$ + $H_2O$, Aerts et al., 2010). Cs strongly partitions into the fluid phase, which is assumed to presents the same Cs/$H_2O$ ratio of the solution loaded into the capsule. In experiments with only $H_2O$ as a fluid phase the Cs/$H_2O$ ratio is fixed. Consequently it is relatively easy to determine the amount of fluid analyzed in the laser spot, once the concentration of cesium is known. However, in double capsule experiments this assumption is no longer valid as the amount of fluid in the inner capsule can vary according to the hydrogen fugacity conditions imposed by the external buffer. In fact, in double capsule arrangements $H_2$ is a mobile component that can be added or removed from the system. Therefore, the Cs/$H_2O$ ratio is no longer fixed.

In this experimental study, the double-capsule technique is employed to constrain the composition of a graphite-saturated GCOH fluid at $fH_2^{NNO}$ (see Section 3.2.1). GCOH

fluids at the investigated conditions are mainly composed of $H_2O$ and $CO_2$. For example, if NNO buffer imposes a fluid more $H_2O$-rich compared to the starting composition, $H_2$ will be added to the inner capsule through the capsule wall, which would lead to a more diluted solution of Cs, with a lower $Cs/H_2O$ ratio compared to the solution loaded in the experimental charge. Obviously this is a complication that, if not corrected, can affect profoundly the interpretation of the analyses. Moreover, the temperature reached by the freezing stage ($T$ = -35 °C) is not sufficient to freeze $CO_2$, which is expected to leave the capsule once opened. Consequently the analyses retrieved refer to the aqueous fraction of the COH fluids.

To estimate the actual $Cs/H_2O$ ratio in our experiments we considered two assumptions. The first is that fluid equilibration at NNO hydrogen fugacity condition is governed only by $H_2$ mobility. The second is that no hydration or carbonation reactions occur in the capsule charge (some considerations in case of carbonation or hydration of the starting material are provided in Section 3.4.3). As long as these two assumptions are valid, it is possible to estimate the amount of Cs in the inner capsule as follows.

We consider a classic dilution equation:

$$C_i\mathrm{Cs} * V_i\mathrm{H_2O} = C_f\mathrm{Cs} * V_f\mathrm{H_2O} \quad (3.4)$$

where $C_i$Cs is the initial concentration of Cs in the aqueous solution loaded into the capsule and $C_f$Cs is the final concentration of Cs after fluid equilibration at NNO $fH_2$ conditions. $V_i$H$_2$O and $V_f$H$_2$O are the initial and final volume of water.

The volume of water is proportional to the moles:

$$V\mathrm{H_2O} = n\mathrm{H_2O} * V_{mol}\mathrm{H_2O} \quad (3.5)$$

($V$H$_2$O, volume of water; $n$, number of H$_2$O moles; $V_{mol}$H$_2$O, molar volume of water).

Considering that at fixed pressure and temperature conditions, the molar volume of water is the same we obtain the following dilution equation:

$$C_i\mathrm{Cs} * n_i\mathrm{H_2O} = C_f\mathrm{Cs} * n_f\mathrm{H_2O} \quad (3.6)$$

The final Cs concentration will be given by:

$$C_f\mathrm{Cs} = \frac{C_i\mathrm{Cs} * n_i\mathrm{H_2O}}{n_f\mathrm{H_2O}} \quad (3.7)$$

and

$$C_f\mathrm{Cs} = \frac{C_i\mathrm{Cs} * n_i\mathrm{H_2O}}{\left(\frac{X\mathrm{H_2O} * n_i\mathrm{CO_2}}{1 - X\mathrm{H_2O}}\right)} \quad (3.8)$$

$C_i$Cs is a constant value fixed at 585 ppm. $n_i$H$_2$O and $n_i$CO$_2$ are known values, resulting from the amount of OAA and H$_2$O introduced in the capsule. $X$H$_2$O is calculated through thermodynamic modeling. $C_f$Cs is the final concentration of Cs in the inner capsule. As shown in Figure 3.5 the concentration of Cs decreases with increasing value of $X$H$_2$O in the COH fluid.

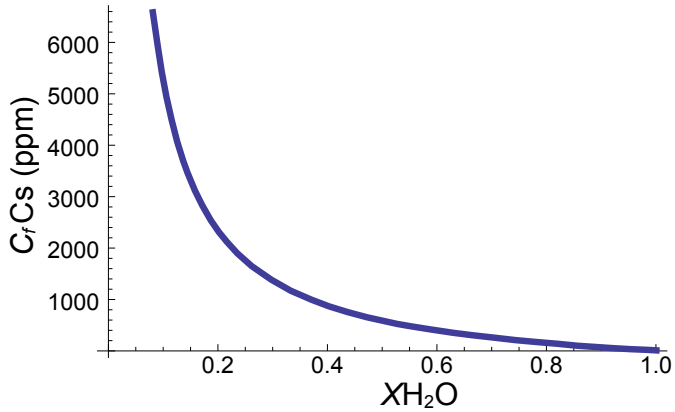


Fig. 3.5. $X$H$_2$O *vs.* $C_f$Cs. Increase in $X$H$_2$O leads to lower Cs concentration in the inner capsule.

Once that the real Cs concentration is know, the solute content has to be recalculated according to the amount of water presents in the laser spot. Three Mg isotopes considered during LA-ICP-MS analyses could be affected by the presence of carbonic fluid phases, diamonds and air (e.g., the humidity condensate during the capsule cut). $^{24}$Mg could be affected by ($^{12}$C$^{12}$C), $^{25}$Mg by ($^{12}$C$^{13}$C) and $^{26}$Mg present the potential interferences of ($^{13}$C$^{13}$C) and ($^{12}$C$^{14}$N). To limit the effect of interferences in the measures we selected the results that provide the lowest, most reliable Mg/Si ratio.

Capsules were also observed at the electron microscope (JEOL8200 Superprobe, University of Milan), to inspect the diamond trap and the eventual presence of precipitates in the diamond layer. Then the capsules were embedded in epoxy and polished, in order to performed WDS electron microprobe analyses and X-ray maps of elements. To evaluate the relative abundances of minerals in the experiments we carried out principal component analysis (PCA) on X-ray maps. PCA is a statistical procedure

that transforms a number of possibly correlated variables into the same number of uncorrelated variables (*eigenvectors*), characterized by different importance (*eigenvalues*) and called principal components. Through principal component analysis the data are expressed through a new Cartesian system were the first principal component (F1) accounts for as much of the variability in the data as possible, and each for each succeeding component (F2, F3,…) accounts for as much of the remaining variability as possible. An example of application of PCA to X-ray maps is shown in Fig. 3.6. PCA data were used to perform image analysis, where each pixel of the image is classified and clustered to a particular phase.

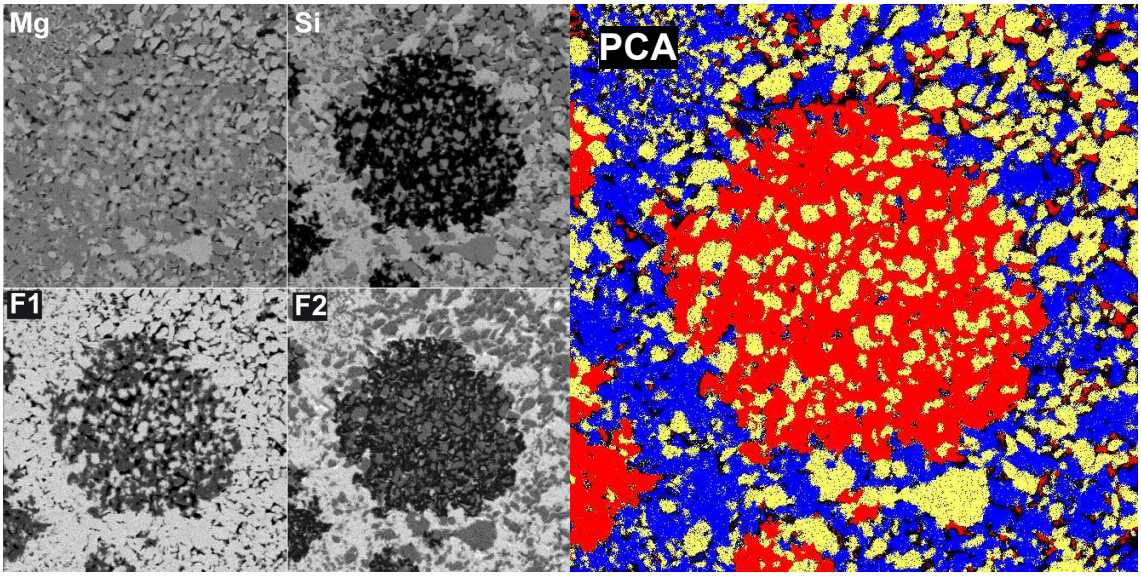


Fig. 3.6. Principal components F1 and F2, derived from X-ray maps of Mg and Si and the resulting principal component analysis, where is possible to distinguish between the different minerals present in the map (forsterite is displayed in yellow, enstatite in blue and magnesite in red).

We checked the experimental runs for the post-quench integrity of the oxygen buffer in the outer capsule, looking for nickel and nickel hydroxide (Fig. 3.7). The buffer was found in all samples at $T < 1100$ °C with the exception of run CZ6 ($P = 1$ GPa, $T = 1000$ °C), where only nickel was observed, and in run CZ4 ($P = 2.1$ GPa, $T = 1100$ °C), where neither nickel nor nickel oxide were observed. In experimental runs at $T = 1200$ °C (CZ18, CZ19, CZ21) nickel and nickel hydroxide were not identified.

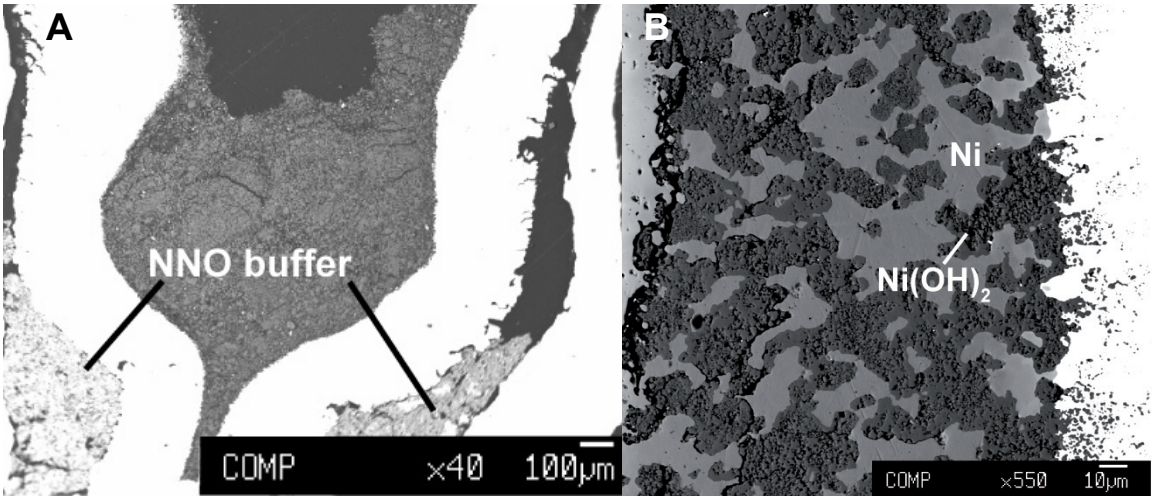


Fig. 3.7. A) BSE image of experimental run CZ7 ($P$ = 1 GPa, $T$ = 900 °C). The oxygen buffer is located between the inner and the outer capsule; B) BSE image of the oxygen buffer NNO in experimental run CZ3 ($P$ = 1 GPa, $T$ = 800 °C).

Diamond trap (Fig. 3.8) was identified at the center of the capsule in all the experimental runs at $T$ < 1100 °C. Runs at higher temperatures conditions ($T$ > 1100 °C: CZ18, CZ19, CZ21 and CZ4) do not show a preserved diamond trap. In experimental runs CZ18 and CZ19 the diamonds are scattered in the capsule (Fig. 3.9). In experimental run CZ4 only few diamonds have been identified in the entire capsule (Fig. 3.10). At higher temperature conditions in experiment CZ21 at $T$ = 1200 °C, diamonds were not found at all in the sample.

Graphite has been observed in all the samples with the exception of the experimental run CZ21, at higher pressure and temperature conditions.

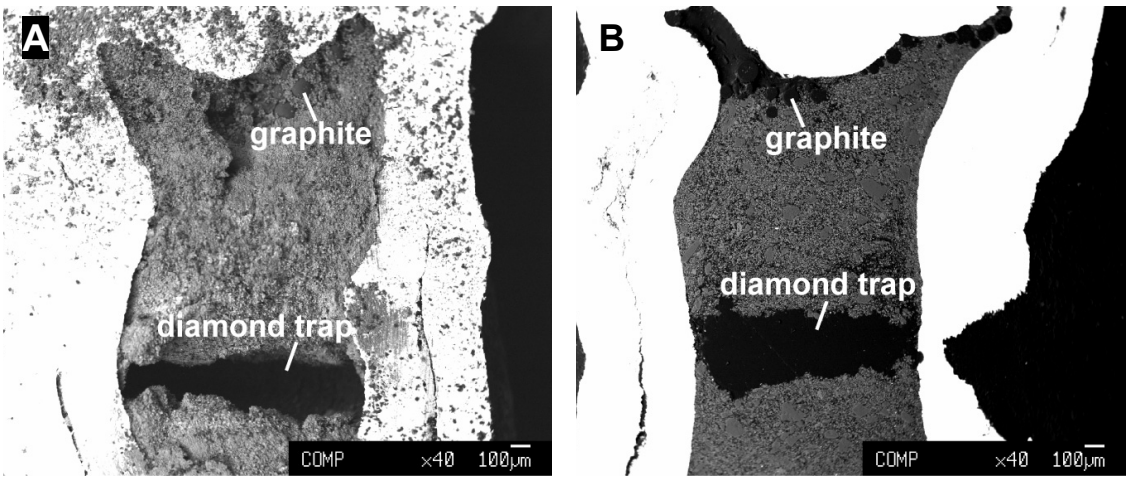


Fig. 3.8. BSE images of diamond traps A) unpolished run CZ7 ($P$ = 1 GPa, $T$ = 900 °C); B) polished run CZ11 ($P$ = 1 GPa, $T$ = 700 °C).

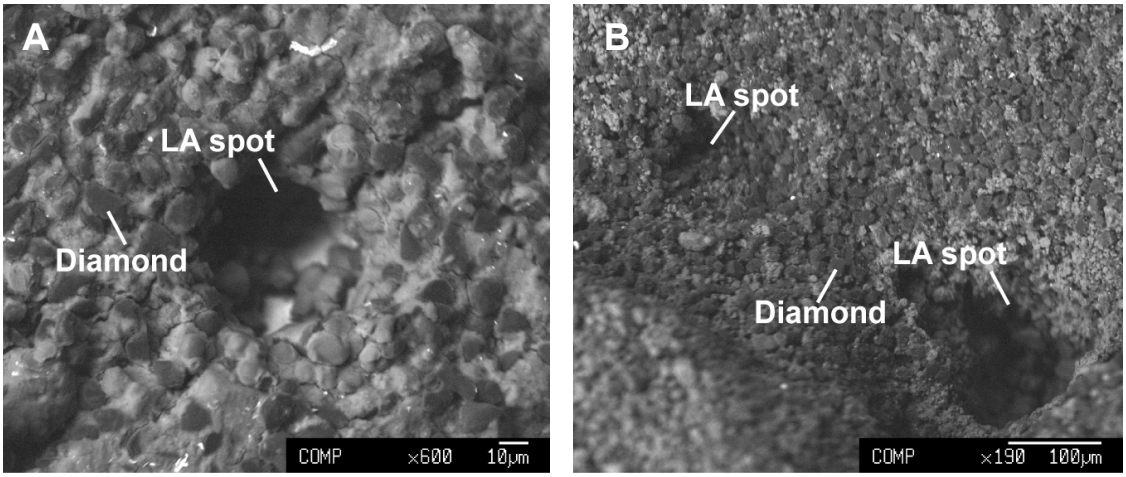


Fig. 3.9. BSE images of the diamonds spread into the solid residue of two experimental runs A) run CZ18 ($P$ = 1 GPa, $T$ = 1200 °C); B) run CZ19 ($P$ = 1.5 GPa, $T$ = 1200 °C).

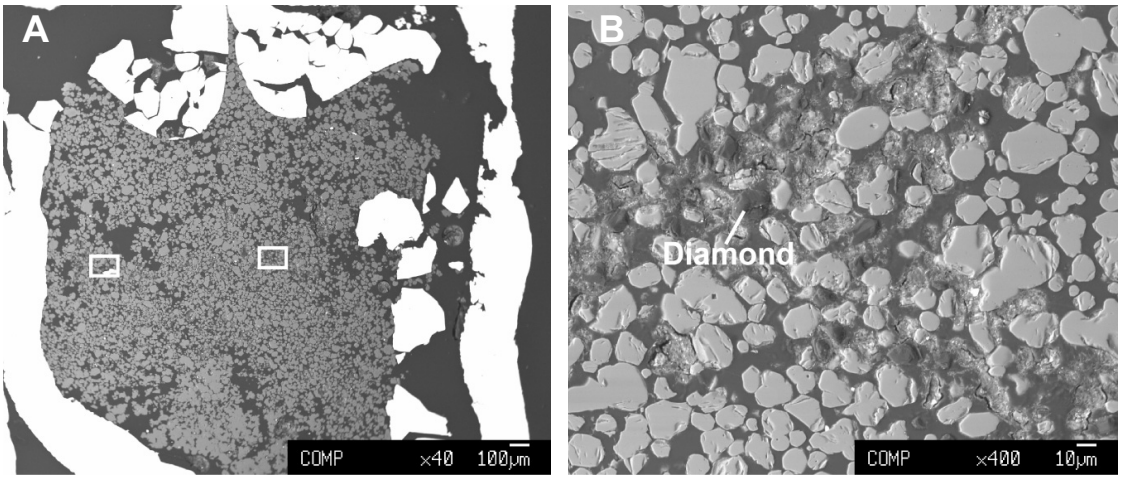


Fig. 3.10. A) BSE image of experimental run CZ4 ($P$ = 2.1 GPa, $T$ = 1100 °C), white squares indicate the areas in which diamonds have been observed; B) detail of experimental run CZ4 where diamonds have been identified.

# 3.3. Results

## 3.3.1. Run table

Experimental conditions for each run are reported in Table 3.1 along with the observed mineral assemblage. All experimental runs were performed at fluid saturated conditions, with a graphite-saturated COH fluid (GCOH fluid in Table 3.1) in double capsules. In Figure 3.11 we display the run products, some modeled reference reactions and the experimental carbonation curve of forsterite (reaction 3.2) that we determined on the basis of textural observations.

We also performed two experiments in presence of a $H_2O$-only fluid in single capsule at $P$ = 1 GPa and $T$ = 800–900 °C using the starting material FoEn, to compared the experimental results in the system MS + $H_2O$ with the results in the system MS + COH fluid.

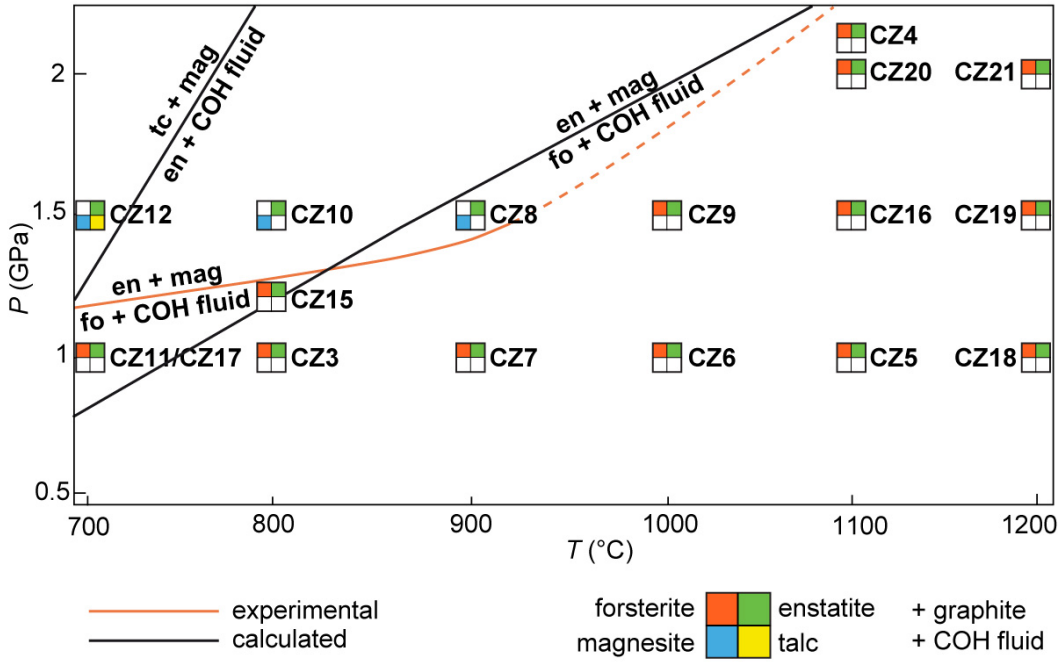


Fig. 3.11. Phase assemblages found in the MS + COH system buffered at $fH_2^{NNO}$ conditions as a function of $P$ and $T$. Run numbers are reported near the phase assemblage. Reactions reported in black solid lines are reported for reference and were calculated by means of thermodynamic modeling. Solid orange line represents the reaction fo + COH fluid = en + mag drawn on the basis of the mineral assemblages observed in textural equilibrium.

Electron-microprobe analyses and electron-microscopy observations will be presented in the next section where runs will be described on the basis of the observed mineral assemblage. At the $P$–$T$–$fO_2$ conditions investigated, from low to high pressure, we observed first forsterite + enstatite (fo + en) assemblage, then enstatite + magnesite (en + mag) and finally talc + magnesite (tc + mag) assemblage.

In Section 3.3.3 the measured contents of $SiO_2$ and MgO in $H_2O$ (for single capsule experiments) and in the aqueous fraction of the COH fluid (for double capsule experiments) retrieved through the cryogenic LA-ICP-MS technique will be presented.

| Run | $P$ (GPa) | $T$ (°C) | Starting material | Fluid | Run time (h) | Run products | $X$(O) | log$f$O$_2$ | $X$CO$_2$ |
|---|---|---|---|---|---|---|---|---|---|
| CZ11 | 1 | 700 | EnMag | GCOH | 48 | fo + en | 0.58 | -16.35 | 0.47 |
| CZ17 | 1 | 700 | FoEn | GCOH | 46 | fo + en | 0.58 | -16.35 | 0.47 |
| CZ24 | 1 | 700 | FoEn | $H_2O$ | 23 | fo + en | - | - | - |
| CZ3 | 1 | 800 | FoEn | GCOH | 48 | fo + en | 0.68 | -14.37 | 0.62 |
| CZ22 | 1 | 800 | FoEn | $H_2O$ | 43 | fo + en | - | - | - |
| CZ7 | 1 | 900 | FoEn | GCOH | 48 | fo + en | 0.75 | -12.76 | 0.71 |
| CZ6 | 1 | 1000 | FoEn | GCOH | 48 | fo + en | 0.80 | -11.42 | 0.77 |
| CZ5 | 1 | 1100 | FoEn | GCOH | 40 | fo + en | 0.84 | -10.30 | 0.82 |
| CZ18 | 1 | 1200 | FoEn | GCOH | 67 | fo + en | 0.87 | -9.34 | 0.85 |
| CZ15 | 1.2 | 800 | EnMag | GCOH | 48 | fo + en | 0.63 | -14.11 | 0.54 |
| CZ12 | 1.5 | 700 | EnMag | GCOH | 48 | tc + mag | 0.45 | -15.77 | 0.24 |
| CZ10 | 1.5 | 800 | EnMag | GCOH | 48 | en + mag | 0.55 | -13.75 | 0.43 |
| CZ8 | 1.5 | 900 | FoEn | GCOH | 120 | en + mag | 0.64 | -12.14 | 0.56 |
| CZ9 | 1.5 | 1000 | FoEn | GCOH | 72 | fo + en | 0.70 | -10.81 | 0.65 |
| CZ16 | 1.5 | 1100 | FoEn | GCOH | 44 | fo + en | 0.76 | -9.69 | 0.72 |
| CZ19 | 1.5 | 1200 | FoEn | GCOH | 24 | fo + en | 0.80 | -8.74 | 0.77 |
| CZ20 | 2 | 1100 | FoEn | GCOH | 26 | fo + en | 0.67 | -9.17 | 0.60 |
| CZ21 | 2 | 1200 | FoEn | GCOH | 24 | en | 0.72 | -8.23 | 0.67 |
| CZ4 | 2.1 | 1100 | FoEn | GCOH | 72 | fo + en | 0.65 | -9.08 | 0.58 |

Table 3.1. Run table. fo, forsterite; en, enstatite; tc; talc; mag, magnesite. $X$(O), $f$O$_2$ and $X$CO$_2$ have been estimated by thermodynamic modeling of a pure GCOH fluid buffered at $f$H$_2^{NNO}$ conditions.

### 3.3.2. Electron microscopy and microprobe characterization

#### a) Forsterite + enstatite assemblage

Experimental runs performed employing the starting material FoEn, in presence of a $H_2O$-only fluid and a COH fluid, present a forsterite + enstatite assemblage at pressure of 1 GPa and temperatures from 700 to 1200 °C. At higher pressures, fo + en is also present at $P$ = 1.2 GPa and $T$ = 800 °C, at $P$ = 1.5 GPa and $T$ = 1000–1200 °C, at $P$ = 2 GPa and $T$ =1100–1200 °C and at $P$ = 2.1 GPa and $T$ = 1100 °C (Fig. 3.11; Table 3.1). Often, runs present a microtexture characterized by relatively fine-grained areas, characterized by grain size less than 5 μm, and more coarse-grained parts, with grain size up to 40 μm (Fig. 3.12). Runs CZ17, CZ18, CZ19 and CZ4 present a homogeneous texture (Fig. 3.13).

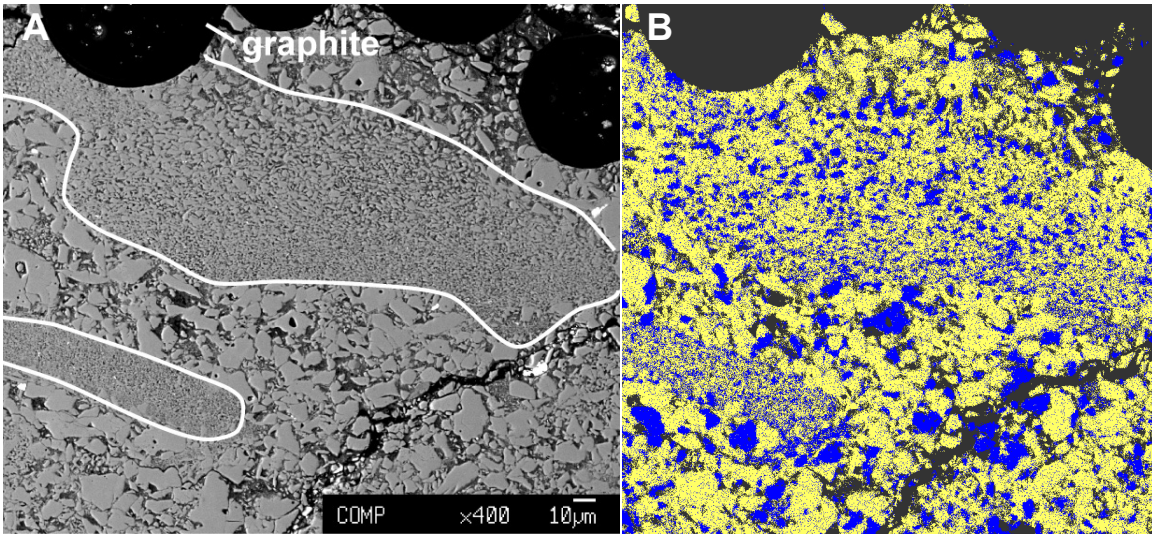


Fig. 3.12. A) BSE image of the fine-grained area and coarse-grained zone in experimental run CZ3 ($P$ = 1 GPa, $T$ = 800 °C). White lines highlight the finer-grained areas of the capsule. B) Principal component analysis performed on the same area in order to distinguish the different phases. Forsterite is displayed in yellow and enstatite in blue.

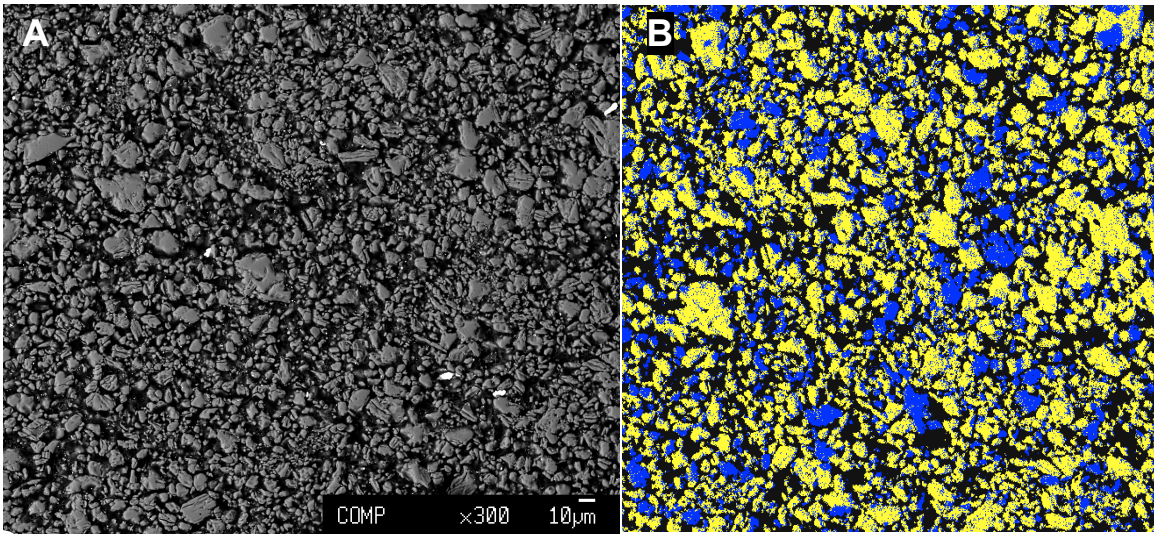


Fig. 3.13. A) BSE image of the homogeneous texture in experimental run CZ17 ($P$ = 1 GPa, $T$ = 700 °C). B) Principal component analysis performed on the same area. Forsterite is displayed in yellow and enstatite in blue.

In experimental run CZ21 ($P$ = 2 GPa, $T$ = 1200 °C), the characterization of phases was particularly difficult as the capsule was severely damaged during the cutting procedure for LA analysis (Fig. 3.14A). Run products present a sponge-like texture constitutes by mainly by $SiO_2$ with small enstatite crystals. No forsterite crystals were observed (Fig. 3.14B).

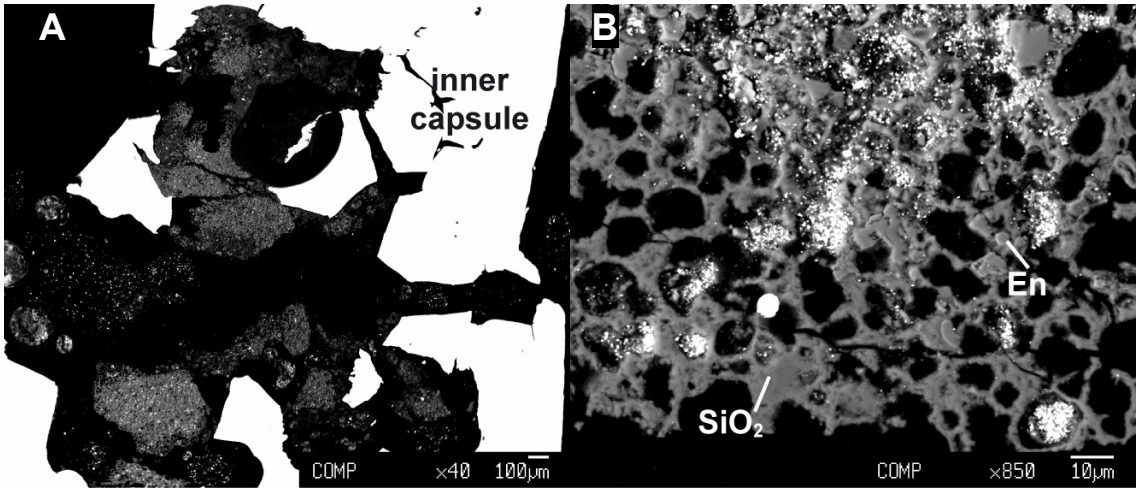


Fig. 3.14. A) BSE image of experimental run CZ21 ($P$ = 2 GPa, $T$ = 1200 °C). B) Detail of the texture of run CZ21, characterized by the presence of $SiO_2$ and small enstatite crystals.

In two runs performed employing as starting material EnMag (CZ11 and CZ15) we observed the equilibrium assemblage forsterite + enstatite. However, magnesite relics from the starting material are also present in these runs, displaying forsterite coronas (Fig. 3.15 and 3.16).

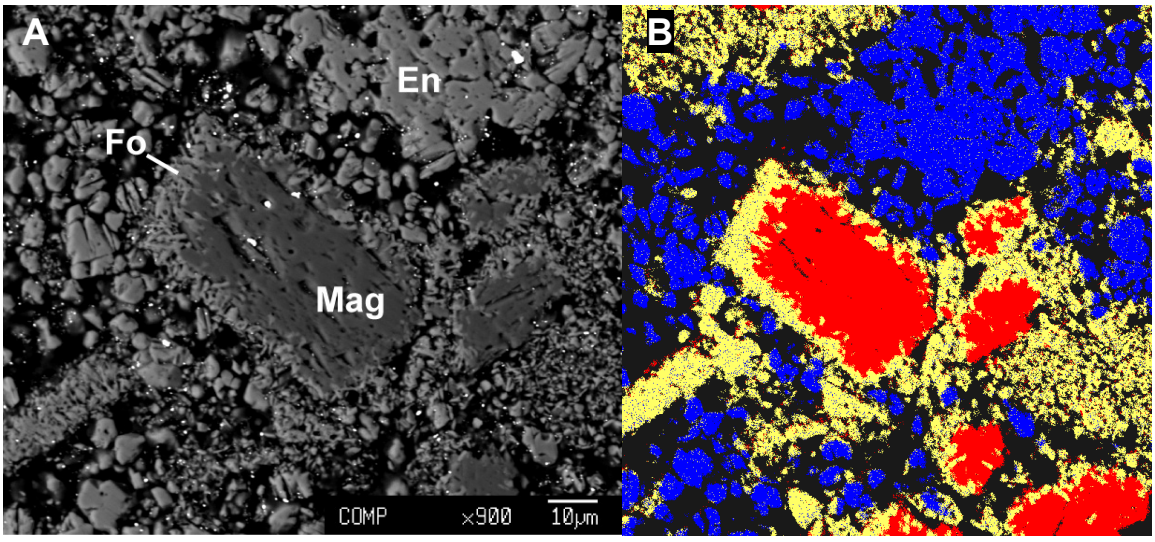


Fig. 3.15. A) BSE image of forsterite coronas on magnesite in experimental run CZ11 ($P$ = 1 GPa, $T$ = 700 °C). B) Principal component analysis performed on the same area. Forsterite is displayed in yellow, enstatite in blue and magnesite in red.

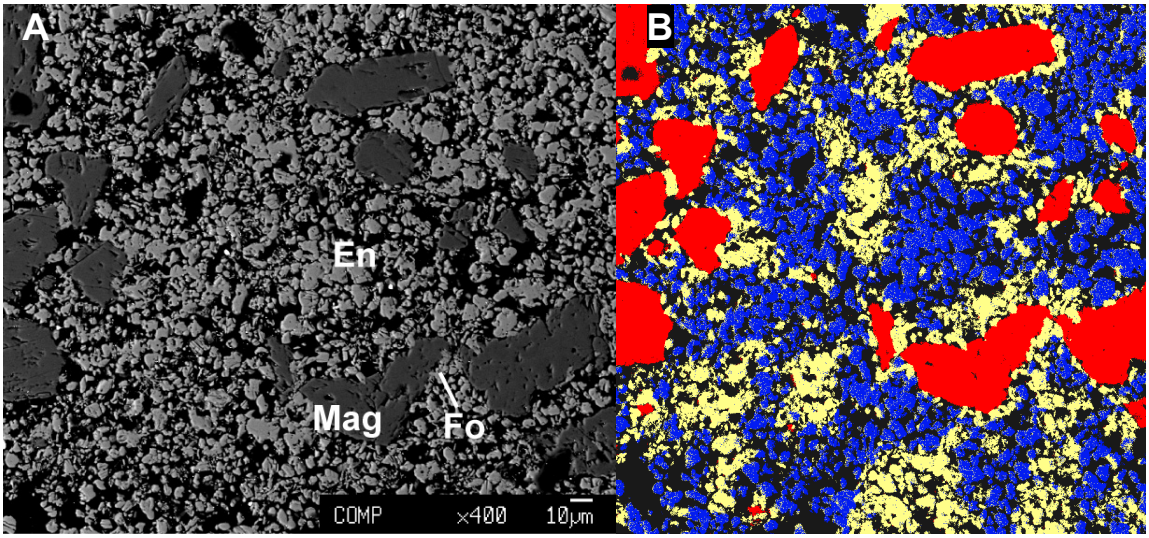


Fig. 3.16. A) BSE image of experimental run CZ15 (*P* = 1.2 GPa, *T* = 800 °C). B) Principal component analysis performed on the same area. Forsterite is displayed in yellow, enstatite in blue and magnesite in red.

Principal component analysis on X-ray elemental maps (see Section 3.2.3) was performed to evaluate the relative abundances of forsterite, enstatite and magnesite, which are given in Tables 3.2 and 3.3. Compared to the abundances of phases in the starting material, experimental runs performed using FoEn as starting material present a decrease in the Fo/(Fo + En) weight ratio (Table 3.2), which is maximum for experiment CZ9. On the other hand, experiments starting from EnMag present an increase in the Fo/(Fo + En) weight ratio (Table 3.3) compared to the starting material ratio, indicating that forsterite is growing at the expenses of magnesite, according to reaction 3.2.

No significant differences in mineral abundances were identified between the experiments performed with a $H_2O$-only fluid (CZ24 and CZ22) and the experiments performed at the same *P*–*T* conditions in presence of a GCOH fluid (CZ3 and CZ7).

We also evaluated the homogeneity of the experimental runs characterized by fine- and coarse-grained areas. Principal component analysis performed on the two parts suggests that mineral abundances is homogeneous and not dependent on the grain size.

WDS analyses of forsterite and enstatite are reported in Table 3.4 and Table 3.5 respectively. As the investigated system is virtually Fe-free, the compositions of phases do not exhibit significant variation with pressure and temperature, with the exception of experimental run CZ18, which presents high Ni-contents in both phases (up to 3 wt.% in forsterite), probably resulting from a contamination of the oxygen buffer in the inner capsule.

The slightly higher Fe-content observed in experimental run CZ15 probably derives from the presence of natural magnesite used as starting material (see Table 3.1).

| | Forsterite | Enstatite | Fo/(Fo + En) |
|---|---|---|---|
| FoEn | 83.2 | 16.7 | 0.83 |
| CZ17 | 66.6 | 33.4 | 0.67 |
| CZ24* | 62.0 | 38.0 | 0.62 |
| CZ3 | 64.2 | 35.8 | 0.64 |
| CZ22* | 64.5 | 35.5 | 0.65 |
| CZ7 | 55.5 | 44.5 | 0.56 |
| CZ6 | 57.3 | 42.7 | 0.57 |
| CZ5 | 73.7 | 26.3 | 0.74 |
| CZ18 | 53.8 | 46.2 | 0.54 |
| CZ9 | 53.1 | 46.9 | 0.53 |
| CZ16 | 65.5 | 34.5 | 0.65 |
| CZ19 | 60.3 | 39.7 | 0.60 |
| CZ20 | 62.3 | 37.7 | 0.62 |
| CZ4 | 63.6 | 36.4 | 0.64 |

Table 3.2. Phase abundances (wt.%) in the run products estimated by principal component analysis. The phase abundances of the starting material FoEn are also reported (see Section 1.2.1). Fo/(Fo + En) expressed as weight ratio. *Experiments performed in single capsule, with a $H_2O$-only fluid.

| | Forsterite | Enstatite | Magnesite | Fo/(Fo + En) |
|---|---|---|---|---|
| EnMag | 15.3 | 39.0 | 44.2 | 0.28 |
| CZ11 | 35.3 | 41.9 | 22.8 | 0.46 |
| CZ15 | 25.4 | 47.8 | 26.8 | 0.35 |

Table 3.3. Phase abundances (wt.%) in the run products estimated by principal component analysis. The phase abundances of the starting material EnMag are also reported (see Section 1.2.1). Fo/(Fo + En) expressed as weight ratio.

| Forsterite | CZ11 | CZ17 | CZ24* | CZ3 | CZ22* | CZ7 | CZ6 | CZ5 | CZ18 | CZ15 | CZ9 | CZ16 | CZ19 | CZ20 | CZ4 |
|---|---|---|---|---|---|---|---|---|---|---|---|---|---|---|---|
| *Oxides (wt.%)* | | | | | | | | | | | | | | | |
| $SiO_2$ | 42.40 | 42.09 | 42.43 | 42.42 | 42.03 | 42.77 | 41.74 | 42.16 | 41.61 | 41.98 | 42.90 | 42.17 | 42.53 | 42.54 | 42.89 |
| MgO | 56.88 | 57.00 | 57.20 | 57.27 | 56.17 | 57.01 | 57.36 | 56.96 | 55.04 | 56.71 | 56.49 | 57.20 | 57.79 | 56.86 | 56.94 |
| FeO | 0.000 | 0.123 | 0.273 | 0.059 | 0.142 | 0.165 | 0.157 | 0.100 | 0.020 | 0.609 | 0.101 | 0.079 | 0.062 | 0.084 | 0.018 |
| NiO | 0.080 | 0.000 | 0.055 | 0.000 | 0.030 | 0.047 | 0.040 | 0.030 | 3.150 | 0.021 | 0.044 | 0.000 | 0.112 | 0.040 | 0.060 |
| CaO | 0.059 | 0.013 | 0.035 | 0.010 | 0.000 | 0.021 | 0.015 | 0.009 | 0.007 | 0.011 | 0.019 | 0.000 | 0.020 | 0.017 | 0.002 |
| Total | 99.42 | 99.23 | 99.99 | 99.76 | 98.37 | 100.0 | 99.31 | 99.26 | 99.83 | 99.33 | 99.55 | 99.45 | 100.5 | 99.54 | 99.91 |
| *a.p.f.u.* | | | | | | | | | | | | | | | |
| Si | 0.999 | 0.995 | 0.996 | 0.996 | 1.001 | 1.002 | 0.987 | 0.996 | 0.992 | 0.993 | 1.008 | 0.994 | 0.993 | 1.001 | 1.005 |
| Mg | 1.998 | 2.008 | 2.001 | 2.006 | 1.994 | 1.991 | 2.022 | 2.006 | 1.956 | 2.001 | 1.980 | 2.010 | 2.011 | 1.995 | 1.989 |
| Fe | 0.000 | 0.002 | 0.005 | 0.001 | 0.003 | 0.003 | 0.003 | 0.002 | 0.000 | 0.012 | 0.002 | 0.002 | 0.001 | 0.002 | 0.000 |
| Ni | 0.003 | 0.000 | 0.001 | 0.000 | 0.001 | 0.002 | 0.001 | 0.001 | 0.060 | 0.000 | 0.001 | 0.000 | 0.002 | 0.002 | 0.002 |
| Ca | 0.001 | 0.000 | 0.001 | 0.000 | 0.000 | 0.001 | 0.000 | 0.000 | 0.000 | 0.000 | 0.000 | 0.000 | 0.001 | 0.000 | 0.000 |
| cations | 3.002 | 3.005 | 3.004 | 3.004 | 2.999 | 2.999 | 3.013 | 3.005 | 3.008 | 3.007 | 2.992 | 3.006 | 3.007 | 2.999 | 2.996 |

Table 3.4. Representative analyses of forsterite compositions. *a.p.f.u.* calculated on the basis of 4 oxygens. *Experiments performed in single capsules, with a $H_2O$-only fluid.

| Enstatite | CZ11 | CZ17 | CZ24* | CZ3 | CZ22* | CZ7 | CZ6 | CZ5 | CZ18 | CZ15 | CZ9 | CZ16 | CZ19 | CZ20 | CZ21 | CZ4 |
|---|---|---|---|---|---|---|---|---|---|---|---|---|---|---|---|---|
| *Oxides (wt.%)* | | | | | | | | | | | | | | | | |
| $SiO_2$ | 60.32 | 60.40 | 59.83 | 59.54 | 59.62 | 60.09 | 59.94 | 60.14 | 58.65 | 59.59 | 59.88 | 59.47 | 58.37 | 59.51 | 59.41 | 59.99 |
| MgO | 39.90 | 39.99 | 39.55 | 40.91 | 39.51 | 39.71 | 39.65 | 40.13 | 39.62 | 39.65 | 39.45 | 40.04 | 41.06 | 40.38 | 40.12 | 39.67 |
| FeO | 0.000 | 0.080 | 0.086 | 0.093 | 0.042 | 0.094 | 0.086 | 0.105 | 0.064 | 0.120 | 0.064 | 0.048 | 0.072 | 0.101 | 0.084 | 0.105 |
| NiO | 0.028 | 0.057 | 0.060 | 0.000 | 0.000 | 0.067 | 0.018 | 0.039 | 0.270 | 0.003 | 0.000 | 0.000 | 0.000 | 0.146 | 0.000 | 0.001 |
| CaO | 0.013 | 0.010 | 0.008 | 0.000 | 0.026 | 0.029 | 0.023 | 0.018 | 0.070 | 0.006 | 0.108 | 0.041 | 0.051 | 0.035 | 0.094 | 0.043 |
| Total | 100.3 | 100.5 | 99.53 | 100.5 | 99.20 | 99.99 | 99.72 | 100.4 | 98.67 | 99.37 | 99.50 | 99.60 | 99.55 | 100.2 | 99.71 | 99.81 |
| *a.p.f.u.* | | | | | | | | | | | | | | | | |
| Si | 2.009 | 2.007 | 2.008 | 1.983 | 2.007 | 2.008 | 2.008 | 2.002 | 1.991 | 2.004 | 2.010 | 1.997 | 1.967 | 1.990 | 1.994 | 2.008 |
| Mg | 1.981 | 1.981 | 1.979 | 2.031 | 1.983 | 1.978 | 1.980 | 1.991 | 2.006 | 1.988 | 1.974 | 2.004 | 2.063 | 2.013 | 2.007 | 1.980 |
| Fe | 0.000 | 0.002 | 0.002 | 0.003 | 0.001 | 0.003 | 0.002 | 0.003 | 0.002 | 0.003 | 0.002 | 0.001 | 0.002 | 0.003 | 0.002 | 0.003 |
| Ni | 0.002 | 0.002 | 0.002 | 0.000 | 0.000 | 0.004 | 0.000 | 0.002 | 0.007 | 0.000 | 0.000 | 0.000 | 0.000 | 0.004 | 0.000 | 0.000 |
| Ca | 0.000 | 0.000 | 0.000 | 0.000 | 0.001 | 0.001 | 0.001 | 0.001 | 0.002 | 0.000 | 0.004 | 0.001 | 0.002 | 0.001 | 0.003 | 0.002 |
| cations | 3.992 | 3.993 | 3.992 | 4.017 | 3.993 | 3.994 | 3.992 | 3.999 | 4.009 | 3.996 | 3.990 | 4.003 | 4.033 | 4.010 | 4.006 | 3.992 |

Table 3.5. Representative analyses of enstatite compositions. *a.p.f.u.* calculated on the basis of 6 oxygens. *Experiments performed in single capsules, with a $H_2O$-only fluid.

### Phases not in textural equilibrium

In Table 3.6 we reported the compositions of the magnesite relics from experiments CZ11 and CZ15. Magnesites in both runs seem to be depleted in Fe compared to the starting material (see Table 1.2). Experimental run CZ20 performed starting from FoEn also presents magnesite crystals, located in the proximity of graphite spheres. The presence of magnesite in the capsule is very localized, as verified through X-ray maps of elements and principal component analysis, so this phase do not appear to be an equilibrium phase. WDS analysis of magnesite in experimental run CZ20 is also reported in Table 3.6 and presents higher FeO and NiO content compared to the magnesite relics from experiments CZ11 and CZ15.

| Magnesite | CZ11 | CZ15 | CZ20 |
|---|---|---|---|
| *Oxides (wt.%)* | | | |
| $SiO_2$ | 0.018 | 0.034 | 2.020 |
| MgO | 46.89 | 48.73 | 46.50 |
| FeO | 0.000 | 0.000 | 0.067 |
| NiO | 0.000 | 0.000 | 0.559 |
| CaO | 0.000 | 0.113 | 0.067 |
| $CO_2$ | 51.21 | 53.31 | 52.67 |
| Total | 98.11 | 102.2 | 101.9 |
| *a.p.f.u.* | | | |
| Si | 0.003 | 0.005 | 0.024 |
| Mg | 0.997 | 0.998 | 0.965 |
| Fe | 0.000 | 0.000 | 0.001 |
| Ni | 0.000 | 0.000 | 0.010 |
| Ca | 0.000 | 0.002 | 0.001 |
| C | 1.000 | 1.000 | 1.000 |
| cations | 2.000 | 2.005 | 2.000 |

Table 3.6. Representative compositions of magnesite not in textural equilibrium. *a.p.f.u.* calculated on the basis of 1 equivalent oxygen. $CO_2$ is calculated by stoichiometry.

In experimental runs CZ7 and CZ4 we observed $MgCO_3$ (Fig. 3.17). In the experimental run at higher pressure and temperatures conditions (CZ4) the precipitates present an acicular shape (Fig. 3.16B). WDS analyses of $MgCO_3$ are reported in Table 3.7. Experimental runs CZ19 and CZ4 contain $SiO_2$-rich microspheres (Fig. 3.18A), which were not retrieved in the polished section. At higher-pressure conditions (run CZ21), $SiO_2$ microspheres are widespread in the entire capsule, forming a sponge-like texture (Fig.

3.18B). WDS analyses of $SiO_2$ are reported in Table 3.7. Unlike in forsterite, enstatite and magnesite, where Cs is below detection limit, magnesite and $SiO_2$ microsphere do contain small amounts of Cs (Table 3.7).

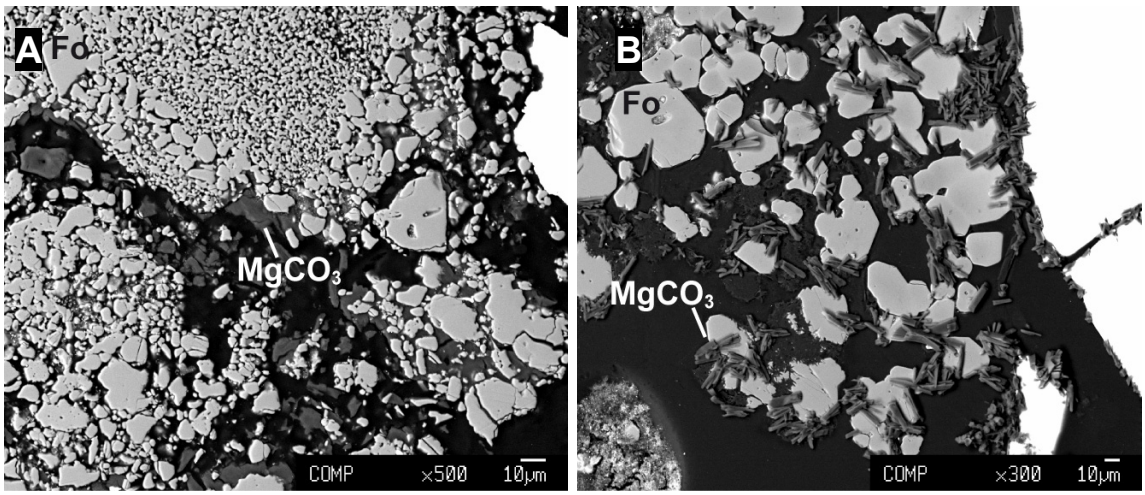


Fig. 3.17. BSE images of $MgCO_3$: A) experimental run CZ7 ($P$ = 1 GPa, $T$ = 900 °C). B) Acicular shape of $MgCO_3$ in experimental run CZ4 ($P$ = 2.1 GPa, $T$ = 1100 °C).

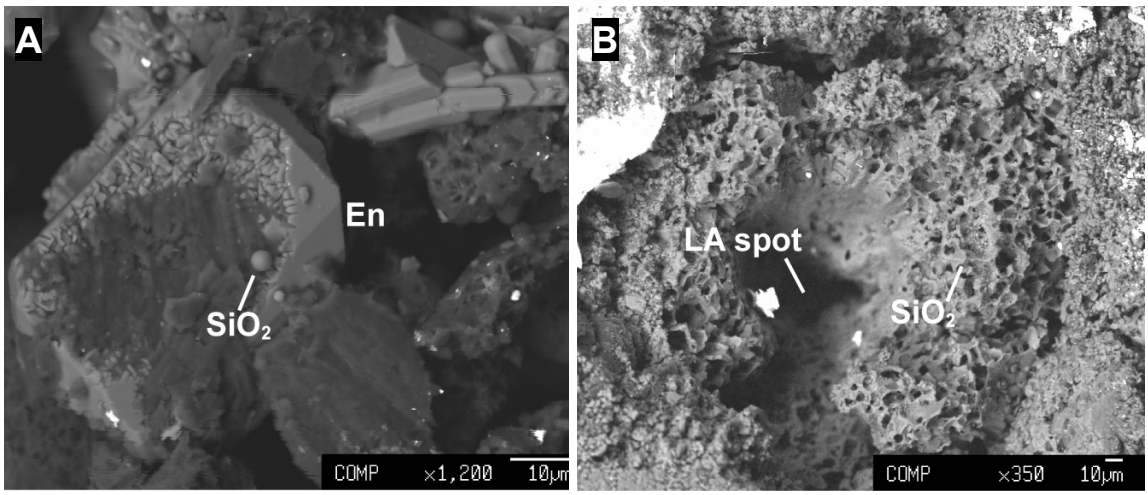


Fig. 3.18. BSE images of $SiO_2$: A) $SiO_2$ microsphere in unpolished section of experimental run CZ4 ($P$ = 2.1 GPa, $T$ = 1100 °C). B) Widespread $SiO_2$ in the unpolished section of experimental run CZ21 ($P$ = 2 GPa, $T$ = 1200 °C).

| | $MgCO_3$ | | $SiO_2$ |
|---|---|---|---|
| | CZ7 | CZ4 | CZ21 |
| *Oxides (wt.%)* | | | |
| $SiO_2$ | 0.141 | 0.131 | 61.79 |
| MgO | 31.23 | 33.64 | 0.29 |
| FeO | 0.008 | 0.042 | 0.000 |
| NiO | 0.000 | 0.113 | 0.108 |
| CaO | 0.047 | 0.047 | 0.018 |
| $Cs_2O$ | 0.012 | 0.068 | 0.041 |
| Total | 31.44 | 34.04 | 62.24 |

Table 3.7. Representative $MgCO_3$ and $SiO_2$ microspheres analyses.

## b) Enstatite + magnesite assemblage

Experimental runs at $P$ = 1.5 GPa and $T$ = 800–900 °C, present the assemblage enstatite + magnesite. The two experiments were performed employing different starting materials: EnMag at $T$ = 800 °C, and FoEn at $T$ = 900 °C.

In experimental run CZ10 forsterite is no longer present and the En/(En + Mag) weight ratio with respect to the starting material is higher (Table 3.8).

Principal component analysis performed on experimental run CZ10 presents an increase in the enstatite content at the expenses of forsterite, which is no longer present in the charge (Fig. 3.19). Experimental run CZ8, performed employing FoEn as starting material presents magnesite formation in the proximity of forsterite crystals (Fig. 3.20). From principal component analysis we estimated the formation of ~20 wt.% of magnesite. WDS analyses are reported in Table 3.9. Magnesite in run CZ10 presents similar Fe content compared to the magnesite employed as starting material (see Table 1.2).

| | Forsterite | Enstatite | Magnesite | En/(En + Mag) |
|---|---|---|---|---|
| EnMag | 15.3 | 39.0 | 44.2 | 0.47 |
| FoEn | 83.2 | 16.7 | 0.00 | 1.00 |
| CZ10 | 0.00 | 55.3 | 44.7 | 0.55 |
| CZ8 | 33.9 | 47.4 | 18.7 | 0.72 |

Table 3.8. Phase abundances (wt.%) in the run products estimated by principal component analysis. The phase abundances of the starting material EnMag are also reported (see Section 1.2.1). En/(En + Mag) expressed as weight ratio.

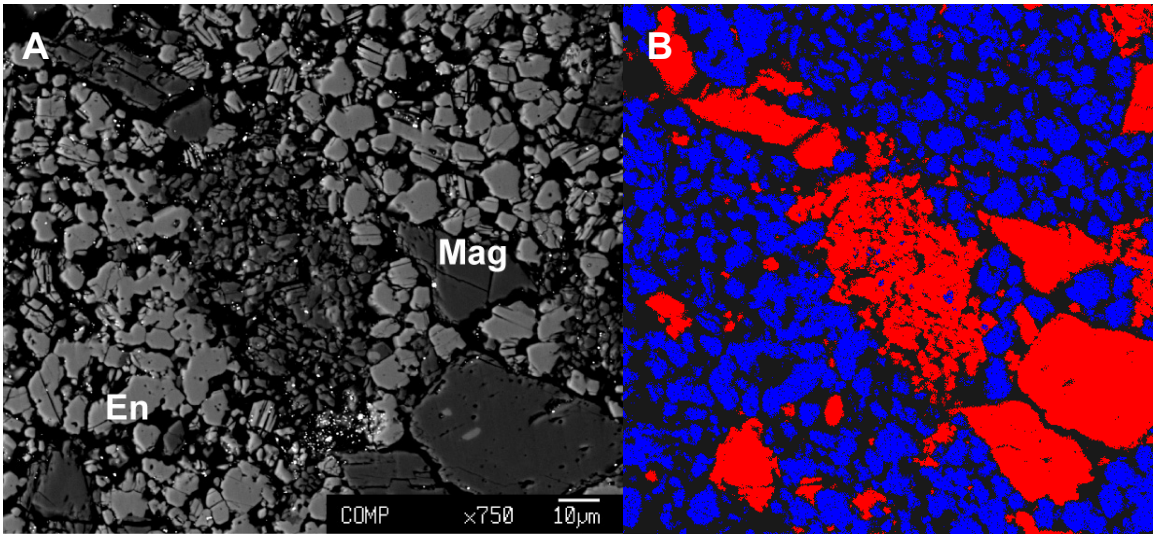


Fig. 3.19. A) BSE image of the enstatite + magnesite assemblage in run CZ10 (*P* = 1.5 GPa, *T* = 800 °C). B) Principal component analysis performed on the same area. Enstatite is displayed in blue and magnesite in red.

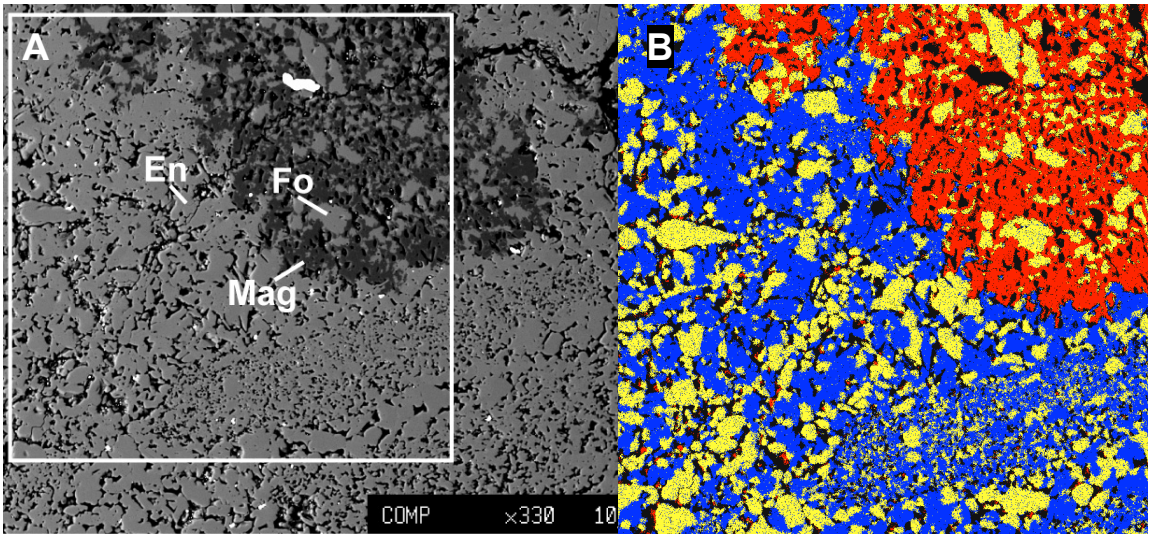


Fig. 3.20. A) BSE image of run CZ8 (*P* = 1.5 GPa, *T* = 900 °C). The squared area has been analyzed through principal component analysis. B) PCA, forsterite is displayed in yellow, enstatite in blue and magnesite in red.

| | Magnesite | | Enstatite | | Forsterite |
|---|---|---|---|---|---|
| | CZ10 | CZ8 | CZ10 | CZ8 | CZ8 |
| *Oxides (wt.%)* | | | | | |
| $SiO_2$ | 0.002 | 0.172 | 60.17 | 58.10 | 42.37 |
| MgO | 47.31 | 45.90 | 39.50 | 41.31 | 56.73 |
| FeO | 0.531 | 0.000 | 0.058 | 0.000 | 0.000 |
| NiO | 0.000 | 0.014 | 0.000 | 0.021 | 0.033 |
| CaO | 0.033 | 0.025 | 0.016 | 0.019 | 0.009 |
| $CO_2$ | 52.00 | 50.27 | - | - | - |
| Total | 99.88 | 96.38 | 99.74 | 99.46 | 99.14 |
| *a.p.f.u.* | | | | | |
| Si | 0.000 | 0.003 | 2.014 | 1.960 | 1.001 |
| Mg | 0.993 | 0.997 | 1.971 | 2.078 | 1.998 |
| Fe | 0.006 | 0.000 | 0.002 | 0.000 | 0.000 |
| Ni | 0.000 | 0.000 | 0.000 | 0.001 | 0.001 |
| Ca | 0.001 | 0.004 | 0.001 | 0.001 | 0.000 |
| C | 1.000 | 1.000 | - | - | - |
| cations | 2.000 | 2.004 | 3.986 | 4.040 | 3.000 |

Table 3.9. Representative enstatite, magnesite and forsterite compositions. *a.p.f.u.* calculated on the basis of 6 oxygens for enstatite, of 1 equivalent oxygen for magnesite and of 4 oxygens for forsterite (which is not in textural equilibrium). $CO_2$ in magnesite is calculated by stoichiometry.

## c) Talc + magnesite assemblage

At $P$ = 1.5 GPa and $T$ = 700 °C the assemblage talc + magnesite is stable. Enstatite is still presents in the experimental charge, unlike forsterite (Fig. 3.21). Principal component analysis performed on X-ray maps of elements present decreasing values of both enstatite and magnesite, and growth of talc (Table 3.10). Representative mineral compositions are reported in Table 3.11.

| | Forsterite | Enstatite | Magnesite | Talc | En/(En+Mag) |
|---|---|---|---|---|---|
| EnMag | 15.3 | 39.0 | 44.2 | 0.00 | 0.47 |
| CZ12 | 0.00 | 25.1 | 37.9 | 37.0 | 0.40 |

Table 3.10. Phase abundances (wt.%) in the run products estimated by principal component analysis. The phase abundances of the starting material EnMag are also reported (see Section 1.2.1). En/(En+Mag) expressed as weight ratio.

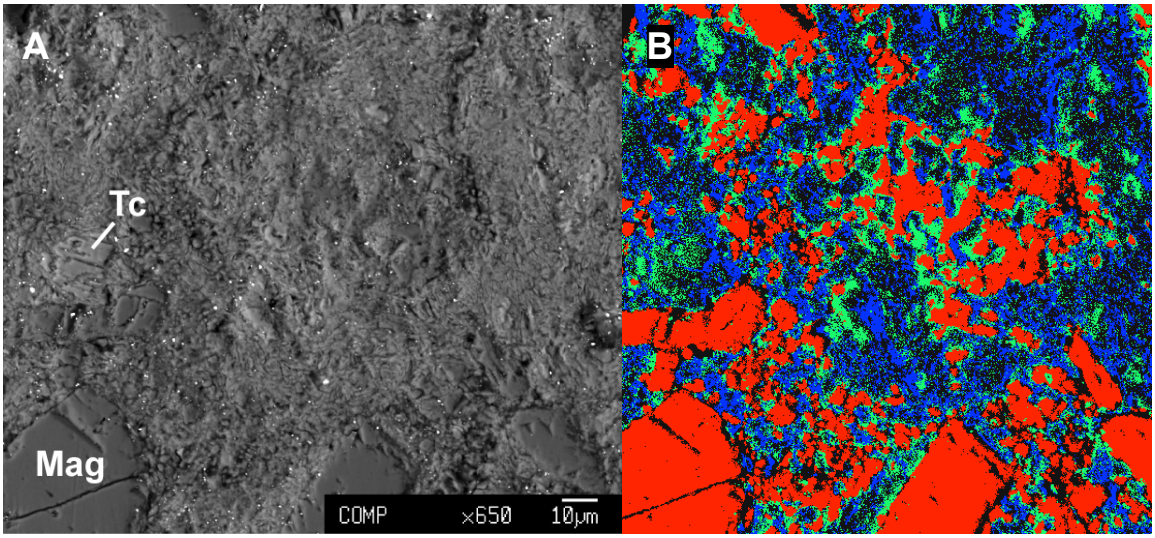


Fig. 3.21. A) BSE image of talc + magnesite assemblage in run CZ12 (*P* = 1.5 GPa, *T* = 700 °C). B) Principal component analysis performed on the same area. Enstatite is displayed in blue, magnesite in red and talc in green.

| | Magnesite | Talc | Enstatite |
|---|---|---|---|
| *Oxides (wt.%)* | | | |
| $SiO_2$ | 0.011 | 62.05 | 59.74 |
| MgO | 46.84 | 31.99 | 39.78 |
| FeO | 0.339 | 0.102 | 0.068 |
| NiO | 0.038 | 0.021 | 0.000 |
| CaO | 1.026 | 0.032 | 0.014 |
| $CO_2$ | 52.18 | - | - |
| H2O | - | 4.690 | - |
| Total | 100.4 | 98.89 | 99.60 |
| *a.p.f.u.* | | | |
| Si | 0.000 | 3.970 | 2.004 |
| Mg | 0.980 | 3.051 | 1.989 |
| Fe | 0.004 | 0.005 | 0.002 |
| Ni | 0.000 | 0.001 | 0.000 |
| Ca | 0.015 | 0.002 | 0.000 |
| C | 1.000 | - | - |
| H | - | 2.001 | - |
| cations | 2.000 | 9.031 | 3.996 |

Table 3.11. Representative magnesite, talc and enstatite compositions. *a.p.f.u.* calculated on the basis of 1 equivalent oxygen for magnesite, 12 oxygens for talc and 6 for enstatite (not in textural equilibrium). $H_2O$ and $CO_2$ are calculated by stoichiometry.

### 3.3.3. Fluid analyses at LA-ICP-MS

As reported in Section 3.2.3, the analyzed composition of the fluid retrieved with the cryogenic LA-ICP-MS technique is relative to the aqueous fraction of the GCOH fluid. Analyses on the aqueous fraction of the COH fluid will be reported according to the mineral assemblage in equilibrium with the GCOH fluid. Mineral solubilities are expressed as molalities *m* of $SiO_2$ and MgO (*m* given in mol/kg).

Concerning the analytical error, Kessel et al. (2004) determine an uncertainty on the amount of $H_2O$ in the fluid, derived from Cs analysis, ranging from 0.7 to 2.5%, which was similar (or smaller) to the standard deviation of their experimental data. In our case, for each experiment we reported the standard deviation, as our values are higher compared to the maximum uncertainty (2.5%) determined by Kessel et al. (2004). However, if only one laser-ablation shot is available we consider the maximum uncertainty given by Kessel et al. (2004).

#### a) Forsterite + enstatite assemblage

The $SiO_2$ and MgO contents in the aqueous fraction of the GCOH fluid in equilibrium with a forsterite + enstatite assemblage are reported in Table 3.12. Calculated Cs concentrations ($C_f$Cs, see Section 3.2.3 and 3.4.3) are also reported. Diamond trap has not been preserved in experiments CZ18, CZ19, CZ21 and CZ4 so that no solubility data are available for these runs.

For experiments performed in single capsules in the MS + $H_2O$ system the amount of Cs is assumed equal to the initial concentration of the solution employed ($C_i$Cs = $C_f$Cs = 585 ppm). The same concentration is assumed also for experiment CZ6, as the oxygen buffer was not observed (see Section 3.2.3).

| Run | $P$ (GPa) | $T$ (°C) | Starting material | $m$SiO$_2$ (mol/kg) | $m$MgO (mol/kg) | MgO + SiO$_2$ (wt.%) | $C_f$Cs (ppm) | $X$CO$_2$ |
|---|---|---|---|---|---|---|---|---|
| CZ11 | 1 | 700 | EnMag | 0.91 | 0.12 | 5.61 | 208.44 | 0.47 |
| CZ17 | 1 | 700 | FoEn | 0.74 (0.12) | 0.56 (0.03) | 6.30 | 618.41 | 0.47 |
| CZ24 | 1 | 700 | FoEn | 0.45 (0.03) | 0.27 (0.07) | 3.55 | 585.00 | - |
| CZ3 | 1 | 800 | FoEn | 0.49 | 0.67 | 5.37 | 868.19 | 0.62 |
| CZ22 | 1 | 800 | FoEn | 0.28 | 0.30 | 2.80 | 585.00 | - |
| CZ7 | 1 | 900 | FoEn | 1.45 (0.23) | 0.60 (0.15) | 10.0 | 1525.2 | 0.71 |
| CZ6* | 1 | 1000 | FoEn | 1.89 (0.95) | 1.79 (0.63) | 15.4 | 585.00 | 0.77 |
| CZ5 | 1 | 1100 | FoEn | 2.63 (1.17) | 4.22 (1.25) | 24.4 | 3504.4 | 0.82 |
| CZ18 | 1 | 1200 | FoEn | n.d. | n.d. | n.d. | 4008.2 | 0.85 |
| CZ15 | 1.2 | 800 | EnMag | 0.53 (0.09) | 0.56 (0.06) | 6.24 | 326.10 | 0.54 |
| CZ9 | 1.5 | 1000 | FoEn | 2.30 | 3.47 | 21.8 | 1288.5 | 0.65 |
| CZ16 | 1.5 | 1100 | FoEn | 2.94 (0.57) | 1.99 (0.45) | 20.3 | 2130.4 | 0.72 |
| CZ19 | 1.5 | 1200 | FoEn | n.d. | n.d. | n.d. | 1601.1 | 0.77 |
| CZ20 | 2 | 1100 | FoEn | 4.02 (0.97) | 5.01 (1.77) | 30.3 | 1356.5 | 0.60 |
| CZ21 | 2 | 1200 | FoEn | n.d. | n.d. | n.d. | 1289.7 | 0.67 |
| CZ4 | 2.1 | 1100 | FoEn | n.d. | n.d. | n.d. | 863.06 | 0.58 |

Table 3.12. GCOH fluid analyses in equilibrium with forsterite + enstatite assemblage. Analyses refer to the aqueous part of the fluid. Number in parenthesis indicates absolute one standard deviation (1$\sigma$) of the average of analysis. Missing value in parenthesis indicate one shot in the diamond trap. $X$CO$_2$ has been estimated by thermodynamic modeling of a pure GCOH fluid at $f$H$_2^{NNO}$. $C_f$Cs corresponds to the cesium concentration in the capsule after fluid equilibration at $f$H$_2^{NNO}$. *experiment in which the presence of the oxygen buffer was not verified and is assumed $C_f$Cs = $C_i$Cs. n.d. = not determined.

In Figure 3.22, we reported $m$SiO$_2$ and $m$MgO in the H$_2$O-only fluid with forsterite + enstatite (experiments CZ24 and CZ22). $m$SiO$_2$ decreases with increasing temperature from 0.45 mol/kg to 0.28 mol/kg at 800 °C, while $m$MgO slightly increases from 0.27 mol/kg to 0.30 mol/kg at 800 °C.

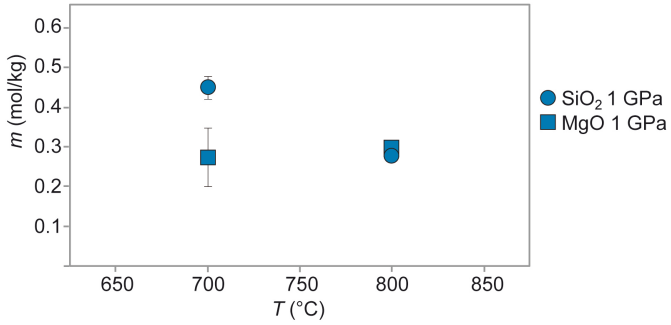


Fig. 3.22. Molalities of SiO$_2$ and MgO *vs.* temperature for the experiments performed in the MS + H$_2$O system (run CZ24 and CZ22). Errors are not shown where smaller than symbol size.

The amount of $SiO_2$ in the aqueous fraction of the COH fluid in the forsterite + enstatite assemblage presents an increase with temperature and pressure, from values of 0.49 mol/kg at $P$ = 1 GPa and $T$ = 800 °C to 4.01 mol/kg at $T$ = 1100 °C and $P$ = 2 GPa (Fig. 3.23A). At $P$ = 1 GPa and $T$ = 700 °C, fluid presents higher content in $SiO_2$ compared to the experiment at the same pressure at $T$ = 800 °C.

MgO also presents increasing values with pressure and temperature, with an exception at $P$ = 1.5 GPa where *m*MgO decreases from 3.47 mol/kg at $T$ =1000 °C to 1.99 mol/kg at $T$ = 1100 °C (Fig. 3.23B).

Solute contents from the MS + $H_2O$ system are in general lower compared to the MS + COH system with the exception of the MgO content in experimental run CZ11 at $P$ = 1 GPa and $T$ = 700 °C.

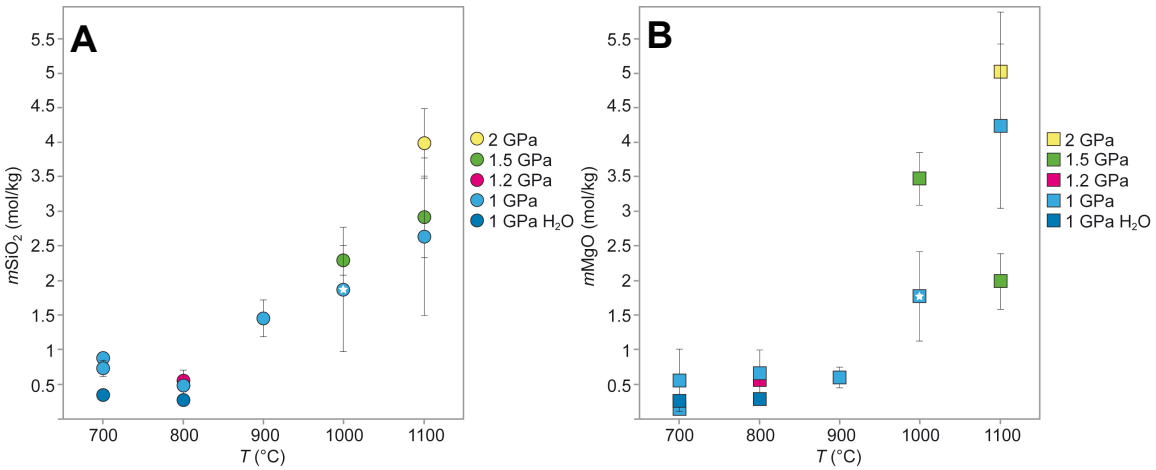


Fig. 3.23. Solute contents of $SiO_2$ (A) and MgO (B) in the aqueous fraction of the COH fluid *vs.* temperature for the forsterite + enstatite assemblage. Values relative to experimental runs performed in $H_2O$-only fluid at 700 and 800 °C are also reported for comparison. White star indicates that the solute content was retrieved without applying the Cs dilution model, as the oxygen buffer was not observed.

$SiO_2$ content in the aqueous fraction of the COH fluid presents a linear increase with increasing pressure (Fig. 3.24A). A similar behavior is observed in *m*MgO at $T$ = 800° and $T$ = 1000 °C, while at higher temperatures ($T$ = 1100 °C) the aqueous fraction of the COH fluid presents decreasing values of MgO from 1 to 1.5 GPa (Fig. 3.24B).

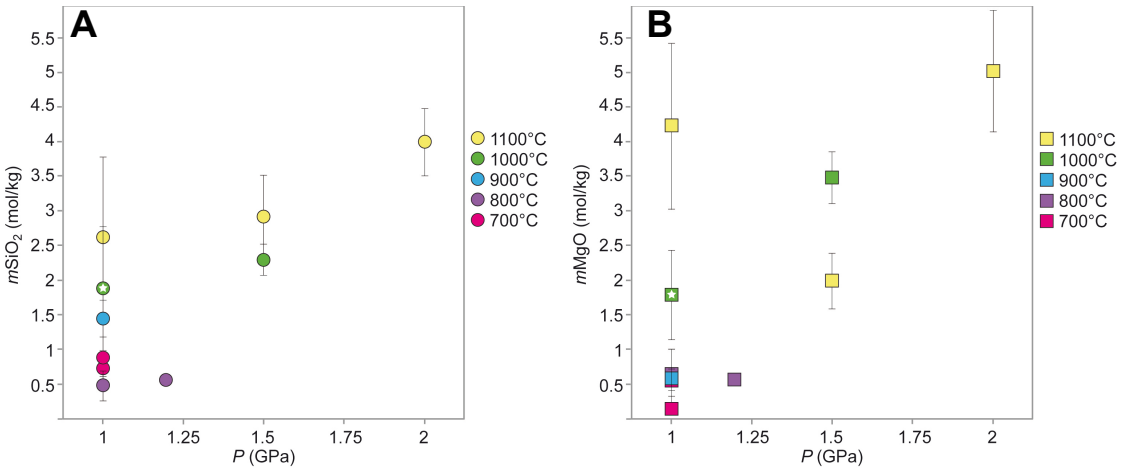


Fig. 3.24. Solute contents of $SiO_2$ (A) and MgO (B) in the aqueous fraction of the COH fluid *vs.* pressure for the forsterite + enstatite assemblage. White star indicates that the solute content was retrieved without applying the Cs dilution model, as the oxygen buffer was not observed.

## b) Enstatite + magnesite assemblage

The $SiO_2$ and MgO content in the aqueous fraction of the COH fluid in the enstatite + magnesite assemblage increase with increasing temperature (Table 3.13). As the experimental runs present magnesite we corrected the concentration of Cs, according to the amount of magnesite generated from reaction 3.2. The complete procedure will be provided in Section 3.4.3.

$m$$SiO_2$ in the $H_2O$ fraction for the enstatite + magnesite is lower compared to the solute content in the forsterite + enstatite assemblage at the same temperature but lower pressure ($P$ = 1 GPa) (Fig. 3.25A). $m$MgO presents similar values with lower pressure experiments at $P$ = 1 GPa (fo + en) at $T$ = 900°C (Fig. 3.25B).

| Run | $P$ (GPa) | $T$ (°C) | Starting material | $m$$SiO_2$ (mol/kg) | $m$MgO (mol/kg) | MgO + $SiO_2$ (wt.%) | $C_f$Cs (ppm) | $X$$CO_2$ |
|---|---|---|---|---|---|---|---|---|
| CZ10 | 1.5 | 800 | EnMag | 0.40 (0.02) | 0.35 (0.09) | 3.38 | 897.14 | 0.43 |
| CZ8 | 1.5 | 900 | FoEn | 0.63 (0.32) | 0.63 (0.24) | 5.89 | 2178.8 | 0.56 |

Table 3.13. Fluid analysis for the enstatite + magnesite assemblage. Number in parenthesis indicates absolute one standard deviation (1σ) of the average of analysis. $X$$CO_2$ has been estimated by thermodynamic modeling of a pure GCOH fluid externally at $fH_2^{NNO}$. $C_f$Cs corresponds to the cesium concentration in the capsule after fluid equilibration at at $fH_2^{NNO}$.

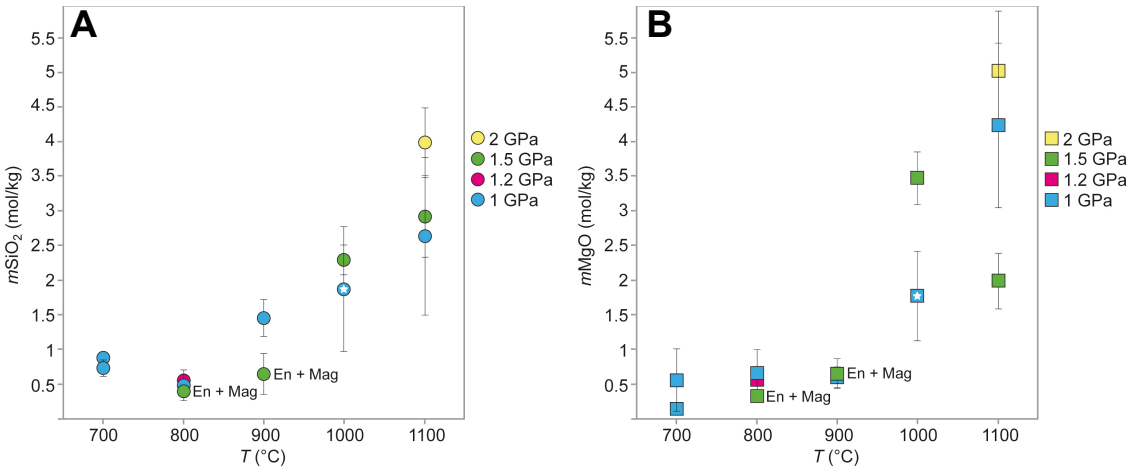


Fig. 3.25. Solute contents of $SiO_2$ (A) and MgO (B) in the aqueous fraction of the COH fluid *vs.* temperature for the enstatite + magnesite assemblage (En + Mag). Experimental data from the forsterite + enstatite assemblage are also reported for comparison. White star indicates that the solute content was retrieved without applying the Cs dilution model, as the oxygen buffer was not observed.

## c) Talc + magnesite assemblage

Contents of $SiO_2$ and MgO in the aqueous fraction of the COH fluid coexisting with the talc + magnesite assemblage are reported in Table 3.14. Also in this case a corrected Cs concentration is provided, as we observed the formation of magnesite and talc (see Section 3.4.3). $m$SiO$_2$ and $m$MgO in the aqueous fraction of the COH fluid are higher compared to experiments performed at the same $P$ (1.5 GPa) on the enstatite + magnesite assemblage (Fig 3.26).

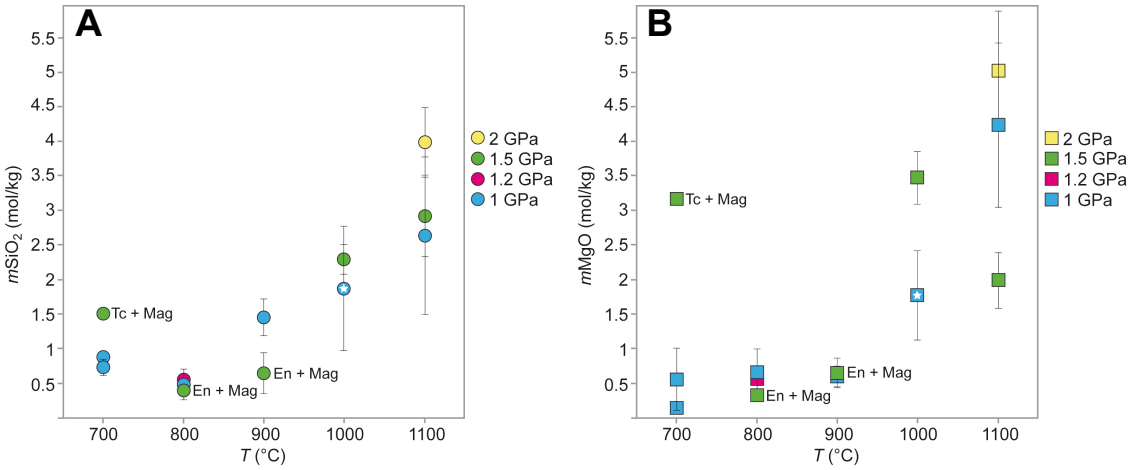


Fig. 3.26. Solute contents of $SiO_2$ (A) and MgO (B) in the aqueous fraction of the COH fluid *vs.* temperature for the talc + magnesite assemblage (Tc + Mag). Experimental data from the forsterite + enstatite and to enstatite + magnesite (En + Mag) assemblage are also reported for comparison. White star indicates that the solute content was retrieved without applying the Cs dilution model, as the oxygen buffer was not observed.

| Run | $P$ (GPa) | $T$ (°C) | Starting material | $m$SiO$_2$ (mol/kg) | $m$MgO (mol/kg) | MgO + SiO$_2$ (wt.%) | $C_f$Cs (ppm) | $X$CO$_2$ |
|---|---|---|---|---|---|---|---|---|
| CZ12 | 1.5 | 700 | EnMag | 1.52 | 3.21 | 18.1 | 20919.94 | 0.24 |

Table 3.14. Fluid analysis for the talc + magnesite assemblage. Missing value standard deviation indicate one shot in the diamond trap. $X$CO$_2$ has been estimated by thermodynamic modeling of a pure GCOH fluid at $f$H$_2^{NNO}$. $C_f$Cs corresponds to the cesium concentration in the capsule after fluid equilibration at $f$H$_2^{NNO}$.

# 3.4. Discussion

## 3.4.1. MS + $H_2O$ system

The cryogenic LA-ICP-MS has been mainly employed to analyze fluid and melts at high-pressure conditions. Kessel et al. (2004, 2005a, 2005b), which developed the technique, investigated the eclogitic system in presence of water at $P$ = 4–6 GPa and $T$ = 700–1400 °C, study extended at $P$ = 2–3 GPa and $T$ = 700–1200 °C by Luginbuehl et al. (2013). Melekhova et al. (2007) focused their attention to the MS + $H_2O$ system up to 13.5 GPa and $T$ = 1000–1350 °C, investigating liquid and melt compositions.

At subsolidus conditions, Aerts et al. (2010) tested the freezing stage also employed in this experimental work (see Section 3.2.3) by reproducing quartz solubility experiments of Manning (1994) at $P$ = 0.88 GPa and $T$ = 700 °C. The measured contents of $SiO_2$ in water agreed with experimental data retrieved using the weight loss technique (Manning, 1994) suggesting that diamond-trap experiments were comparable in accuracy and precision with weigh-loss data.

Reproducing experimental data from literature, obtained with different experimental and analytical strategies is a fundamental step to evaluate if a new experimental procedure is promising or not. Aerts et al. (2010) demonstrate that the freezing approach is a valid approach, able to provide data on quartz solubility in water.

In our study, we tested the cryogenic LA-ICP-MS technique on mantle minerals in equilibrium with water. We performed two experiments $T$ = 700 and T = 800 °C at $P$ = 1 GPa, using the forsterite + enstatite mix FoEn (see Section 1.2.1) at $T$ = 700–800 °C (runs CZ24 and CZ22).

We compared the measured $SiO_2$ content in $H_2O$ with experimental data from Newton & Manning (2002), which measured enstatite + forsterite solubility in $H_2O$ using the weigh loss method and by approaching silica solubility from higher to lower silica concentration. Newton & Manning (2002) used as minerals in equilibrium with water

forsterite (FQ) and enstatite (EQ), both as single crystals, and a mixture of fine-grained forsterite + enstatite in equal mass proportion (EFQ). Comparison with our experimental results in $H_2O$ is presented in Figure 3.27.

At $P$ = 1 GPa and $T$ = 700 °C the amount of $SiO_2$ measured in water is 0.45 mol/kg, a higher value compared to Newton & Manning (2002) ($mSiO_2$ = 0.25 mol/kg). A possible explanation for the discrepancy in the experimental results at 700 °C could be attributed to the different grain size of the starting material of the two compared experiments. Our experimental result were retrieved from a synthetic forsterite + enstatite powder (FoEn), while the experiment performed by Newton & Manning (2002) was conducted on single crystals of forsterite (1 to 3 mm length).

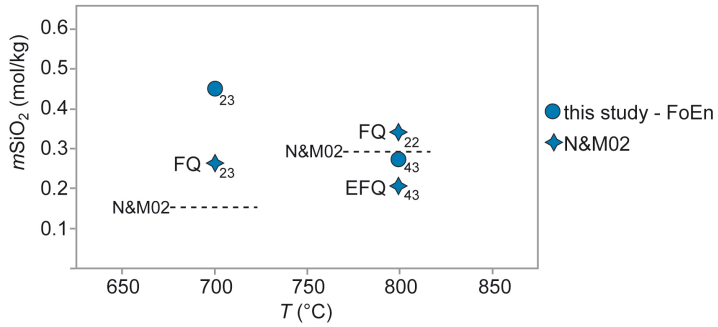


Fig. 3.27. Comparison of our experimental data on $mSiO_2$ with data from Newton & Manning (2002) (N&M02) at 1 GPa. FQ, forsterite single crystal; EFQ, forsterite + enstatite powder mixture. Run times are reported below symbols and are given in hours. Errors are not shown when smaller than symbol size. Dashed lines represent the average silica solubility retrieved by Newton & Manning (2002).

At $P$ = 1 GPa and $T$ = 800 °C, $SiO_2$ content in $H_2O$ obtained by the freezing technique ($mSiO_2$ = 0.28 mol/kg) is similar to the data of Newton & Manning (2002) on forsterite + enstatite powder mixture ($mSiO_2$ = 0.21 mol/kg, same run time). In this case, the compared experiments were both performed on synthetic powders.

It has to be noted that the solubility of enstatite and forsterite in $H_2O$ was determined by Newton & Manning (2002) by bracketing experiments from high to low $SiO_2$ concentrations. The bracketing results are reported in Figure 3.27 as dashed lines. Newton & Manning (2002) observed that the experiments approach each other closely at 700 °C for run times longer that 100 hours. The strong difference between experiment CZ24 and the calculated $mSiO_2$ of Newton & Manning (2002) at 700 °C could result also from relatively short run time (24 hours). However, the result at $T$ = 800 °C, which perfectly agrees with Newton & Manning (2002), suggests that the cryogenic LA-ICP-MS

technique can be applied to measure solutes content in fluid in equilibrium with mantle minerals (e.g., forsterite and enstatite).

### 3.4.2. MS + COH system: solid phases

Some considerations about the mineral assemblages present in our experimental runs can be done considering the Gibbs phase rule, which defines the number of phases that can occur in *n*-variant fields. Our experimental study is characterized by four components (MS + C + COH). Therefore a divariant *P–T* field should contain 4 phases, including COH fluid and graphite, always in excess. In the majority of the experimental runs we observed the presence the assemblage forsterite + enstatite + graphite + COH fluid.

In experiments CZ11 and CZ15 we identify forsterite, enstatite and magnesite (+ C + COH fluid). The two runs presented forsterite coronas on magnesite crystals (Section 3.3.2a). By means of principal component analysis, we observed an increment in the forsterite content, expressed as Fo/(Fo + En), from 0.28 of the starting material EnMag to 0.46 for run CZ11 and 0.35 for run CZ15. These characteristics suggest that the stable mineral assemblage in both experimental run is forsterite + enstatite and the presence of magnesite relics derive exclusively from the starting material EnMag.

Experimental run CZ8 performed using FoEn starting material presented newly formed magnesite crystals around forsterite. In this case the stable assemblages was enstatite + magnesite, in fact, the experimental *P–T* conditions were close to the calculated carbonation reaction 1.1 (Section 3.3.1). From principal component analysis we estimates that approximately the 50 mol% of forsterite in the charge reacted to form magnesite.

In experimental run CZ20 performed employing the starting material FoEn we also identify few magnesite crystals. However, in this case magnesite was located only around graphite spheres. In this case we suggest that magnesite could results from metastable growth around graphite crystal due to thermal gradient.

$SiO_2$ and $MgCO_3$ were identified in experimental runs CZ7, CZ19, CZ4 and CZ21. In run CZ21 $SiO_2$ was preserved in the polished section while $MgCO_3$ was observed in polished section of runs CZ7 and CZ4. Textural observations suggest that $SiO_2$ and $MgCO_3$ represent precipitated phases from the high-pressure fluid. $SiO_2$ was observed in droplets (experiments CZ19 and CZ4) or as a sponge-like matrix at high-pressure condition (run CZ21). $MgCO_3$ was located in capsule fractures and at high-pressure conditions presents acicular shape. The presence of Cs, measure through WDS analyses could suggests that at

the experimental conditions, both $SiO_2$ and $MgCO_3$ were dissolved in the fluid and precipitated upon quenching.

Except for experimental run CZ7, in all the cited experimental runs the diamond trap was no longer present as a layer, this could have favor the identification of precipitates at the electron microprobe, as they were no longer trapped in the diamond layer, which is often completely removed after LA-ICP-MS analyses.

In run CZ4 only few diamonds were identified and in run CZ21 diamonds were not identified in the polished section. The lack of diamond could result from dissolution processes in $H_2O$–$CO_2$ fluids as observed by Fedortchouck et al. (2011) starting from $T$ = 1150 °C. Fedortchouck et al. (2007) observed that after 35 hours at $P$ = 1 GPa and $T$ = 1350 °C a diamond of 5 mm lose nearly the 40 wt.% of the initial weight at NNO oxygen $fH_2$ conditions. Considering that the diamonds employed in our studies are significant smaller while the experimental pressure is higher ($P$ = 2–2.1 GPa) dissolution seems to be the processes responsible for the lack of diamonds, at least at high temperature conditions.

Although the experiments performed were aimed to measure fluid composition and were not reversed, we reported in Fig 3.28 reaction 1.1. The reaction presents a weak pressure dependency and occur at higher pressure compared to the carbonation reaction of forsterite determined by Koziol & Newton (1998) in the MS + $CO_2$ system. The shift toward higher pressures is predicted also by the calculated reaction through thermodynamic model and is caused by the presence of $H_2O$ in the system. With increasing temperatures and molar fraction of $CO_2$ the reaction approach Koziol & Newton (1998) reaction as the composition of the fluid becomes more $CO_2$ rich.

At pressures above 1.5 GPa and $T$ = 700 °C, talc formation in experiment CZ12 is consistent with the calculated reaction through thermodynamic model. The reaction talc + forsterite = enstatite + $H_2O$ (Melekhova et al., 2006) is not reported as it occurs at lower temperatures ($T$ = 640 °C) at $P$ = 1.5 GPa and, by increasing pressure, it moves towards lower $T$.

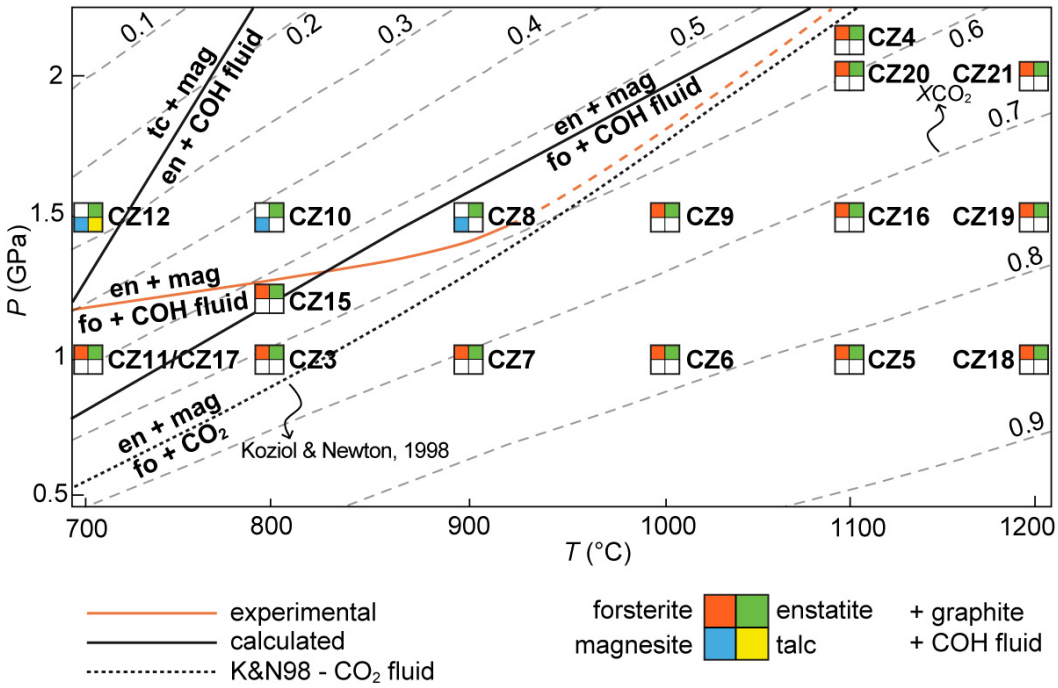


Fig. 3.28. Phase assemblages in the MS + COH system buffered at $fH_2^{NNO}$ conditions as a function of *P* and *T*. Reactions reported in black (solid lines) have been modeled with the software Perplex (Connolly, 1990) and reported as a reference (see details in Section 3.2.1). Solid orange line represent the reaction fo + COH fluid = en + mag based on the mineral assemblages observed in textural equilibrium. Dashed black line, reaction fo + $CO_2$ = en + mag from Koziol & Newton (1998). Dashed gray lines represent $XCO_2$, estimated by thermodynamic modeling of a pure GCOH fluid externally buffered by nickel-nickel oxide.

### 3.4.3. Corrected Cs dilution model based on electron microprobe observation

The cryogenic LA-ICP-MS technique relies on the use of an internal standard, cesium, to retrieve the fluid/solid ratio in the laser spot, necessary to determine the concentration of solutes in the fluid (see Section 3.2.3). Since in our study we are dealing with $H_2O$–$CO_2$ mixed fluids, to estimate the final Cs concentration in the inner capsule, we considered a dilution model that accounts for the equilibration of the GCOH fluid $fH_2^{NNO}$ conditions, which relies on two assumptions: i) fluid composition at $fH_2$ buffered conditions is controlled only by $H_2$ mobility; ii) no carbonates or hydrates occur in the experimental charge. If these assumptions are valid, equation 3.8 permits to estimate the concentration of Cs after fluid equilibration. However, carbonates (magnesite) and hydrous phases (talc) have been identified in some samples. Therefore, in these cases the second assumption necessary for the validity of Cs dilution model is not taking place anymore. In fact, the formation of carbonates or hydrates in the experimental charge consumes respectively

$CO_2$ and $H_2O$ in the inner capsule. Consequently, redox reactions involving graphite in the inner capsule and NNO buffer in the outer capsule will try to adjust the GCOH fluid composition to maintain homogeneous $fH_2$ conditions in the inner and in the outer capsules, thus leading to a different Cs concentration in the resulting fluid of the inner capsule.

For instance, the carbonation reaction 1.1 forms magnesite at the expenses of forsterite, consuming $CO_2$. To maintain the same $CO_2/H_2O$ ratio, the amount of water will decrease following CO2, i.e. $H_2$ will leave the inner capsule. Consequently, the actual available numbers of moles of $H_2O$ ($n_iH_2O$) and $CO_2$ ($n_iCO_2$) have to be recalculated to obtain the corrected Cs concentration through equation 3.8, concentration that in this case will certainly increase. The reverse is thought to occur in case of decarbonation reactions, where $H_2O$ is formed into the inner capsule thanks to $H_2$ coming from the outer capsule, so that the concentration of Cs will decrease.

## a) Carbonation and decarbonation reactions

At 1.5 GPa and 800 °C (run CZ10, see Section 3.3.2b), the forsterite present in the starting material EnMag reacted completely with $CO_2$ to form magnesite (reaction 1.1) leading to a pure assemblage enstatite + magnesite. Since we know the amount of forsterite in the starting material (see Section 1.2.1), we can calculate the moles of $CO_2$ consumed by reaction 1.1 in the inner capsule, expressed as $n_{Fo}CO_2$. We can also calculate the moles of $H_2O$ and $CO_2$ generated from the starting mixture of OAA + $H_2O$ ($n_iCO_2$ and $n_iH_2O$).

The initial number of moles of $H_2O$ in the inner capsule corrected after magnesite formation ($n_{i*}H_2O$):

$$n_{i*}\mathrm{H_2O} = n_i\mathrm{H_2O} - [n_{\mathrm{Fo}}\mathrm{CO_2} * \mathrm{H_2O}/(1 - \mathrm{H_2O})] \quad (3.9)$$

The removed quantity of $H_2O$ is expressed in equation 3.9 as the number of moles consumed by reaction 1.1 ($n_{Fo}CO_2$) multiplied by $H_2O$/(1 - $H_2O$), in which $H_2O$ is calculated through thermodynamic model and expressed as molar fraction of $H_2O$ in the COH fluid. By knowing the initial and the final quantity of $H_2O$ we can calculate the corrected initial concentration of Cs, before reaction 1.1, that is:

$$C_{i*}\mathrm{Cs} = \frac{C_i\mathrm{Cs} * n_i\mathrm{H_2O}}{n_{i*}\mathrm{H_2O}} \quad (3.10)$$

where $C_i$Cs is the concentration of Cs of the starting material (558 ppm).

At this point the calculation follows the same procedure described in Section 3.2.3. We can substitute into equation 3.8 the corrected value of the initial concentration of Cs ($C_{i*}$Cs) obtaining:

$$C_f\mathrm{Cs} = \frac{C_{i*}\mathrm{Cs} * n_{i*}\mathrm{H_2O}}{\left(\frac{X\mathrm{H_2O} * n_{i*}\mathrm{CO_2}}{1 - X\mathrm{H_2O}}\right)} \quad (3.11)$$

where $n_{i*}H_2O$ is defined by reaction 3.9 and $n_{i*}CO_2$ is given by equation:

$$n_{i*}\mathrm{CO_2} = n_{i*}\mathrm{H_2O}/[\mathrm{H_2O}/(1 - \mathrm{H_2O})] \quad (3.12)$$

The obtained corrected concentration of Cs for experiment CZ10 is 897.14 ppm, which is different from the uncorrected value of 522.83 ppm calculated without considering the change in $X$H$_2$O due to $CO_2$ sequestration in magnesite.

At $P$ = 1.5 GPa and $T$ = 900 °C (experiment CZ8) we observed growth of magnesite from the magnesite-free starting material FoEn. We retrieved the amount of forsterite that reacted with $CO_2$ forming magnesite + enstatite (reaction 1.1), which is roughly the half of the total moles of forsterite charged. By knowing the initial amount of forsterite in the capsule we can calculate the moles of $CO_2$ consumed by the reaction. Following the same procedure reported for experimental run CZ10, we estimated a concentration of Cs of 2178.8 ppm, significantly higher compared to the uncorrected concentration of 796.06 ppm.

Experimental run CZ11 (see Section 3.3.2a) at $P$ = 1 GPa and $T$ = 700 °C presented forsterite coronas on magnesite crystals, suggesting that magnesite was not a stable phase at the investigated $P$–$T$ conditions. In this case, the destabilization of magnesite increases the amount of $CO_2$ in the inner capsule, causing an opposite effect compared to carbonation reactions. In this case, $H_2$ is forced to enter from the outer capsule into the inner capsule, diluting the Cs solution. Following the same procedure previously described, we calculated the number of $CO_2$ moles in excess ($n_{\mathrm{Mag}}CO_2$) in the inner capsule by estimating the amount of magnesite destabilized. In this case Equation 3.9, has the following form:

$$n_{i*}\mathrm{H_2O} = n_i\mathrm{H_2O} + \left[n_{\mathrm{Mag}}\mathrm{CO_2} * \mathrm{H_2O}/(1 - \mathrm{H_2O})\right] \quad (3.13)$$

The estimated corrected concentration of Cs is 205 ppm, a lower concentration compared to the uncorrected value (558 ppm).

Experimental run CZ15 ($P$ = 1.2 GPa, $T$ = 800 °C) also presents an increase in the forsterite abundance relative to magnesite. To calculate the concentration of Cs we followed the same procedure given for experimental run CZ11, considering the moles of $CO_2$ released by magnesite destabilization. The estimated corrected concentration of Cs is 320.1 ppm, lower compare to the uncorrected value (1348.7 ppm).

### b) Hydration reaction

At $P$ = 1.5 GPa and $T$ = 700 °C (experiment CZ12) the stable assemblage is talc + magnesite, which results from reaction 3.3.

Water consumption in the inner capsule caused by hydrated mineral formation such as talc, do not necessary implies a variation in the concentration of Cs. As fluid equilibration is governed by $H_2$ mobility any reduction of the amount of water in the inner capsule is compensated by $H_2$ coming from the outer capsule, so no variation of Cs concentration is expected. The presence of nickel hydroxide in the outer capsule after quench demonstrates that water was not completely consumed by this process and we can assume therefore that the $fH_2$ conditions in the inner capsule were still constrained by nickel–nickel oxide buffer. However, in reaction 3.3 also $CO_2$ reacts to form magnesite. Moreover, as shown by principal component analysis, the forsterite present in the starting material EnMag, reacted completely with the $CO_2$-component of the COH fluid through reaction 1.1. For sake of simplicity, in this case we only calculated the amount of carbon dioxide consumed by reaction 1.1, following the procedure given in the previous section, considering only the carbonation reaction of forsterite and assuming that talc formation does not affect the concentration of Cs. The corrected Cs concentration is 20919.9 ppm, while the uncorrected values is 177.66 ppm.

## 3.4.4. Mineral solubility in the MS + COH system: aqueous fraction

The amounts of $SiO_2$ and MgO in the aqueous fraction of the COH fluid retrieved through the cryogenic LA-ICP-MS technique are reported in Figure 3.29.

The solubilities of all the mineral assemblages investigated in the aqueous fraction of the COH fluid increase with increasing values of $P$ and $T$. Solubilities of forsterite + enstatite in $H_2O$-only fluid (experiments CZ24 and CZ22) are lower compared to the MS + COH

system, with the exception of experimental run CZ11, which presents lower MgO content in the aqueous fraction of the COH fluid at $P$ = 1 GPa and $T$ = 700 °C (Fig. 3.29A).

In experimental runs CZ8 and CZ10 (enstatite + magnesite) the fluid presents lower solute contents compared to the fluid in equilibrium with forsterite + enstatite assemblage (Fig. 3.29), with the exception of the MgO content in experimental run at $T$ = 900 °C. In this run, we observed the precipitation of $MgCO_3$ (Section 3.4.2) that could lead to underestimate the amount of MgO in the aqueous fraction of the fluid.

The lower $m$SiO$_2$ in the aqueous fraction of the COH fluid measured in the enstatite + magnesite assemblage (Fig. 3.29) compared to the forsterite + enstatite assemblage suggests that the solubility of enstatite is lower compared to that of forsterite, feature that has also been observed in the $H_2O$-only system by Newton & Manning (2002).

Talc solubility in the aqueous fraction of the COH fluid, investigated at $P$ = 1.5 GPa and $T$ = 700 °C, presents high values of $SiO_2$ (1.5 mol/kg) and MgO (3.2 mol/kg). $m$MgO value is comparable to data of Grabman & Popp (1991), who determined the talc solubility in $H_2O$ at $P$ = 500 °C and $T$ = 0.2 GPa ($m$MgO = 2.8 mol/kg).

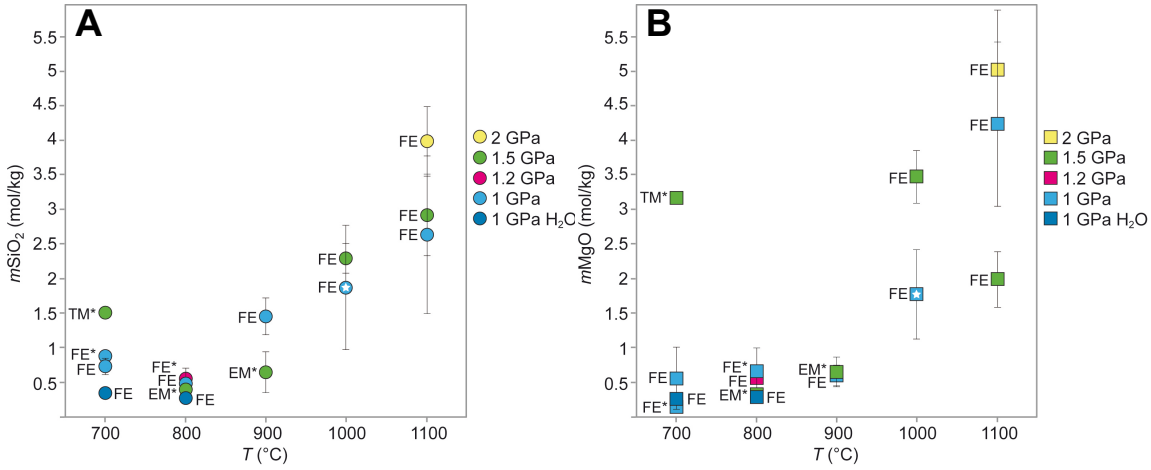


Fig. 3.29. Solute contents of $SiO_2$ (A) and MgO (B) in the aqueous fraction of the GCOH fluid as a function of $T$. The assemblages in equilibrium with the COH fluid are indicated by FE = forsterite + enstatite; TM = talc + magnesite; EM = enstatite + magnesite. Asterisks indicate results in which the Cs dilution model has been corrected for carbonation/hydration reactions. White star indicates that the solute content was retrieved without applying the Cs dilution model, as the oxygen buffer was not observed.

Comparisons with published data on forsterite and enstatite solubility in pure $H_2O$ are reported in Figure 3.30. The $SiO_2$ content in the aqueous fraction of the COH fluid is higher compared to the experimental data in the $H_2O$-only systems of Manning & Boettcher (1994) and Zhang & Frantz (2000).

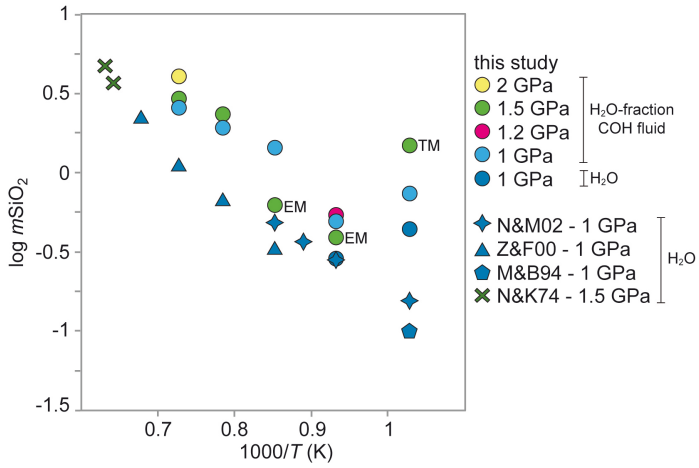


Fig. 3.30. Silica content in the $H_2O$-fraction of the COH fluid (this study) and in pure $H_2O$ expressed as log $m$SiO$_2$ *vs.* 1000/T. Experimental solubility data of mineral assemblages other than forsterite + enstatite assemblage are indicated right from the corresponding symbol. EM, enstatite+ magnesite; TM, talc + magnesite. N&K74, Nakamura & Kushiro (1974); M&B94, Manning & Boettcher (1994); Z&F00, Zhang & Frantz (2000); N&M02, Newton & Manning (2002).

On the other hand, $SiO_2$ contents in the aqueous fraction of the COH fluid are similar to the experimental data of Newton & Manning (2002) for what concern the enstatite + magnesite assemblage, whereas for the forsterite + enstatite assemblage present higher values. At higher temperature conditions, our result for the forsterite + enstatite assemblage seems consistent with the experimental data of Nakamura & Kushiro (1974) at $P$ = 1.5 GPa.

In Figure 3.31 is reported the solute content of $SiO_2$ (Fig. 3.31A) and MgO (Fig. 3.31B) in the aqueous fraction of the COH fluid plotted against the $X$CO$_2$ of the COH fluid, calculated through thermodynamic modeling. Mineral solubilities in the aqueous fraction of the COH fluid increase with increasing $CO_2$ content in the COH fluid at $T$ > 900 °C, while at lower temperature conditions the increase is less pronounced.

At $P$ = 1 GPa, $SiO_2$ content increase with increasing $X$CO$_2$ in the fluid with the exception of experimental run at $T$ = 800°C, which present lower content of $SiO_2$ in the fluid. Enstatite + magnesite solubilities in the $H_2O$ fraction also present increasing values with increasing $CO_2$-content in the fluid.

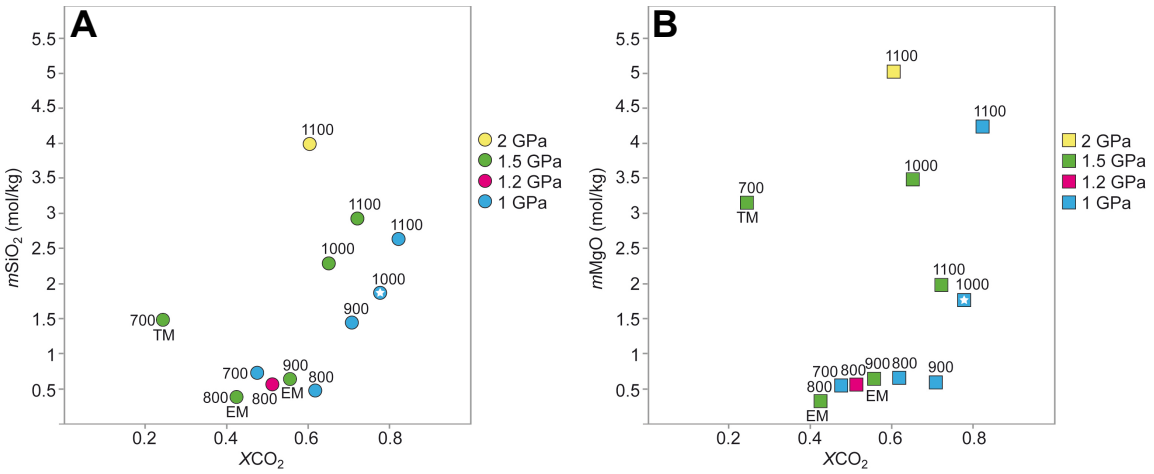


Fig. 3.31. Solute contents of $SiO_2$ (A) and MgO (B) in the aqueous fraction of the COH fluid *vs.* $XCO_2$. Values above symbols are temperatures are also reported and given in °C. Experimental data on mineral assemblage different from forsterite + enstatite assemblage are indicated right from the corresponding symbol. EM, enstatite+ magnesite; TM, talc + magnesite. $XCO_2$ has been estimated by thermodynamic modeling of a pure GCOH fluid externally buffered by nickel-nickel oxide. White star indicates experimental run in which Cs dilution model was not applied, as the oxygen buffer was not observed. At $P$ = 1 GPa and $T$ = 700 °C is reported the experimental run performed using FoEn starting material, which do not present magnesite relics.

### 3.4.5. Mineral solubility in the MS + COH system: reconstructed fluid

The solute content in the bulk COH fluid has been retrieved by rescaling the values of molality of $SiO_2$ and MgO to the amount of $H_2O$ present in the COH fluid calculated by thermodynamic modeling (Table 3.15).

Solubilities of the mineral assemblages investigated in the reconstructed GCOH fluid are reported in Figure 3.32. As the $XCO_2$ increases with increasing $T$, and decreases with increasing $P$ (see Fig. 3.31) the effect of the recalculation is maximum at $P$ = 1 GPa and $T$ = 1100 °C.

In general, we observed that the solubility in $H_2O$–$CO_2$ fluids of forsterite + enstatite and also enstatite + magnesite in terms of $m$$SiO_2$ and $m$MgO is almost independent on $T$, while $P$ exerts an important influence (Fig. 3.32).

| Run | $P$ (GPa) | $T$ (°C) | Run products | $m$SiO$_2$ (mol/kg) | $m$MgO (mol/kg) | MgO + SiO$_2$ (wt.%) | $X$(O) | log$f$O$_2$ | $X$CO$_2$ |
|---|---|---|---|---|---|---|---|---|---|
| CZ11 | 1 | 700 | fo + en | 0.48 | 0.06 | 2.95 | 0.58 | -16.35 | 0.47 |
| CZ17 | 1 | 700 | fo + en | 0.39 | 0.29 | 3.31 | 0.58 | -16.35 | 0.47 |
| CZ3 | 1 | 800 | fo + en | 0.19 | 0.26 | 2.05 | 0.68 | -14.37 | 0.62 |
| CZ7 | 1 | 900 | fo + en | 0.42 | 0.17 | 2.92 | 0.75 | -12.76 | 0.71 |
| CZ6 | 1 | 1000 | fo + en | 0.41 | 0.39 | 3.48 | 0.80 | -11.42 | 0.77 |
| CZ5 | 1 | 1100 | fo + en | 0.44 | 0.70 | 4.40 | 0.84 | -10.30 | 0.82 |
| CZ15 | 1.2 | 800 | fo + en | 0.24 | 0.26 | 3.61 | 0.63 | -14.11 | 0.54 |
| CZ12 | 1.5 | 700 | tc + mag | 0.96 | 2.01 | 13.7 | 0.45 | -15.77 | 0.24 |
| CZ10 | 1.5 | 800 | en + mag | 0.23 | 0.20 | 1.95 | 0.55 | -13.75 | 0.43 |
| CZ8 | 1.5 | 900 | en + mag | 0.28 | 0.28 | 2.62 | 0.64 | -12.14 | 0.56 |
| CZ9 | 1.5 | 1000 | fo + en | 0.79 | 1.19 | 7.61 | 0.70 | -10.81 | 0.65 |
| CZ16 | 1.5 | 1100 | fo + en | 0.79 | 0.54 | 5.67 | 0.76 | -9.69 | 0.72 |
| CZ20 | 2 | 1100 | fo + en | 1.57 | 1.95 | 2.95 | 0.67 | -9.17 | 0.60 |

Table 3.15. Solubilities of forsterite + enstatite (fo + en), enstatite + magnesite (en + mag) and talc + magnesite (tc + mag) in the reconstructed GCOH fluid. $X$(O), $f$O$_2$ and $X$CO$_2$ have been estimated by thermodynamic modeling of a pure GCOH fluid externally buffered by nickel-nickel oxide.

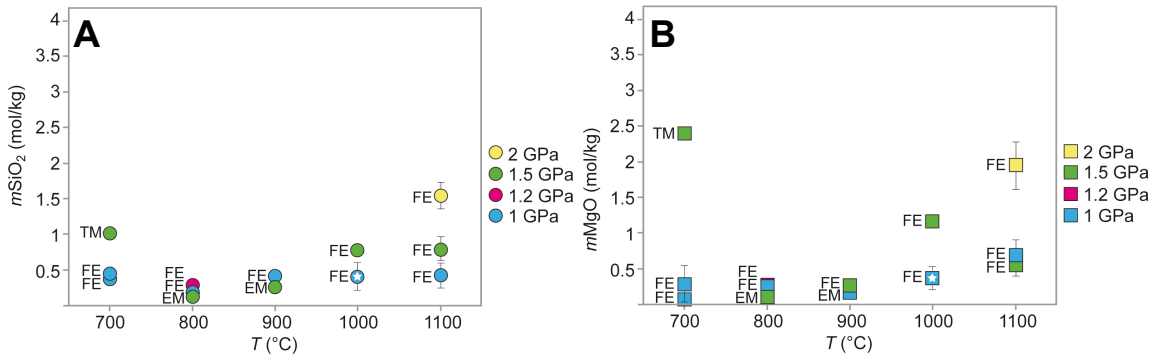


Fig. 3.32. Solute contents of SiO$_2$ (A) and MgO (B) in the GCOH fluid as a function of $T$. The assemblages in equilibrium with the reconstructed COH fluid are indicated by FE = forsterite + enstatite; TM = talc + magnesite; EM = enstatite + magnesite. White star indicates that the solute content was retrieved without applying the Cs dilution model, as the oxygen buffer was not observed

The comparison between published data on SiO$_2$ solute contents in pure water in equilibrium with forsterite + enstatite assemblages and our experimental results is reported in Fig. 3.33. In general, solubility data in COH fluids are similar or slightly lower compared to published result in H$_2$O-only fluid, with the exception of the low-$T$ experiment at $P$ = 1 GPa and $T$ = 700 °C, which deviates from the general trend characterizing data in pure H$_2$O. Also experimental run $P$ = 1.5 GPa and $T$ = 700 °C

diverge from the general trend. This could be explained in two ways: i) this run contains talc and magnesite, so the comparison with solubility data of forsterite and enstatite is not straightforward; ii) unknown uncertainties have been introduced by the Cs correction in this experiment, where both carbonation and hydration reactions occurred.

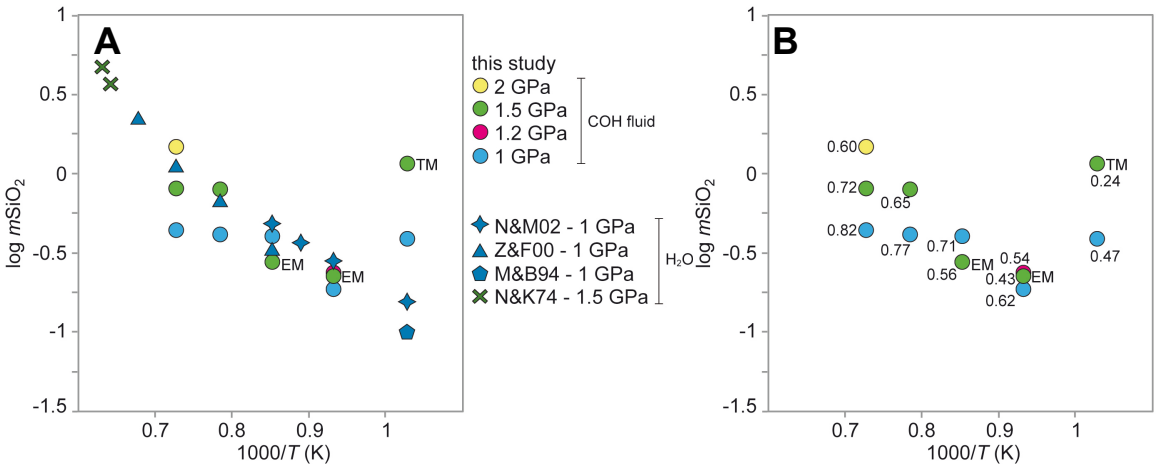


Fig. 3.33. A) Silica content in the reconstructed COH fluid (this study) and in pure $H_2O$ expressed as log $m$SiO$_2$ *vs.* 1000/T. Experimental solubility data of mineral assemblages other than forsterite + enstatite assemblage are indicated right from the corresponding symbol. EM, enstatite+ magnesite; TM, talc + magnesite. Experimental data from literature on forsterite + enstatite solubility in $H_2O$ are also reported. N&K74, Nakamura & Kushiro (1974); M&B94, Manning & Boettcher (1994); Z&F00, Zhang & Frantz (2000); N&M02, Newton & Manning (2002). B) Silica content in the reconstructed COH fluid expressed as log $m$SiO$_2$ *vs.* 1000/T. Values near symbols are the correspondent $X$CO$_2$ of the fluid, estimated by thermodynamic modeling of a pure GCOH fluid buffered at $f$H$_2$$^{NNO}$ conditions.

For what concerned MgO there are no experimental data available for comparison at the *P*–*T* conditions investigated in the $H_2O$-only system. In fact, the MgO content in the aqueous fluid is considered very low ($m$MgO < 0.3 mol/kg; Zhang & Frantz, 2000). However, in the reconstructed COH fluid the MgO content increase with *P* and *T*, as shown in Figure 3.34, suggesting that in COH fluid not only silica is brought in solution.

The amount of MgO dissolved in the COH fluid in equilibrium with the enstatite + magnesite assemblage is fairly consistent with the trend described by $CaCO_3$ dissolution in $H_2O$ at similar *P* values (Fig. 3.35) retrieved by Caciagli & Manning (2003). The authors suggest that the dissolution of calcite could result from the reaction:

$$CaCO_3 + 2\ H^+ = Ca^{2+} + CO_{2(aq)} + H_2O \qquad (3.14)$$

Analogously, magnesite dissolution could occur this way:

$$MgCO_3 + 2\ H^+ = Mg^{2+} + CO_{2(aq)} + H_2O \qquad (3.15)$$

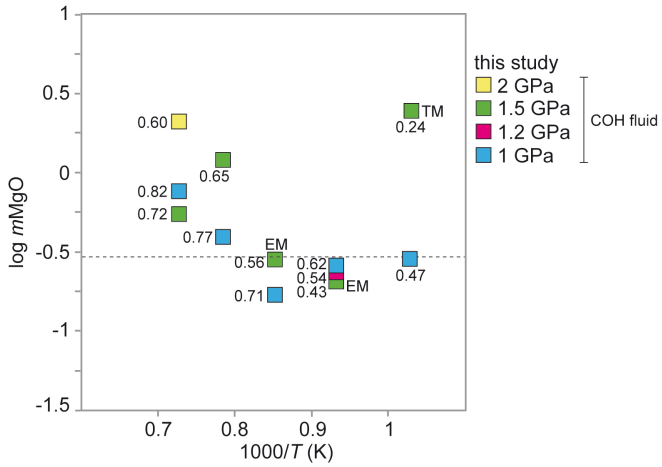


Fig. 3.34. MgO content in the COH fluid expressed as log *m*MgO *vs.* 1000/T. Experimental data on mineral assemblage different from forsterite + enstatite assemblage are specified. EM, enstatite+ magnesite; TM, talc + magnesite. The dashed line represent the upper limit of MgO content in a $H_2O$ fluid deriving from a forsterite + enstatite assemblage (Zhang & Frantz, 2000). Values near symbols are the correspondent $XCO_2$ of the fluid, estimated by thermodynamic modeling of a pure GCOH fluid buffered at $fH_2^{NNO}$ conditions.

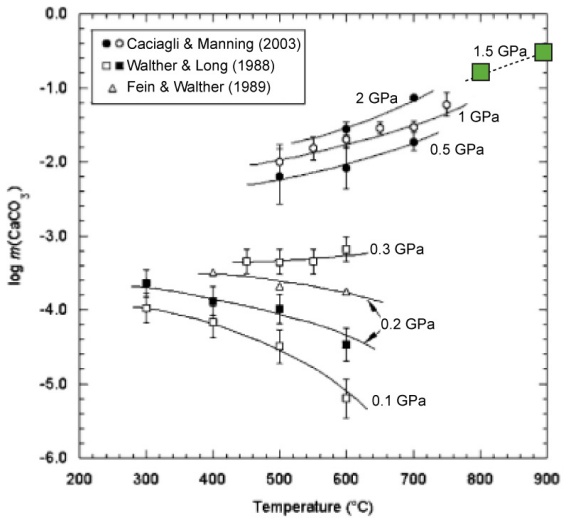


Fig. 3.35. Solubility of calcite in $H_2O$ modified after Caciagli & Manning (2003). Our experimental results on magnesite solubility in COH fluid at 1.5 GPa are reported in green and are expressed as *m*MgO.

It is also worth to mention that at $P > 4$ GPa and $T = 250–400$ °C, $CO_3^{2-}$ is thought to becomes increasingly dominant in the aqueous solution instead of $CO_{2(aq)}$ and $HCO_3^-$, as shown by Raman spectroscopy data on aragonite (Facq et al., 2014). From this result, Pan et al. (2013) proposed that the solubility for carbonate minerals at $P < 10$ GPa is given by the reaction:

$$MCO_{3(s)} = M^{2+} + CO_3^{2-} \quad (3.16)$$

Pan et al. (2013) predict at least millimolal level of $Mg^{2+}$ and $CO_3^{2-}$ at $P$ = 10 GPa and $T$ = 700 °C dissolved in the aqueous fluid. Magnesite solubility in $H_2O$ is roughly 0.1 μmol/kg at $P$ = 1 GPa and T = 1000 K following reaction 3.16. This value is six orders of magnitude smaller compared to our experimental results on magnesite solubility at $P$ = 1.5 GPa (0.2 mol/kg MgO at 800 °C), which suggest that $CO_3^{2-}$ is probably not the dominant species in COH fluids at relatively low-pressure conditions. Reaction 3.15 is probably the most promising process able to dissolve magnesite.

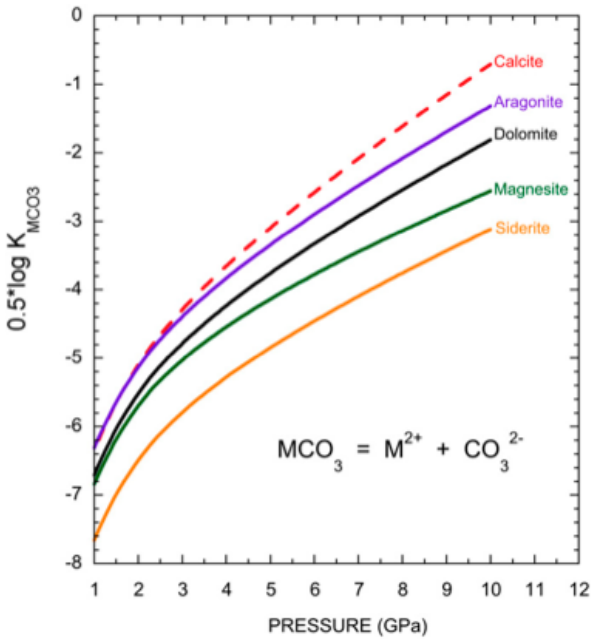


Fig. 3.36. Calculated carbonates solubilites in $H_2O$ from Pan et al. (2013).

In Fig. 3.37 we plot the total solute content (MgO + $SiO_2$) in the reconstructed COH fluid for the forsterite + enstatite and enstatite + magnesite assemblages. The total dissolve material in the COH fluid increases from 2 to 4 wt.% at $P$ = 1 GPa and $T$ from 800 to 1100 °C, reaching the 12 wt.% at $P$ = 2 GPa. By comparing the experimental results performed in the MS + COH system with results from the MS + $H_2O$ system, we observed no significant differences. The lower amount of $SiO_2$ in the COH fluid observed comparing the experimental results with data from literature (see Fig. 3.33) seems to be balanced by the increase in the MgO content in the COH fluid with increasing $XCO_2$ (see Fig. 3.34).

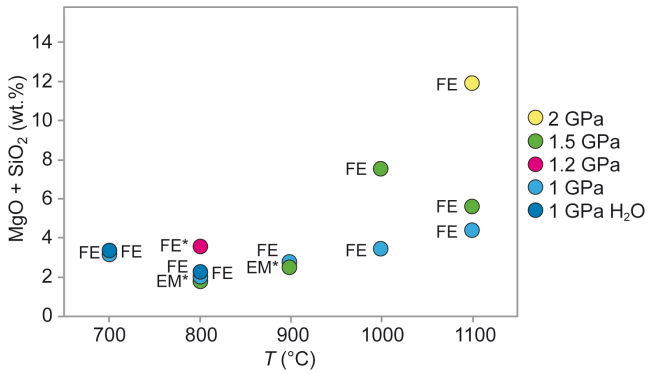


Fig. 3.36. Forsterite + enstatite (FE) and magnesite + enstatite (EM) solubilities in the reconstructed COH fluid (wt.%) *vs.* temperature. The composition of the COH fluid have been estimated by thermodynamic modeling of a pure GCOH fluid buffered at $fH_2^{NNO}$ (Perplex; Connolly, 1990). Asterisks indicate results in which the Cs dilution model has been corrected.

This could be caused by the lack of $SiO_2$ complexes with $CO_2$ at the investigated conditions, as suggested by the similar behavior of quartz solubility in $H_2O$–$CO_2$ mixtures (Walther & Orville, 1983; Newton &Manning, 2000; Shmulovich et al. 2001, 2006). The observed variations in the amount of $SiO_2$ in the COH fluid with pressure and temperature, can be attributed mainly to changes in $H_2O$ activity as suggested by Newton & Manning (2009) for the quartz + COH system. On the other hand, carbon dioxide seems to increase the amount of MgO in the COH fluid with respect to the $H_2O$ only system.

## 3.4.6. Solutes speciation

Although the identification of the solute species was beyond the purpose of this experimental work, some considerations can be made on the speciation of the solute in the MS + COH system.

Newton & Manning (2002) proposed that silica dimers are the main species resulting from forsterite and enstatite dissolution in $H_2O$. Silica dimers results from the reactions:

$$SiO_2 + 2\ H_2O = H_4SiO_4 \qquad (3.17)$$

$$2\ H_4SiO_4 = H_6Si_2O_7 + H_2O \qquad (3.18)$$

Reaction 3.17 forms orthosilicic-acid monomer and reaction 3.18 pyrosilicic-acid dimer. Zotov & Keppler (2002) indicate that aqueous fluids in equilibrium with quartz below 0.6 GPa and $T$ = 600 °C present only monomers, whereas at higher pressure and temperature

conditions monomers and dimers coexist. Above $P$ = 1.2 GPa and $T$ = 850–900 °C, silica polymers may be present in significant concentrations (Zotov & Keppler, 2002).

Given that our results are consistent with data from Newton & Manning (2002), we assume that also in the MS + COH system dimers are the dominant silica species at $T$ > 800 °C. However, we observed that in COH fluid, magnesium is an important solute constituent.

Dissolution reactions in the MS + COH system can involve the following species: $Mg_2SiO_4$, $Mg_2Si_2O_6$, $MgCO_3$, $Mg^{2+}$, $SiO_2$, $Mg(HCO_3)^+$, $Mg(HSiO_3)^+$, $MgOH^+$, $CO_3^{2-}$, $CO_2$, $H_2O$, $O_2$, $H^+$ and $OH^-$ (DEW model; Sverjensky et al., 2014). Neglecting the silica dimers and considering only dissolution reactions involving forsterite for sake of simplicity, the possible reactions in a $H_2O$–$CO_2$ fluid are:

$$2\ Mg_2SiO_4 + H_2O + 3\ CO_2 = 2\ MgCO_{3(aq)} + 2\ Mg(HSiO_3)^+ + CO_3^{2-} \quad (3.19)$$

$$Mg_2SiO_4 + H_2O + CO_2 = SiO_{2(aq)} + 2\ MgOH^+ + CO_3^{2-} \quad (3.20)$$

$$Mg_2SiO_4 + H_2O + CO_2 = Mg(HSiO_3)^+ + MgOH^+ + CO_3^{2-} \quad (3.21)$$

$$2\ Mg_2SiO_4 + H_2O + 3\ CO_2 = 2\ Mg(HSiO_3)^+ + 2\ Mg^{2+} + 3\ CO_3^{2-} \quad (3.22)$$

$$Mg_2SiO_4 + 3\ CO_2 + H_2O = 2\ Mg(HCO_3)^+ + SiO_{2(aq)} + CO_3^{2-} \quad (3.23)$$

$$Mg_2SiO_4 + 2\ CO_2 + H_2O = Mg(HCO_3)^+ + Mg(HSiO_3)^+ + 2\ CO_3^{2-} \quad (3.24)$$

$$Mg_2SiO_4 + 2\ CO_2 = 2\ MgCO_{3(aq)} + SiO_{2(aq)} \quad (3.25)$$

$$Mg_2SiO_4 + 2\ CO_2 = 2\ Mg^{2+} + SiO_{2(aq)} + 2\ CO_3^{2-} \quad (3.26)$$

These reactions provide an idea of the possible solutes occurring in a COH fluid interacting with forsterite.

For what concerned magnesite dissolution in COH fluids, we can speculate a similar behavior of calcite in $H_2O$, as the experimental results agree well with data from Caciagli & Manning (2003). Therefore, magnesite dissolution could occur following reaction 3.15.

# Chapter 4

# General discussion and conclusions

Aqueous fluids are thought to be the dominant fluid type released during subduction processes (e.g., Hermann et al., 2006). It is widely accepted that $H_2O$, resulting from dehydration reactions of hydrous minerals, is released to the overlying mantle wedge, triggering melting processes and promoting mass transfer (Schmidt & Poli, 1998; Poli & Schmidt, 2002). However, $CO_2$ content of arc magmas (e.g., Wallace, 2005) and observation of carbon-bearing phases in mantle-wedge peridotites (e.g., Malaspina & Tumiati, 2012) suggest that also carbon is released from the subducting slab (see Section 1.1).

Thermodynamic models (Kerrick & Connolly, 2001a; Connolly, 2005; Gorman et al., 2006) suggest that $CO_2$ is strongly partitioned into carbonates in subduction zones and predict low degrees of decarbonation at top-of-the-slab conditions. Experimental data (e.g., Molina & Poli, 2000; Dasgupta & Hirschmann, 2006; Poli et al., 2009; Grassi & Schmidt, 2011) also shown that the release of $CO_2$-rich fluids from the subducted slab through decarbonation reactions is unlikely, as carbonates are very stable at high-*P* conditions.

Other processed have been invoked for the transfer of carbon from the subducting slab to the mantle-wedge (e.g., carbonatitic melts), however the mechanism and magnitude of the processes remain still unresolved (see Hazen et al., 2013).

Concerning the role of fluids, Tumiati et al. (2013), combining experimental data on COH-bearing and hydrous peridotites (Fumagalli & Poli, 2005; Fumagalli et al., 2009) with the mantle-wedge hydration model proposed by Gerya & Meilick (2011), suggested that a cold COH-rich plume or diapir, which could be a major carrier of carbon from the slab to the upper mantle. Hydrous cold plumes were also suggested by Marschall & Schumacher (2012), which described blobs of low-density mélange material that rise

buoyantly from the surface of the subducting slab, transporting mélange material to lower depths.

Another relevant mechanism for the fluid-mediated transport of carbon from the slab to the mantle wedge is through carbonate dissolution (see review by Manning et al., 2013). Experimental data from Caciagli & Manning (2003) shows at high *P* conditions, the dominant species from calcite dissolution is $CO_{2(aq)}$. At *P* = 1 GPa up to 0.6 wt.% calcite is dissolved in $H_2O$ (Caciagli & Manning, 2003).

Thermodynamic models of complex fluid bearing non-volatile components (Dolejs & Manning, 2010; Sverjensky et al., 2014) confirm that with increasing pressure, the amount of dissolved material in aqueous fluids increases.

Our experimental results in the COH and MS + COH systems at *P* = 1 GPa and *T* = 700–800 °C retrieved through the capsule-piercing QMS technique, suggest that the addition of forsterite + enstatite to the COH fluid shifts the volatile speciation toward $CO_2$ at fixed *P*–*T*–$fH_2$ conditions (see Chapter 2). At *P* = 1 GPa, data show an increase in $CO_2$ of + 11 mol% at *T* = 800 °C and of + 26 mol% at *T* = 900 °C in the COH fluid in equilibrium with forsterite + enstatite compared to a pure COH fluid. Although at this stage we only speculate about a process able to induce this difference, it appears evident that the increased amount of $CO_2$ is related to an interaction of the COH fluid with solid phases, in particular with the assemblage forsterite + enstatite, which represents a model upper-mantle mineralogical composition. We have seen in Chapter 3 that the solubility of mantle minerals in COH fluids is not lowered by the presence of $CO_2$, but presents similar values compared by the solubility in pure $H_2O$. In Section 3.4.6, we suggest a series of possible dissolution reactions of forsterite (reactions 3.19–3.26), producing dissolved species containing carbon, such as $CO_3^{2-}$ and $Mg(HCO_3)^+$. These species will increase the amount of carbon in the fluid, but not in $CO_2$ species. In order to get the increase of $CO_2$ that we observed in our experiments, we suggest the possible following reactions occurring in addition to reactions 3.19–3.26:

$$CO_3^{2-} + H^+ = CO_{2(aq)} + OH^- \quad (4.1)$$

$$Mg(HCO_3)^+ + H^+ = Mg^{2+} + CO_{2(aq)} + H_2O \quad (4.2)$$

By combining these reactions with the forsterite-dissolution reaction 3.18, we can write the following reaction:

$2\ Mg_2SiO_4 + 3\ CO_2 + 5\ H^+ =$

$$2\ Mg^{2+} + 3\ CO_{2(aq)} + 1.5\ H_2O + 2\ Mg(HSiO_3)^+ + OH^- \qquad (4.3)$$

where the species $CO_{2(aq)}$ occurs instead of carbonate species. Unlike carbonate species, the specie $CO_{2(aq)}$ can be exsolved at subsolvus *P–T–X* conditions, so these reactions could at least partially explain the increase in $CO_2$ we observed. The amount of $CO_{2(aq)}$ is proportional to the amount of forsterite dissolved in the fluid. Following our data, this amount is 2–4 wt.% at *P* = 1 GPa and *T* = 800–1100 °C, and 12 wt.% at *P* = 2 GPa and T = 1100 °C. Moreover, according to Zotov & Keppler (2000, 2002), silica-dimer forming reactions are dehydration reactions (reactions 3.17 and 3.18). Therefore, they could modify the composition of the COH fluid by increasing $XCO_2$. Dissolution of mantle minerals such as forsterite and enstatite, could contribute to increase the amount of $CO_2$ in high-pressure COH fluid.

As a consequence, the total amount of $CO_2$ retained in COH fluids infiltrating the mantle-wedge could be remarkably high, and in any case much more compared to the quantities predicted by thermodynamic models in the simple COH system.

# Acknowledgments

First I would like to thank my PhD advisor Simone Tumiati, who constantly pushed me to improve as experimental petrologist. I'm very grateful for the time he dedicated to support my research and for guided me during the last three years. Thanks for being a great supervisor, a wise "zen master" and a good friend.

A huge thanks goes to Patrizia Fumagalli and Stefano Poli, their guidance during my PhD studies has been fundamental to go through this dissertation. Thanks for the interesting discussions, comments and feedbacks. I truly enjoyed working in the group of Experimental Petrology, and I consider myself very lucky to have had the opportunity to share with you these three years of studies.

I would like to thank Peter Ulmer (ETH Zurich) for giving me the chance to spend 4 months at ETH Zurich and for helping me to figure out how to analyze double capsules with the freezing technique. Thanks to Thomas Pettke (University of Bern) for the assistance during LA-ICP-MS sessions and for the stimulating discussions on high-pressure fluids.

Thanks to Sandro Recchia (University of Insubria) for his fundamental contribution to develop and assemble the capsule-piercing device and for the assistance in COH volatile speciation analyses.

Thanks to Andrea Risplendente (University of Milan) for his great support during electron microprobe analyses. Stefanie Luginbuehl (ETH Zurich) is gratefully acknowledged for the Cs-solution employed in freezing experiments. Monica Dapiaggi (University of Milan) is thanked for the diffraction data on the starting materials. Thanks to Francesca Miozzi (University of Milan) for being a very helpful master student.

I would like to thank my PhD fellows Irene Fantone and Paolo Lotti, for the important scientific breakthrough that we shared during countless coffee breaks and for being great friends.

I'm also grateful to the department colleagues of the "kitchen", thanks for share with me lunches and laughter.

More personally, I would like to thank my family. Thanks mom and dad for supporting me even if I was a horrible teenager.
And a special thanks to Giorgio, this dissertation would not have been completed without your support.

# Appendix

| Run | *P* (GPa) | *T* (°C) | Oxygen buffer | Graphite (g) | OAD (g) | Oxygen buffer (g) |
|---|---|---|---|---|---|---|
| COH11 | $1 \cdot 10^{-9}$ | 250 | - | - | 0.0010 | - |
| COH36 | $1 \cdot 10^{-9}$ | 250 | - | - | 0.0010 | - |
| COH12 | $1 \cdot 10^{-9}$ | 250 | IW | 0.0012 | 0.0011 | 0.0019 |
| COH26 | 1 | 800 | - | 0.0088 | 0.0083 | - |
| COH27 | 1 | 800 | - | 0.0093 | 0.0091 | - |
| COH14 | 1 | 800 | IW | 0.0044 | 0.0034 | 0.0039 |
| COH15 | 1 | 800 | HM | 0.0051 | 0.0038 | 0.0063 |
| COH19 | 1 | 800 | NNO | 0.0049 | 0.0043 | 0.0243 |
| COH20 | 1 | 800 | NNO | 0.0063 | 0.0058 | 0.0176 |
| COH25 | 1 | 900 | - | 0.0096 | 0.0095 | - |
| COH28 | 1 | 900 | - | 0.0114 | 0.0149 | - |
| COH32 | 1 | 900 | NNO | 0.0069 | 0.0109 | 0.1938 |
| COH29 | 1 | 900 | NNO | 0.0068 | 0.0054 | 0.0212 |
| COH16 | 3 | 1000 | NNO | 0.0058 | 0.0042 | 0.0066 |

Tab. A.1. Weighted quantities of the materials loaded into single capsule experiments in the COH-only system. OAD, oxalic acid dihydrate.

| Run | *P* (GPa) | *T* (°C) | Graphite (g) | OAD (g) | FoEn | Fluid /solid (wt.%) | $H_2O$ (OC, g) | NNO (OC, g) |
|---|---|---|---|---|---|---|---|---|
| COH18 | 1 | 800 | 0.0020 | 0.0058 | - | 100.0 | 0.0067 | 0.0526 |
| CM3 | 1 | 800 | 0.0010 | 0.0028 | 0.0102 | 27.45 | 0.0064 | 0.0570 |
| COH30 | 1 | 900 | 0.0043 | 0.0030 | - | 100.0 | 0.0090 | 0.0490 |
| CM7 | 1 | 900 | 0.0007 | 0.0026 | 0.0089 | 29.83 | 0.0062 | 0.0513 |

Tab. A.2. Weighted quantities of the materials loaded into double capsule experiments in the COH and MS + COH system. OAD, oxalic acid dihydrate; OC, outer capsule.

| Run | *P* (GPa) | *T* (°C) | Graphite (g) | Cs-doped $H_2O$ (g) | OAA (g) | FoEn or EnMag | Fluid/solid (wt.%) | $H_2O$ (OC, g) | NNO (OC, g) |
|---|---|---|---|---|---|---|---|---|---|
| CZ11 | 1 | 700 | 0.0006 | 0.0006 | 0.0014 | 0.0102 | 19.77 | 0.0040 | 0.0197 |
| CZ17 | 1 | 700 | 0.0009 | 0.0006 | 0.0013 | 0.0092 | 20.13 | 0.0039 | 0.0198 |
| CZ24 | 1 | 700 | - | 0.0020 | - | 0.0313 | 6.25 | - | - |
| CZ3 | 1 | 800 | 0.0008 | 0.0006 | 0.0017 | 0.0098 | 24.34 | 0.0030 | 0.0197 |
| CZ22 | 1 | 800 | - | 0.0039 | - | 0.0236 | 16.55 | - | - |
| CZ7 | 1 | 900 | 0.0006 | 0.0006 | 0.0013 | 0.0101 | 19.03 | 0.0032 | 0.0190 |
| CZ6 | 1 | 1000 | 0.0005 | 0.0007 | 0.0014 | 0.0101 | 20.06 | 0.0033 | 0.0197 |
| CZ5 | 1 | 1100 | 0.0002 | 0.0008 | 0.0015 | 0.0102 | 21.78 | 0.0031 | 0.0194 |
| CZ18 | 1 | 1200 | 0.0011 | 0.0006 | 0.0013 | 0.0095 | 19.64 | 0.0040 | 0.0188 |
| CZ15 | 1.2 | 800 | 0.0013 | 0.0008 | 0.0010 | 0.0104 | 17.34 | 0.0048 | 0.0196 |
| CZ12 | 1.5 | 700 | 0.0011 | 0.0006 | 0.0017 | 0.0103 | 22.72 | 0.0052 | 0.0231 |
| CZ10 | 1.5 | 800 | 0.0014 | 0.0007 | 0.0015 | 0.0100 | 22.08 | 0.0045 | 0.0224 |
| CZ8 | 1.5 | 900 | 0.0006 | 0.0006 | 0.0015 | 0.0101 | 20.91 | 0.0032 | 0.0194 |
| CZ9 | 1.5 | 1000 | 0.0004 | 0.0007 | 0.0015 | 0.0105 | 20.40 | 0.0028 | 0.0194 |
| CZ16 | 1.5 | 1100 | 0.0014 | 0.0006 | 0.0011 | 0.0090 | 18.34 | 0.0041 | 0.0207 |
| CZ19 | 1.5 | 1200 | 0.0014 | 0.0005 | 0.0016 | 0.0090 | 23.45 | 0.0041 | 0.0219 |
| CZ20 | 2 | 1100 | 0.0013 | 0.0010 | 0.0016 | 0.0090 | 28.84 | 0.0043 | 0.0226 |
| CZ21 | 2 | 1200 | 0.0010 | 0.0006 | 0.0013 | 0.0083 | 22.84 | 0.0041 | 0.0149 |
| CZ4 | 2.1 | 1100 | 0.0005 | 0.0007 | 0.0015 | 0.0098 | 22.38 | 0.0031 | 0.0191 |

Tab. A.3. Weighted quantities of the materials loaded into double capsule experiments in the MS + COH system. OAD, oxalic acid dihydrate; OC, outer capsule.

| Run | CZ11/CZ17 | CZ3 | CZ7 | CZ6 | CZ5 | CZ18 | CZ15 | CZ12 |
|---|---|---|---|---|---|---|---|---|
| $P$ (GPa) | 1 | 1 | 1 | 1 | 1 | 1 | 1.2 | 1.5 |
| $T$ (°C) | 700 | 800 | 900 | 1000 | 1100 | 1200 | 800 | 700 |
| $\log fO_2^{NNO}$ OC | -15.777 | -13.468 | -11.557 | -9.949 | -8.577 | -7.394 | -13.383 | -15.542 |
| $X$(O) OC | 0.33330 | 0.33327 | 0.33321 | 0.33312 | 0.33301 | 0.33287 | 0.33328 | 0.33332 |
| $\log fH_2^{NNO}$ OC = IC | 1.63832 | 1.77544 | 1.88428 | 1.97234 | 2.04308 | 2.10078 | 1.92820 | 2.01511 |
| $X$(O) IC | 0.58300 | 0.67800 | 0.74500 | 0.79800 | 0.83700 | 0.86700 | 0.62600 | 0.45100 |
| $\log fO_2^{NNO}$ IC | -16.346 | -14.368 | -12.759 | -11.421 | -10.296 | -9.342 | -14.107 | -15.767 |
| $H_2O$ | 0.524 | 0.380 | 0.287 | 0.217 | 0.167 | 0.129 | 0.457 | 0.755 |
| $CO_2$ | 0.473 | 0.613 | 0.696 | 0.745 | 0.759 | 0.741 | 0.539 | 0.244 |
| $XCO_2$ | 0.474 | 0.617 | 0.708 | 0.774 | 0.820 | 0.852 | 0.541 | 0.244 |

Tab. A.4. Thermodynamic model of GCOH fluid performed with the software Perplex (Connolly, 1990). $\log fO_2^{NNO}$ OC is derived with the routine "vertex". $X$(O), $\log fH_2^{NNO}$ and $\log fO_2^{NNO}$ IC are retrieved with the routine "fluids". OC, outer capsule; IC, inner capsule. In the outer capsule the fluid is constituted by $H_2O$-only

| Run | CZ10 | CZ8 | CZ9 | CZ16 | CZ19 | CZ20 | CZ21 | CZ4 |
|---|---|---|---|---|---|---|---|---|
| $P$ (GPa) | 1.5 | 1.5 | 1.5 | 1.5 | 1.5 | 2 | 2 | 2.1 |
| $T$ (°C) | 800 | 900 | 1000 | 1100 | 1200 | 1100 | 1200 | 1100 |
| $\log fO_2^{NNO}$ OC | -13.255 | -11.361 | -9.768 | -8.410 | -7.238 | -8.243 | -7.082 | -8.209 |
| $X$(O) OC | 0.33329 | 0.33325 | 0.33319 | 0.33311 | 0.33301 | 0.33317 | 0.33309 | 0.33318 |
| $\log fH_2^{NNO}$ OC = IC | 2.13992 | 2.24192 | 2.31790 | 2.37856 | 2.42950 | 2.67309 | 2.71578 | 2.72867 |
| $X$(O) IC | 0.55300 | 0.63600 | 0.70300 | 0.75600 | 0.79800 | 0.67000 | 0.72100 | 0.65300 |
| $\log fO_2^{NNO}$ IC | -13.754 | -12.141 | -10.810 | -9.693 | -8.744 | -9.172 | -8.229 | -9.076 |
| $H_2O$ | 0.573 | 0.441 | 0.343 | 0.270 | 0.214 | 0.390 | 0.316 | 0.415 |
| $CO_2$ | 0.424 | 0.552 | 0.640 | 0.695 | 0.720 | 0.593 | 0.650 | 0.571 |
| $XCO_2$ | 0.425 | 0.556 | 0.651 | 0.720 | 0.771 | 0.604 | 0.673 | 0.579 |

Tab. A.5. Thermodynamic model of GCOH fluid performed with the software Perplex (Connolly, 1990). $\log fO_2^{NNO}$ OC is derived with the routine "vertex". $X$(O), $\log fH_2^{NNO}$ and $\log fO_2^{NNO}$ IC are retrieved with the routine "fluids". OC, outer capsule; IC, inner capsule. In the outer capsule the fluid is constituted by $H_2O$-only

# References


Aerts, M., Hack, A.C., Reusser, E., Ulmer, P. (2010) Assessment of the diamond-trap method for studying high-pressure fluids and melts and an improved freezing stage design for laser ablation ICP-MS analysis. *American Mineralogist, 95*, 1523-1526.

Akaishi, M., Kumar, S., Kanda, H., Yamaoka, S. (2000) Formation process of diamond from supercritical $H_2O$–$CO_2$ fluid under high pressure and high temperature conditions. *Diamond and Related Materials*, *9*(12), 1945-1950.

Andersen, T., Neumann, E.R. (2001) Fluid inclusions in mantle xenoliths. *Lithos*, *55*(1), 301-320.

Anderson, G., Burnham, C.W. (1965) The solubility of quartz in super-critical water. *American Journal of Science*, *263*(6), 494-511.

Antignano, A., Manning, C.E. (2008a) Fluorapatite solubility in $H_2O$ and $H_2O$–NaCl at 700 to 900 °C and 0.7 to 2.0 GPa. *Chemical Geology*, *251*(1), 112-119.

Antignano, A., Manning, C.E. (2008b) Rutile solubility in $H_2O$, $H_2O$–$SiO_2$, and $H_2O$–$NaAlSi_3O_8$ fluids at 0.7–2.0 GPa and 700–1000 °C: implications for mobility of nominally insoluble elements. *Chemical Geology*, *255*, 283-293.

Aranovich, L.Y., Newton, R.C. (1999) Experimental determination of $CO_2$–$H_2O$ activity-composition relations at 600–1000 °C and 6-14 kbar by reversed decarbonation and dehydration reactions. *American Mineralogist*, *84*, 1319-1332.

Ardia, P., Hirschmann, M.M., Withers, A.C., Tenner, T.J. (2012) $H_2O$ storage capacity of olivine at 5–8 GPa and consequences for dehydration partial melting of the upper mantle. *Earth and Planetary Science Letters*, *345*, 104-116.

Audétat, A., Keppler, H. (2005) Solubility of rutile in subduction zone fluids, as determined by experiments in the hydrothermal diamond anvil cell. *Earth and Planetary Science Letters*, *232*(3), 393-402.

Baker, M.B., Stolper, E.M. (1994) Determining the composition of high-pressure mantle melts using diamond aggregates. *Geochimica et Cosmochimica Acta, 58*, 2811-2827.

Bali, E., Zajacz, Z., Kovács, I., Szabó, C. S., Halter, W., Vaselli, O., Török, K., Bodnar, R.J. (2008) A quartz-bearing orthopyroxene-rich websterite xenolith from the Pannonian Basin, Western Hungary: evidence for release of quartz-saturated melts from a subducted slab. *Journal of Petrology*, *49*(3), 421-439.

Bebout, G.E. (1995) The impact of subduction-zone metamorphism on mantle-ocean chemical cycling. *Chemical Geology, 126*, 191-218.

Becker, K.H., Cemič, L., Langer, K.E. (1983) Solubility of corundum in supercritical water. *Geochimica et Cosmochimica Acta*, *47*(9), 1573-1578.

Bergman, S.C., Dubessy, J. (1984) $CO_2$-CO fluid inclusions in a composite peridotite xenolith: implications for upper mantle oxygen fugacity. *Contributions to Mineralogy and Petrology*, *85*(1), 1-13.

Berkesi, M., Hidas, K., Guzmics, T., Dubessy, J., Bodnar, R.J., Szabo, C., Vajna, B., Tsunogae, T. (2009) Detection of small amounts of $H_2O$ in $CO_2$-rich fluid inclusions using Raman spectroscopy. *Journal of Raman Spectroscopy*, *40*(11), 1461-1463.

Berndt, M.E., Allen, D.E., Seyfried, W.E. (1996) Reduction of $CO_2$ during serpentinization of olivine at 300 C and 500 bar. *Geology*, *24*(4), 351-354.

Berry, A.J., Hermann, J., O'Neill, H.S., Foran, G.J. (2005) Fingerprinting the water site in mantle olivine. *Geology*, *33*(11), 869-872.

Bose, K., Ganguly, J. (1995) Quartz-coesite transition revisited: Reversed experimental determination at 500–1200 °C and retrieved thermochemical properties. *American Mineralogist*, *80*, 231-231.

Bowen, N.L. (1928) The evolution of igneous rocks. *Dover Publications*.

Bowers, T.S., Helgeson, H.C. (1983) Calculation of the thermodynamic and geochemical consequences of nonideal mixing in the system $H_2O$–$CO_2$–NaCl on phase relations in geologic systems: Equation of state for $H_2O$–$CO_2$–NaCl fluids at high pressures and temperatures. *Geochimica et Cosmochimica Acta*, *47*(7), 1247-1275.

Brey, G.P., Bulatov, V.K., Girnis, A.V., Lahaye, Y. (2008) Experimental melting of carbonated peridotite at 6-10 GPa. *Journal of Petrology, 49*, 797-821.

Burnham, C.W., Jahns, R.H. (1962) A method for determining the solubility of water in silicate melts. *American Journal of Science*, *260*(10), 721-745.

Caciagli, N.C., Manning, C.E. (2003) The solubility of calcite in water at 6-16 kbar and 500-800 °C. *Contributions to Mineralogy and Petrology, 146*, 275-285.

Chepurov, A.I., Tomilenko, A.A., Zhimulev, E.I., Sonin, V.M., Chepurov, A.A., Kovyazin, S.V., Timina, T.Y., Surkov, N.V. (2012) The conservation of an aqueous fluid in inclusions in minerals and their interstices at high pressures and temperatures during the decomposition of antigorite. *Russian Geology and Geophysics*, *53*(3), 234-246.

Conceição, R.V., Green, D.H. (2004) Derivation of potassic (shoshonitic) magmas by decompression melting of phlogopite+pargasite lherzolite. *Lithos, 72*, 209-229.

Connolly, J.A.D. (1990) Multivariable phase diagrams; an algorithm based on generalized thermodynamics. *American Journal of Science, 290*, 666-718.

Connolly, J.A.D. (1995) Phase diagram methods for graphitic rocks and application to the system C−O−H−FeO−$TiO_2$−$SiO_2$. *Contributions to Mineralogy and Petrology, 119*, 94-116.

Connolly, J.A.D. (2005) Computation of phase equilibria by linear programming: a tool for geodynamic modeling and its application to subduction zone decarbonation. *Earth and Planetary Science Letters*, *236*(1), 524-541.

Connolly, J.A.D., Cesare, B. (1993) C−O−H−S fluid composition and oxygen fugacity in graphitic metapelites. *Journal of Metamorphic Geology*, *11*(3), 379-388.

Dasgupta, R., Hirschmann, M.M. (2006) Melting in the Earth's deep upper mantle caused by carbon dioxide. *Nature, 440*, 659-662.

Dasgupta, R., Hirschmann, M.M. (2007) Effect of variable carbonate concentration on the solidus of mantle peridotite. *American Mineralogist, 92*, 370-379.

Dolejs, D., Manning, C.E. (2010) Thermodynamic model for mineral solubility in aqueous fluids: theory, calibration and application to model fluid-flow systems. *Geofluids, 10*, 20-40.

Dvir, O., Angert, A., Kessel, R., 2013. Determining the composition of C−H−O liquids following high-pressure and high-temperature diamond-trap experiments. *Contributions to Mineralogy and Petrology, 165*, 593-599.

Eggler, D.H (1978) The effect of $CO_2$ upon partial melting of peridotite in the system $Na_2O$–CaO–$Al_2O_3$–MgO–$SiO_2$–$CO_2$ to 35 kb, with an analysis of melting in a peridotite–$H_2O$–$CO_2$ system. *American Journal of Science, 278*, 305-343.

Eggler, D.H. (1974) Effect of $CO_2$ on the melting of peridotite. *Carnegie Institution of Washington Yearbook, 72*, 457-467.

Eggler, D.H. (1975) Peridotite–carbonate relations in the system CaO–MgO–$SiO_2$–$CO_2$. *Carnegie Institution of Washington Yearbook, 74*, 468-474.

Eggler, D.H., Mysen, B.O., Hoering, T.C. (1979) The solubility of carbon monoxide in silicate melts at high pressures and its effect on silicate phase relations. *Earth and Planetary Science Letters, 43*, 321-330.

Eugster, H.P. (1957) Heterogeneous reactions involving oxidation and reduction at high pressures and temperatures. *The Journal of Chemical Physics, 26*, 1760-1761.

Eugster, H.P., Skippen, G.B. (1967) Igneous and metamorphic reactions involving gas equilibria. *Researches in Geochemistry, 2*, 492-520.

Facq, S., Daniel, I., Montagnac, G., Cardon, H., Sverjensky, D.A. (2014) In situ Raman study and thermodynamic model of aqueous carbonate speciation in equilibrium with aragonite under subduction zone conditions. *Geochimica et Cosmochimica Acta*, *132*, 375-390.

Falloon, T.J., Green, D.H. (1989) The solidus of carbonated, fertile peridotite. *Earth and Planetary Science Letters*, *94*(3), 364-370.

Falloon, T.J., Green, D.H., Danyushevsky, L.V., Faul, U.H. (1999) Peridotite melting at 1.0 and 1.5 GPa: An experimental evaluation of techniques using diamond aggregates and mineral mixes for determination of near-solidus melts. *Journal of Petrology, 40*, 1343-1375.

Fedortchouk, Y., Canil, D., Semenets, E. (2007) Mechanisms of diamond oxidation and their bearing on the fluid composition in kimberlite magmas. *American Mineralogist*, *92*(7), 1200-1212.

Fedortchouk, Y., Manghnani, M.H., Hushur, A., Shiryaev, A., Nestola, F. (2011) An atomic force microscopy study of diamond dissolution features: The effect of $H_2O$ and $CO_2$ in the fluid on diamond morphology. *American Mineralogist*, *96*(11-12), 1768-1775.

Fein, J.B., Walther, J.V. (1989) Calcite solubility and speciation in supercritical NaCl–HCl aqueous fluids. *Contributions to Mineralogy and Petrology*, *103*(3), 317-324.

Ferraris, C., Grobety, B., Früh-Green, G.L., Wessicken, R. (2004) Intergrowth of graphite within phlogopite from Finero ultramafic complex (Italian Western Alps) implications for mantle crystallization of primary-texture mica. *European Journal of Mineralogy*, *16*(6), 899-908.

Foley, S.F., Yaxley, G.M., Rosenthal, A., Buhre, S., Kiseeva, E.S., Rapp, R.P., Jacob, D. E. (2009) The composition of near-solidus melts of peridotite in the presence of $CO_2$ and $H_2O$ between 40 and 60 kbar. *Lithos, 1125*, 274-283.

Frantz, J.D., Dubessy, J., Mysen, B.O. (1994) Ion-pairing in aqueous $MgSO_4$ solutions along an isochore to 500 °C and 11 kbar using Raman spectroscopy in conjunction with the diamond-anvil cell. *Chemical Geology*, *116*(3), 181-188.

French, B.M. (1966) Some geological implications of equilibrium between graphite and a C–H–O gas phase at high temperatures and pressures. *Reviews of Geophysics, 4*(2), 223-253.

Frezzotti M.L., Di Vincenzo G., Ghezzo C., Burke E.A.J. (1994) Evidence of magmatic $CO_2$-rich fluids in peraluminous graphite-bearing leucogranites from Deep Freeze Range (northern Victoria Land, Antarctica). *Contributions to Mineralogy and Petrology*, *117*(2), 111-123.

Frezzotti, M.L., Huizenga, J.M., Compagnoni, R., Selverstone, J. (2013) Diamond formation by carbon saturation in C–O–H fluids during cold subduction of oceanic lithosphere. *Geochimica et Cosmochimica Acta, 143*, 68-86.

Frezzotti, M.L., Peccerillo, A. (2007) Diamond-bearing COHS fluids in the mantle beneath Hawaii. *Earth and Planetary Science Letters*, *262*(1), 273-283.

Frezzotti, M.L., Selverstone, J., Sharp, Z.D., Compagnoni, R. (2011) Carbonate dissolution during subduction revealed by diamond-bearing rocks from the Alps. *Nature Geoscience, 4*, 703-706.

Fu, B., Touret, J.L., Zheng, Y.F., Jahn, B.M. (2003a) Fluid inclusions in granulites, granulitized eclogites and garnet clinopyroxenites from the Dabie–Sulu terranes, eastern China. *Lithos*, *70*(3), 293-319.

Fu, B., Touret, J.L.R., Zheng, Y.F. (2003b) Remnants of premetamorphic fluid and oxygen isotopic signatures in eclogites and garnet clinopyroxenite from the Dabie–Sulu terranes, eastern China. *Journal of metamorphic Geology*, *21*(6), 561-578.

Fumagalli, P., Poli, S. (2005) Experimentally determined phase relations in hydrous peridotites to 6.5 GPa and their consequences on the dynamics of subduction zones. *Journal of Petrology, 46*, 555-578.

Fumagalli, P., Zanchetta, S., Poli, S. (2009) Alkali in phlogopite and amphibole and their effects on phase relations in metasomatized peridotites: a high-pressure study. *Contributions to Mineralogy and Petrology*, *158*(6), 723-737.

Gerya, T.V., Meilick, F.I. (2011) Geodynamic regimes of subduction under an active margin: effects of rheological weakening by fluids and melts. *Journal of Metamorphic Geology*, *29*(1), 7-31.

Goncharov, A.G., Ionov, D.A., Doucet, L.S., Pokhilenko, L.N. (2012) Thermal state, oxygen fugacity and C-O-H fluid speciation in cratonic lithospheric mantle: New data on peridotite xenoliths from the Udachnaya kimberlite, Siberia. *Earth and Planetary Science Letters*, *357*, 99-110.

Goranson, R.W. (1931) The solubility of water in granite magmas. *American Journal of Science, 22*, 481-502.

Gorman, P.J., Kerrick, D.M., Connolly, J.A.D. (2006) Modeling open system metamorphic decarbonation of subducting slabs. *Geochemistry Geophysics Geosystems, 7*(4), doi:10.1029/2005GC001125.

Grassi, D., Schmidt, M.W. (2011) The melting of carbonated pelites from 70 to 700 km depth. *Journal of Petrology, 4,* 765-789.

Green, D.H. (1973) Experimental melting studies on a model upper mantle composition at high pressure under water-saturated and water-undersaturated conditions. *Earth and Planetary Science Letters, 19*, 37-53.

Green, D.H., Falloon, T.J. (1998) Pyrolite: a Ringwood concept and its current expression. *The Earth's Mantle: Composition, Structure, and Evolution*, 311-380.

Green, D.H., Hibberson, W.O., Rosenthal, A., Kovács, I., Yaxley, G.M., Falloon, T.J., Brink, F. (2014) Experimental Study of the Influence of Water on Melting and Phase Assemblages in the Upper Mantle. *Journal of Petrology*, *55*(10), 2067-2096.

Guillong, M., Meier, D.L., Allan, M.M., Heinrich, C.A., Yardley, B.W.D. (2008) SILLS: a MATLAB-based program for the reduction of laser ablation ICP-MS data of homogeneous materials and inclusions. *Mineralogical Association of Canada Short Course*, *40*, 328-333.

Hamilton, D.L., Burnham, C.W., Osborn, E.F. (1964) The solubility of water and effects of oxygen fugacity and water content on crystallization in mafic magmas. *Journal of Petrology*, *5*(1), 21-39.

Hazen, R.M., Jones, A.P., Baross, J.A. (2013) Carbon in earth. *Reviews in Mineralogy and Geochemistry*, *75*.

Hermann, J., Spandler, C., Hack, A., Korsakov, A.V. (2006) Aqueous fluids and hydrous melts in high-pressure and ultra-high pressure rocks: implications for element transfer in subduction zones. *Lithos, 92*, 399-417.

Hidas, K., Guzmics, T., Szabó, C., Kovács, I., Bodnar, R. J., Zajacz, Z., Nèdli, Z., Vaccari, L., Perucchi, A. (2010) Coexisting silicate melt inclusions and $H_2O$-bearing, $CO_2$-rich fluid inclusions in mantle peridotite xenoliths from the Carpathian–Pannonian region (central Hungary). *Chemical Geology*, *274*(1), 1-18.

Holland, T.J.B., Powell, R. (1998) An internally consistent thermodynamic data set for phases of petrological interest. *Journal of metamorphic Geology*, *16*(3), 309-343.

Holloway, J.R. (1977) Fugacity and activity of molecular species in supercritical fluids. *Thermodynamics in Geology*, 161-181.

Holloway, J.R. (1987) Igneous fluids. *Reviews in Mineralogy and Geochemistry*, *17*(1), 211-233.

Holloway, J.R., Burnham, C.W., Millhollen, G.L. (1968) Generation of $H_2O$-$CO_2$ Mixtures for Use in Hydrothermal Experimentation. *Journal of Geophysical Research, 73*(20), 6598-6600.

Holloway, J.R., Jakobsson, S. (1986) Volatile solubilities in magmas: transport of volatiles from mantles to planet surfaces. *Journal of Geophysical Research: Solid Earth (1978–2012)*, *91*(B4), 505-508.

Holloway, J.R., Reese, R.L., (1974) The generation of $N_2$−$CO_2$−$H_2O$ fluids for use in hydrothermal experimentation I: experimental method and equilibrium calculations in the C−O−H−N system. *American Mineralogist, 59*, 587-597.

Huizenga, J.M. (2001) Thermodynamic modelling of C–O–H fluids. *Lithos*, *55*(1), 101-114.

Izraeli E.S., Harris J.W., Navon O. (2001) Brine inclusions in diamonds: a new upper mantle fluid. *Earth and Planetary Science Letters*, *187*(3), 323-332.

Jakobsson, S., Holloway, J.R. (1986) Crystal—Liquid experiments in the presence of a COH fluid buffered by graphite + iron + wustite: Experimental method and near-liquidus relations in basanite. *Journal of volcanology and geothermal research, 29*(1), 265-291.

Jakobsson, S., Holloway, J.R. (2008) Mantle melting in equilibrium with an Iron–Wustite–Graphite buffered COH-fluid. *Contributions to Mineralogy and Petrology, 155*, 247-256.

Jakobsson, S., Oskarsson, N. (1994) The system CO in equilibrium with graphite at high pressure and temperature: An experimental study. *Geochimica et cosmochimica acta, 58*(1), 9-17.

Kaegi, R., Muntener, O., Ulmer, P. (2005) An experimental setup to control $fO_2$ in high-pressure $H_2O$-undersaturated natural calc-alkaline magmas. *Lithos, 73*, 53-53.

Kennedy, G.C., Wasserburg, G.J., Heard, H.C., Newton R.C. (1962) The upper three-phase region in the system $SiO_2$-$H_2O$. *American Journal of Science, 260*(7), 501-521.

Kerrick, D.M., Connolly, J.A.D. (1998) Subduction of ophicarbonates and recycling of $CO_2$ and $H_2O$. *Geology, 26*, 375-378.

Kerrick, D.M., Connolly, J.A.D. (2001a) Metamorphic devolatilization of subducted marine sediments and the transport of volatiles into the Earth's mantle. *Nature, 411*, 293-296.

Kerrick, D.M., Connolly, J.A.D. (2001b) Metamorphic devolatilization of subducted oceanic metabasalts: implications for seismicity, arc magmatism and volatile recycling. *Earth and Planetary Science Letters, 189*, 19-29.

Kessel, R., Ulmer, P., Pettke, T., Schmidt, M.W., Thompson, A.B. (2004) A novel approach to determine high-pressure high-temperature fluid and melt compositions using diamond-trap experiments. *American Mineralogist*, *89*(7), 1078-1086.

Kessel, R., Ulmer, P., Pettke, T., Schmidt, M.W., Thompson, A.B. (2005a) The water–basalt system at 4 to 6 GPa: phase relations and second critical endpoint in a K-free eclogite at 700 to 1400 °C. *Earth and Planetary Science Letters*, *237*(3), 873-892.

Kessel, R., Schmidt, M.W., Ulmer, P., Pettke, T. (2005b) Trace element signature of subduction-zone fluids, melts and supercritical liquids at 120–180 km depth. *Nature*, *437*(7059), 724-727.

Klein-BenDavid, O., Izraeli, E.S., Hauri, E., Navon, O. (2004) Mantle fluid evolution—a tale of one diamond. *Lithos*, *77*(1), 243-253.

Konzett, J., Ulmer, P. (1999) The stability of hydrous potassic phases in lherzolitic mantle. An experimental study to 9.5 GPa in simplified and natural bulk compositions. *Journal of Petrology, 40*, 629-652.

Koziol, A.M., Newton R.C. (1998) Experimental determination of the reaction: Magnesite + enstatite = forsterite + $CO_2$ in the ranges 6-25 kbar and 700-1100 °C. *American Mineralogist, 83*(3-4), 213-219.

Kushiro, I., Syono, Y., Akimoto, S. (1968) Melting of a peridotite nodule at high pressures and high water pressures. *Journal of Geophysical Research: Solid Earth (1978–2012), 73*, 6023-6029.

Labotka, T.C. (1991) Chemical and physical properties of fluids. *Reviews in Mineralogy and Geochemistry*, *26*(1), 43-104.

Liebscher, A. (2010) Aqueous fluids at elevated pressure and temperature. *Geofluids*, *10*(1-2), 3-19.

Litasov, K.D., Ohtani, E. (2009) Solidus and phase relations of carbonated peridotite in the system $CaO–Al_2O_3–MgO–SiO_2–Na_2O–CO_2$ to the lower mantle depths. *Physics of the Earth and Planetary Interiors*, *177*, 46-58.

Logvinova, A.M., Wirth, R., Fedorova, E.N., Sobolev, N.V. (2008) Nanometre-sized mineral and fluid inclusions in cloudy Siberian diamonds: New insights on diamond formation. *European Journal of Mineralogy, 20*, 317-331.

Luginbuehl, S., Ulmer, P., Pettke, T. (2013) *Mineralogical Magazine, 77*(5), 1649.

Luth R.W. (1999) Carbon and carbonates in the mantle. *Mantle Petrology: Field observations and high pressure experimentation*, 297-316.

Luth, R.W. (1989) Natural versus experimental control of oxidation state: Effects on the composition and speciation of COH fluids. *American Mineralogist*, *74*, 50-57.

Luth, R.W. (2003) Mantle volatiles-distribution and consequences. *Treatise on Geochemistry*, *2*, 319-361.

Malaspina, N., Scambelluri, M., Poli, S., Van Roermund, H.L.M., Langenhorst, F. (2010) The oxidation state of mantle wedge majoritic garnet websterites metasomatised by C-bearing subduction fluids. *Earth and Planetary Science Letters*, *298*(3), 417-426.

Malaspina, N., Tumiati, S. (2012) The role of COH and oxygen fugacity in subduction-zone garnet peridotites. *European Journal of Mineralogy*, *24*(4), 607-618.

Manning, C.E. (1994) The solubility of quartz in $H_2O$ in the lower crust and upper mantle. *Geochimica et Cosmochimica Acta*, *58*(22), 4831-4839.

Manning, C.E. (2004) The chemistry of subduction-zone fluids. *Earth and Planetary Science Letters, 223*, 1-16.

Manning, C.E., Antignano, A., Lin, H.A. (2010) Premelting polymerization of crustal and mantle fluids, as indicated by the solubility of albite plus paragonite plus quartz in $H_2O$ at 1 GPa and 350-620 °C. *Earth and Planetary Science Letters, 292*, 325-336.

Manning, C.E., Boettcher, S.L. (1994) Rapid-quench hydrothermal experiments at mantle pressures and temperatures. *American Mineralogist*, *79*(11), 1153-1158.

Manning, C.E., Shock, E.L., Sverjensky, D. (2013) The chemistry of carbon in aqueous fluids at crustal and uppermantle conditions: experimental and theoretical constraints. *Reviews in Mineralogy and Geochemistry, 75*, 109-148.

Marschall, H.R., Schumacher, J.C. (2012) Arc magmas sourced from mélange diapirs in subduction zones. *Nature Geoscience, 5*(12), 862-867.

Martin, A.M., Hammouda, T. (2011) Role of iron and reducing conditions on the stability of dolomite + coesite between 4.25 and 6 GPa – a potential mechanism for diamond formation during subduction. *European Journal of Mineralogy, 23*, 5-16.

Matveev, S., Ballhaus, C., Fricke, K., Trunckenbrodt, J., Ziegenbein, D. (1997) CHO volatiles under upper mantle conditions. I. Experimental results. *Geochimica et Cosmochimica Acta*, *61*, 3081-3088.

Melekhova, E., Schmidt, M.W., Ulmer, P., Guggenbühl, E. (2006) The reaction talc + forsterite = enstatite + $H_2O$ revisited: Application of conventional and novel experimental techniques and derivation of revised thermodynamic properties. *American Mineralogist*, *91*(7), 1081-1088.

Melekhova, E., Schmidt, M.W., Ulmer, P., Pettke, T. (2007) The composition of liquids coexisting with dense hydrous magnesium silicates at 11–13.5 GPa and the endpoints of the solidi in the $MgO–SiO_2–H_2O$ system. *Geochimica et Cosmochimica Acta*, *71*(13), 3348-3360.

Mibe, K., Fujii, T., Yasuda, A. (2002) Composition of aqueous fluid coexisting with mantle minerals at high pressure and its bearing on the differentiation of the Earth's mantle. *Geochimica et Cosmochimica Acta*, *66*(12), 2273-2285.

Molina, J.F., Poli, S. (2000) Carbonate stability and fluid composition in subducted oceanic crust: an experimental study on $H_2O–CO_2$-bearing basalts. *Earth and Planetary Science Letters, 176*, 295-310.

Morgan, G.B., Chou, I., Pasteris, J.D. (1992) Speciation in experimental COH fluids produced by the thermal dissociation of oxalic acid dihydrate. *Geochimica et Cosmochimica Acta*, *56*(1), 281-294.

Mysen, B.O. (1975) Solubility of volatiles in silicate melts at high pressure and temperature: the role of carbon dioxide and water in feldspar, pyroxene, and feldspathoid melts. *Carnegie Institution of Washington Yearbook*, *74*, 454-468.

Mysen, B.O., Boettcher, A. L. (1975) Melting of hydrous mantle: I. Phase relations of natural peridotite at high pressures and temperatures with controlled activities of water, carbon dioxide and hydrogen. *Journal of Petrology, 16*, 520-548.

Mysen, B.O., Mibe, K., Chou, I.M., Bassett, W.A. (2013b) Structure and equilibria among silicate species in aqueous fluids in the upper mantle: Experimental $SiO_2–H_2O$ and $MgO–SiO_2–H_2O$ data recorded in situ to 900 °C and 5.4 GPa. *Journal of Geophysical Research: Solid Earth*, *118*(12), 6076-6085.

Mysen, B.O., Tomita, T., Ohtani, E., Suzuki, A. (2013a) Speciation of and D/H partitioning between fluids and melts in silicate-DOHCN systems determined in-situ at upper mantle temperatures, pressures, and redox conditions. *American Mineralogist*, *99*(4), 578-588.

Naemura, K., Hirajima, T., Svojtka, M. (2009) The Pressure–Temperature Path and the Origin of Phlogopite in Spinel–Garnet Peridotites from the Blanský Les Massif of the Moldanubian Zone, Czech Republic. *Journal of Petrology*, *50*(10), 1795-1827.

Nakamura, Y., Kushiro, I. (1974) Composition of the gas phase in $Mg_2SiO_4$-$SiO_2$-$H_2O$ at 15 kbar. *Carnegie Institution of Washington Yearbook*, *73*, 255-258.

Navon, O., Hutcheon, I.D., Rossman, G.R., Wasserburg, G.J. (1988) Mantle-derived fluids in diamond micro-inclusions. *Nature, 335*, 784-789.

Newton, R.C., Manning, C.E. (2000) Quartz solubility in $H_2O$-NaCl and $H_2O$-$CO_2$ solutions at deep crust-upper mantle pressures and temperatures: 2–15 kbar and 500–900 °C. *Geochimica et Cosmochimica Acta*, *64*(17), 2993-3005.

Newton, R.C., Manning, C.E. (2002) Experimental determination of calcite solubility in $H_2O$-NaCl solutions at deep crust/upper mantle pressures and temperatures: Implications for metasomatic processes in shear zones. *American Mineralogist*, *87*(10), 1401-1409.

Newton, R.C., Manning, C.E. (2009) Hydration state and activity of aqueous silica in $H_2O$-$CO_2$ fluids at high pressure and temperature. *American Mineralogist*, *94*(8-9), 1287-1290.

Newton, R.C., Manning, C.E. (2010) Role of saline fluids in deep-crustal and upper mantle metasomatism: insights from experimental studies. *Geofluids* 10, 58-72.

Newton, R.C., Manning, C.E., Hanchar, J.M., Colasanti C.V. (2010) Free energy of formation of zircon based on solubility measurements at high temperature and pressure. *American Mineralogist, 95*, 52–58.

Niida, K., Green, D.H. (1999) Stability and chemical composition of pargasitic amphibole in MORB pyrolite under upper mantle conditions. *Contributions to Mineralogy and Petrology*, *135*(1), 18-40.

Ohmoto, H., Kerrick, D.M. (1977) Devolatilization equilibria in graphitic systems. *American Journal of Science*, *277*(8), 1013-1044.

Olafsson, M., Eggler, D.H. (1983) Phase relations of amphibole, amphibole-carbonate, and phlogopite-carbonate peridotite: petrologic constraints on the asthenosphere. *Earth and Planetary Science Letters*, *64*(2), 305-315.

Pan, D., Spanu, L., Harrison, B., Sverjensky, D.A., Galli, G. (2013) Dielectric properties of water under extreme conditions and transport of carbonates in the deep Earth. *Proceedings of the National Academy of Sciences*, *110*(17), 6646-6650.

Pasteris, J.D. (1987) Fluid inclusions in mantle xenoliths. *Mantle xenoliths*, 691-707.

Peacock, S.M. (2001) Are the lower planes of double seismic zones caused by serpentine dehydration in subducting oceanic mantle? *Geology*, *29*(4), 299-302.

Perchuk, A.L., Korepanova, O.S. (2011) The problem of $CO_2$ recycling in subduction zones. *Moscow University Geology Bulletin*, *66*(4), 250-260.

Peretti, A., Dubessy, J., Mullis, J., Frost, B.R., Trommsdorff, V. (1992) Highly reducing conditions during Alpine metamorphism of the Malenco peridotite (Sondrio, northern Italy) indicated by mineral paragenesis and $H_2$ in fluid inclusions. *Contributions to Mineralogy and Petrology*, *112*(2-3), 329-340.

Pernert, J.C. (1952) Oxalic acid. *Encyclopedia of Chemical Technology*, *9*, 661-674.

Pettke, T., Oberli, F., Audétat, A., Guillong, M., Simon, A.C., Hanley, J.J., Klemm, L.M. (2012) Recent developments in element concentration and isotope ratio analysis of individual fluid inclusions by laser ablation single and multiple collector ICP-MS. *Ore Geology Reviews*, *44*, 10-38.

Poli, S., Franzolin, E., Fumagalli, P., Crottini, A. (2009) The transport of carbon and hydrogen in subducted oceanic crust: an experimental study to 5 GPa. *Earth and Planetary Science Letters*, *278*(3), 350-360.

Poli, S., Schmidt, M.W. (1995) $H_2O$ transport and release in subduction zones: experimental constraints on basaltic and andesitic systems. *Journal of Geophysical Research: Solid Earth (1978–2012)*, *100*(B11), 22299-22314.

Poli, S., Schmidt, M.W. (1998) The high-pressure stability of zoisite and phase relationships of zoisite-bearing assemblages. *Contributions to Mineralogy and Petrology*, *130*(2), 162-175.

Poli, S., Schmidt, M.W. (2002) Petrology of subducted slabs. *Annual Review of Earth and Planetary Sciences*, *30*(1), 207-235.

Roedder, E. (1965) Liquid $CO_2$ inclusions in olivine-bearing nodules and phenocrysts from basalts. *American Mineralogist*, *50*(10), 1746.

Roedder, E. (1984) Fluid inclusions. *Reviews in Mineralogy, 12*, 79-108.

Rosenbaum, J.M., Slagel, M.M. (1995) COH speciation in piston-cylinder experiments. *American Mineralogist*, *80*, 109-114.

Ryabchikov, I.D., Schreyer, W., Abraham, K. (1982) Compositions of aqueous fluids in equilibrium with pyroxenes and olivines at mantle pressures and temperatures. *Contributions to Mineralogy and Petrology*, *79*(1), 80-84.

Saxena, S.K., Fei, Y. (1987) High pressure and high temperature fluid fugacities. *Geochimica et Cosmochimica Acta*, *51*(4), 783-791.

Saxena, S.K., Fei, Y. (1988) Fluid mixtures in the C-H-O system at high pressure and temperature. *Geochimica et Cosmochimica Acta*, *52*(2), 505-512.

Scambelluri, M., Pettke, T., Van Roermund, H.L.M. (2008) Majoritic garnets monitor deep subduction fluid flow and mantle dynamics. *Geology*, *36*(1), 59-62.

Scambelluri, M., Philippot, P. (2001) Deep fluids in subduction zones. *Lithos*, *55*(1), 213-227.

Schiano, P., Clocchiatti, R., Shimizu, N., Maury, R.C., Jochum, K.P., Hofmann, A.W. (1995) Hydrous, silica-rich melts in the sub-arc mantle and their relationship with erupted arc lavas. *Nature*, *377*(6550), 595-600.

Schmidt, M.W., Poli, S. (1998) Experimentally based water budgets for dehydrating slabs and consequences for arc magma generation. *Earth and Planetary Science Letters*, *163*(1), 361-379.

Schmidt, M.W., Poli, S. (2003) Generation of mobile components during subduction of oceanic crust. *Treatise on Geochemistry*, *3*, 567-591.

Schmidt, M.W., Poli, S. (2014) Devolatilization During Subduction. *Treatise on Geochemistry (Second Edition), 4*, 669-701.

Schmidt, M.W., Ulmer, P. (2004) A rocking multianvil: elimination of chemical segregation in fluid-saturated high-pressure experiments. *Geochimica et Cosmochimica Acta*, *68*(8), 1889-1899.

Schneider, M.E., Eggler, D.H. (1986) Fluids in equilibrium with peridotite minerals: implications for mantle metasomatism. *Geochimica et Cosmochimica Acta*, *50*(5), 711-724.

Shmulovich, K.I., Graham, C., Yardley, B. (2001) Quartz, albite and diopside solubilities in $H_2O$–NaCl and $H_2O$–$CO_2$ fluids at 0.5–0.9 GPa. *Contributions to Mineralogy and Petrology*, *141*(1), 95-108.

Shmulovich, K.I., Yardley, B.W.D., Graham, C.M. (2006) Solubility of quartz in crustal fluids: experiments and general equations for salt solutions and $H_2O$–$CO_2$ mixtures at 400–800 C and 0.1–0.9 GPa. *Geofluids*, *6*(2), 154-167.

Stalder, R., Ulmer, P. (2001) Phase relations of a serpentine composition between 5 and 14 GPa: significance of clinohumite and phase E as water carriers into the transition zone. *Contributions to Mineralogy and Petrology*, *140*(6), 670-679.

Stalder, R., Ulmer, P., Thompson, A.B., Günther, D. (2000) Experimental approach to constrain second critical end points in fluid/silicate systems: Near-solidus fluids and melts in the system albite–$H_2O$. *American Mineralogist*, *85*(1), 68-77.

Stalder, R., Ulmer, P., Thompson, A., Günther, D. (2001) High pressure fluids in the system MgO–$SiO_2$–$H_2O$ under upper mantle conditions. *Contributions to Mineralogy and Petrology*, *140*(5), 607-618.

Sverjensky, D.A., Harrison, B., Azzolini, D. (2014) Water in the deep Earth: The dielectric constant and the solubilities of quartz and corundum to 60kb and 1200 °C. *Geochimica et Cosmochimica Acta*, *129*, 125-145.

Taylor, W.R., Foley, S.F. (1989) Improved oxygen-buffering techniques for C-O-H fluid-saturated experiments at high pressure. *Journal of Geophysical Research: Solid Earth (1978–2012)*, *94*(B4), 4146-4158.

Taylor, W.R., Green, D.H. (1988) Measurement of reduced peridotite–COH solidus and implications for redox melting of the mantle. *Nature*, *332*(6162), 349-352.

Thibault, Y., Edgar, A.D., Lloyd, F.E. (1992) Experimental investigation of melts from a carbonated phlogopite lherzolite: implications for metasomatism in the continental lithospheric mantle. *American Mineralogist*, *77*, 784-794.

Thomsen, T.B., Schmidt, M.W. (2008) Melting of carbonated pelites at 2.5–5.0 GPa, silicate–carbonatite liquid immiscibility, and potassium–carbon metasomatism of the mantle. *Earth and Planetary Science Letters, 267*(1), *17-31.*

Tomlinson, E.L., McMillan, P.F., Zhang, M., Jones, A.P., Redfern, S.A. (2007) Quartz-bearing C–O–H fluid inclusions diamond: Retracing the pressure–temperature path in the mantle using calibrated high temperature IR spectroscopy. *Geochimica et Cosmochimica Acta*, *71*(24), 6030-6039.

Tropper, P., Manning, C.E. (2005) Very low solubility of rutile in $H_2O$ at high pressure and temperature, and its implications for Ti mobility in subduction zones. *American Mineralogist*, *90*(2-3), 502-505.

Tropper, P., Manning, C.E. (2007) The solubility of corundum in $H_2O$ at high pressure and temperature and its implications for Al mobility in the deep crust and upper mantle. *Chemical Geology*, *240*(1), 54-60.

Truckenbrodt, J., Ziegenbein, D., Johannes, W. (1997) Redox conditions in piston-cylinder apparatus: The different behavior of boron nitride and unfired pyrophyllite assemblies. *American Mineralogist*, *82*, 337-344.

Truckenbrodt, J., Johannes, W. (1999) $H_2O$ loss during piston-cylinder experiments. *American Mineralogist*, *84*, 1333-1335.

Tsuno, K., Dasgupta, R. (2011) Melting phase relation of nominally anhydrous, carbonated pelitic-eclogite at 2.5–3.0 GPa and deep cycling of sedimentary carbon. *Contributions to Mineralogy and Petrology*, *161*(5), 743-763.

Tumiati, S., Fumagalli, P., Tiraboschi, C., Poli, S. (2013) An Experimental Study on COH-bearing Peridotite up to 3.2 GPa and Implications for Crust–Mantle Recycling. *Journal of Petrology*, *54*(3), 453-479.

Tuttle, O.F., Bowen, N.L. (1958) Origin of granite in the light of experimental studies in the system $NaAlSi_3O_8$–$KAlSi_3O_8$–$SiO_2$–$H_2O$. *Geological Society of America Memoirs, 74*, 1-153.

Ulmer, P. (2001) Partial melting in the mantle wedge – the role of $H_2O$ in the genesis of mantle-derived 'arc-related' magmas. *Physics of the Earth and Planetary Interiors, 127*(1), 215-232.

Ulmer, P., Trommsdorff, V. (1995) Serpentine stability to mantle depths and subduction-related magmatism. *Science*, *268*(5212), 858-861.

Ulmer, P., Trommsdorff, V. (1999) Phase relations of hydrous mantle subducting to 300 km. *Mantle Petrology: Field Observations and High-Pressure Experimentation*, 259-281.

Van Roermund, H.L.M., Carswell, D.A., Drury, M.R., Heijboer, T.C. (2002) Microdiamonds in a megacrystic garnet websterite pod from Bardane on the island of Fjørtoft, western Norway: Evidence for diamond formation in mantle rocks during deep continental subduction. *Geology 30*, 959-962.

Wallace, M., Green, D.H. (1991) The effect of bulk rock composition on the stability of amphibole in the upper mantle: implications for solidus positions and mantle metasomatism. *Mineralogy and Petrology*, *44*(1-2), 1-19.

Wallace, M.E., Green, D.H. (1988) An experimental determination of primary carbonatite magma composition. *Nature, 335*, 343-346.

Wallace, P.J. (2005) Volatiles in subduction zone magmas: concentrations and fluxes based on melt inclusion and volcanic gas data. *Journal of Volcanology and Geothermal Research*, *140*(1), 217-240.

Walther, J.V. (1997) Experimental determination and interpretation of the solubility of corundum in $H_2O$ between 350 and 600 °C from 0.5 to 2.2 kbar. *Geochimica et Cosmochimica Acta*, *61*(23), 4955-4964.

Walther, J.V., Orville, P.M. (1983) The extraction-quench technique for determination of the thermodynamic properties of solute complexes: Application to quartz solubility in fluid mixtures. *American Mineralogist, 68*, 731-741.

White, B.S., Wyllie, P.J. (1992) Solidus reactions in synthetic lherzolite–$H_2O$–$CO_2$ from 20-30 kbar, with applications to melting and metasomatism. *Journal of Volcanology and Geothermal Research, 50*, 117-130.

Withers, A.C., Hirschmann, M.M. (2008) Influence of temperature, composition, silica activity and oxygen fugacity on the $H_2O$ storage capacity of olivine at 8 GPa. *Contributions to Mineralogy and Petrology*, *156*(5), 595-605.

Wyllie, P.J. (1977) Effects of $H_2O$ and $CO_2$ on magma generation in the crust and mantle. *Journal of the Geological Society, 134*, 215-234.

Yoder, H.S., Tilley, C.E. (1962) Origin of basalt magmas: an experimental study of natural and synthetic rock systems. *Journal of Petrology*, *3*(3), 342-532.

Yoshida, T., Nishizawa, K., Tabata, M., Abe, H., Kodama, T., Tsuji, M., Tamaura, Y. (1993) Methanation of $CO_2$ with $H_2$-reduced magnetite. *Journal of materials science*, *28*(5), 1220-1226.

Zhang, C., Duan, Z. (2009) A model for C–O–H fluid in the Earth's mantle. *Geochimica et Cosmochimica Acta*, *73*(7), 2089-2102.

Zhang, H.F., Nakamura, E., Sun, M., Kobayashi, K., Zhang, J., Ying, J.F., Tang, Y.J., Niu, L.F. (2007) Transformation of subcontinental lithospheric mantle through peridotite-melt reaction: evidence from a highly fertile mantle xenolith from the North China craton. *International Geology Review*, *49*(7), 658-679.

Zhang, Y.G., Frantz, J.D. (2000) Enstatite-forsterite-water equilibria at elevated temperatures and pressures. *American Mineralogist*, *85*(7-8), 918-925.

Zotov, N., Keppler, H. (2000) In-situ Raman spectra of dissolved silica species in aqueous fluids to 900 C and 14 kbar. *American Mineralogist*, *85*(3-4), 600-604.

Zotov, N., Keppler, H. (2002) Silica speciation in aqueous fluids at high pressures and high temperatures. *Chemical Geology*, *184*(1), 71-82.